# SILICON MICRO AND NANO PHOTONIC DEVICES FOR PHOTONIC INTEGRATED CIRCUITS

by

Deepak V. Simili

Submitted in partial fulfillment of the requirements
for the degree of Doctor of Philisophy

at

Dalhousie University
Halifax, Nova Scotia
August 2019

*I would like to thank my family for their strength, patience and support.*

# Table of Contents

## List of Tables

# List of Figures

# Abstract

Silicon photonics has the potential to provide compact sized, high performance photonic devices to enable low cost photonic integrated circuits for telecom, datacom and other high data rate applications. Silicon as a material has a mature fabrication process developed over the years from the electronics industry, leading to smaller device sizes of the order of micrometers with precise control and lower costs compared to other photonic materials such as III/V group semiconductors and optical crystals such as Lithium Niobate.

In this thesis, silicon photonic devices on micron and 220 nm scale thicknesses are described. A novel shallow etch polarization beam splitter in micron scale silicon photonics has been designed. The nominal design has excellent device performance of low excess loss below 0.4 dB for TE and TM polarizations and polarization extinction ratio greater than 15 dB over the telecom C band of 1530-1565 nm. In addition, the nominal design is robust to fabrication error of +/- 10 nm in etch depth variation and +/- 50 nm in waveguide width variation. In nanometer scale silicon photonics, novel design of a high performance electro-optic modulator using the ultrafast electro-optic Kerr effect in silicon nanocrystals is described. Analysis of the modulator indicates a high data rate transmission of 90 Gb/s with low energy consumption of 25.13 fJ/bit and a compact ring resonator structure having a diameter of 40 micrometers. In addition, theory, design simulation, fabrication and experimental characterization of Mach Zehnder Interferometer (MZI) circuits and slot waveguide Bragg grating structures have been described on 220 nm silicon thickness. A novel slow light propagation loss of 5.1 dB/mm with group index of 12.38 near 1555 nm wavelength has been experimentally obtained in slot waveguide Bragg gratings with internal corrugation. This leads to an excellent phase shifter performance for high performance electro-optic modulators and integrated-optic sensing applications.

## List of Abbreviations Used

| | |
|---|---|
| AC | Alternating Current |
| ASK | Amplitude Shift Keying |
| BOX | Buried Oxide |
| BPD | Bipolar Photo Diode |
| BS | Beam Splitter |
| CAD | Computer Aided Design |
| CMOS | Complementary Metal Oxide Semiconductor |
| CW | Continuous Wave |
| DC | Direct Current |
| DCA | Digital Communication Analyzer |
| e-beam | Electron Beam |
| EM | Electro Magnetic |
| FDTD | finite Difference Time Domain |
| FSR | Free Spectral Range |
| Gbps | Giga bits per second |
| I | In phase Component |
| ICP | Inductively Coupled Plasma |
| Ix | In phase Component TE polarization |
| Iy | In phase Component TM polarization |

| | |
|---|---|
| ICSBG | Internally corrugated slot Bragg grating |
| LIDAR | Light Detection and Ranging |
| LLC | Limited Liability Company |
| LO | Local Oscillator |
| MMF | Multi mode fiber |
| MMI | Multimode Interference |
| MPW | Multi Project Wafer |
| MRR | Micro Ring Resonator |
| MZI | Mach Zehnder Interferometer |
| NRZ | Non return to Zero |
| OOK | On-Off Keying |
| PBS | Polarization Beam Splitter |
| PC | Polarization Converter |
| PDK | Process Design Kit |
| PECVD | Plasma Enhanced Chemical Vapour Deposition |
| PRBS | Pseudo Random Bit Sequence |
| PLC | Planar Lightwave Circuit |
| Q | Quadrature Component |
| Qx | Quadrature Component TE polarization |
| Qy | Quadrature Component TM polarization |
| QPSK | Quadrature Phase Shift Keying |

RC Resistance Capacitance

RCMT Rigorous Coupled Mode Theory

RF Radio Frequency

RIE Reactive Ion Etcher

RZ Return to Zero

SEM Scanning Electron Microscope

Si Silicon

$SiO_2$ Silicon dioxide

$Si - nc - SiO_2$ Silicon nanocrystals embedded in Silica.

SOI Silicon on Insulator

SMF Single Mode Fiber

SOI Silicon on Insulator

TE Transverse Electric

TEOS Tetra Ethyl Ortho Silicate

TM Transverse Magnetic

Tx Transmission

WDM Wavelength Division Multiplexing

## Acknowledgements

I would like to thank my supervisor Prof. Michael Cada and Dalhousie University for giving me an opportunity to pursue my graduate studies at the Photonics Application Lab. I'm grateful for his research experience and mentorship over the years that has allowed me to develop professionally. Prof. Cada and Prof. Yuan Ma from the Electrical and Computer Engineering department at Dalhousie along with several other colleagues developed a very interesting PhD program called ASPIRE (Applied Science in Photonics and Innovative Research in Engineering). Herein, after completing my coursework, I got experience of cutting edge research related to my thesis as part of academic collaboration of Prof. Lukas Chrostowski's NSERC SiEPIC (Silicon Electronic-Photonic Integrated Circuits) program at UBC and Industrial internship on a silicon photonics project conducted at Lumentum LLC in Ottawa, Canada. Both these experiences gave me a practical perspective in the field of silicon photonics in an academic research environment as well as requirements and challenges in a industrial research setting. These experiences helped me shape and form the building blocks of my thesis. I would like to thank the silicon photonics group at Lumentum for having me as part of their team. I also thank the Photonics Application Lab group members at Dalhousie with whom I have had the privilege of working with and have numerous interesting discussions over the years.

I acknowledge the edX UBCx Phot1x Silicon Photonics Design, Fabrication and Data Analysis course, which is supported by the Natural Sciences and Engineering Research Council of Canada (NSERC) Silicon Electronic-Photonic Integrated Circuits (SiEPIC) Program. The silicon photonic devices described in chapter 4 of this thesis were fabricated by Richard Bojko at the University of Washington Washington Nanofabrication Facility, part of the National Science Foundation's National Nanotechnology Infrastructure Network (NNIN) and Cameron Horvath at Applied Nanotools, Inc.. Measurement results reported in chapter 4 were performed by Hossam Shoman through the automated test setup at The University of British Columbia.I

thank Professor J. Pistora from the Nanotechnology Center, VSB-Technical University of Ostrava for valuable suggestions and support of this work. I acknowledge CMC Microsystems for access to design software in particular, Lumerical Solutions, Inc.,Photon Design, Mathworks, Python, and KLayout.

I'm thankful for the financial support provided by NSERC ASPIRE program, Nova Scotia Graduate Scholarship and the Dalhousie Faculty of Graduate Studies scholarship during my PhD studies.

Finally, I thank my parents and my elder brother for their continuous support and encouragement throughout my studies.

# Chapter 1

## Introduction

The present age of the twenty first century is also called as the information age with exponential growth of digital data leading to connectivity and development in almost every field through the Information and communications technology (ICT) sector. The internet traffic volume has been increasing at an exponential rate and it is predicted that the annual global Internet protocol(IP) traffic would be 396 Exabytes ($396 \times 10^{18}$bytes) per month in the year 2022 [9]. This growth in internet traffic mainly due to increase in the percentage of population with access to internet and the number of devices per person connected to the internet (for ex. laptop,desktop, smartphone,security camera etc.). It is estimated that there would be 50 billion devices connected to the internet by the year 2020 [10]. This has led to the challenge of scaling equipment performance with the internet traffic growth.

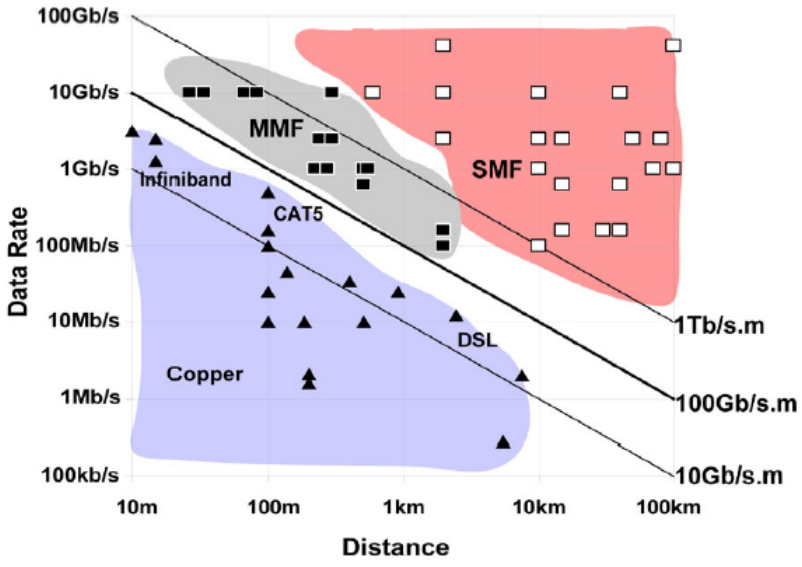


Figure 1.1: Data rate and distances for commercially deployed interconnects of different media,©[2006] IEEE [2]

Traditionally, fiber optic links were used for transporting data over large distances

of the range of 100's of Kms. This is because electrical copper cables have higher attenuation and therefore are more lossy for higher frequencies than optical fiber cables. At a sufficient bandwidth distance product of 100 Gbps.m per wire pair or fiber, it becomes practical to transition from an electronic interconnect to an optical interconnect as shown in Fig. 1.1. With continuous increase in data rates of Ethernet which are on the order 100 Gbps [11], an MMF optical link would be the viable option at a distance of 1 meter and at 10 meters a single mode fiber (SMF)would be appropriate. As these distances correspond to machine to machine and between offices, one can expect an increasing penetration of optical links closer to the end user and within machines itself.

Present photonic components in the core network are made of III/V group semiconductor materials or optical crystals such as Lithium Niobate and silica based PLC (Planar light wave circuits), which have larger footprint and are more expensive compared to silicon. Silicon with its mature CMOS fabrication process developed over the years through the electronics industry, offers the opportunity to be the photonic material for high performance photonic components that can meet the demands for increased integration and higher data rates.

## 1.1 Motivation and Objective

My main motivation is to specialize in the field of telecommunication engineering in the area of fiber optic communication. Photonics is a very important part of this and silicon photonics has big potential to further development of fiber optic communication.

A modulator is an important component in a photonic integrated circuit as it transfers the message signal to optical domain for transmission over large bandwidth optical fibers. Therefore it is highly desirable to have fast (sub picosecond response times), compact and low cost modulators with low energy consumption to meet demands for present day exponential growth in digital data. Through this thesis I intend to describe my contribution towards these goals in the form of design of a silicon high speed DC Kerr effect modulator, and an experimentally verified low loss slow light enhanced silicon phase shifter section for an MZI based modulator.

I had the desire and opportunity to work on a silicon photonics industrial project

for telecom or datacom applications through an internship. Through this internship, I got a first hand experience on passive design, fabrication and characterization of micron scale silicon photonic components , which I intend to describe as a chapter in my thesis.

## 1.2 Silicon Photonic Integrated Circuits

It has been hypothesized that silicon photonics could be the next fabless semiconductor industry [12]. This means that one could outsource fabrication of silicon photonic components to third party standard fabrication foundries, and focus their efforts on designing and testing novel silicon photonic components. The development of microelectronics industry during later half of the twentieth century can be attributed to this fablass semiconductor concept and multi project wafer runs where several designers could share their designs in a single chip fabrication run [13]. A few companies such as Luxtera, Mellanox have already commercialized their silicon photonic products[14, 15].Indeed several fabrication foundries with CMOS (AMF [16], ePIXfab [17]) or ebeam capabilities (Washington Nanofabrication Facility at Univ. of Washington [18], Applied Nanotools [19] )have offered multiproject wafer run schuttles to enable students and researchers to fabricate their designs and have them experimentally characterized.

The fundamental cross section of an SOI (Silicon On Insulator) wafer used by fabrication foundries is shown in Fig. 1.2. It has a 2 micron buried oxide (BOX) layer above which is a layer of silicon, which is also called as the device layer as photonic devices are patterned on this silicon layer. The device layer thickness is shown as H as its chosen based on customer requirements which are application dependant. The most widely used thickness for multi project wafer runs is 220 nm (AMF, ePIXfab, WNF, ANT) , but other thicknesses are also used such as 2-4 microns by Mellanox [7], 300 nm by Luxtera [20].The cladding is generally an oxide layer with thickness of 1.5 microns. In this thesis, I would be reporting on silicon photonic devices with micron scale and 220 nm device layer thicknesses.

Most fiber optic communication system infrastructure employ wavelength division multiplexing (WDM) operating with 50 GHz channel spacing at 10 Gb/s per channel using digital On-Off keying (OOK) modulation technique. Here one bit is encoded per

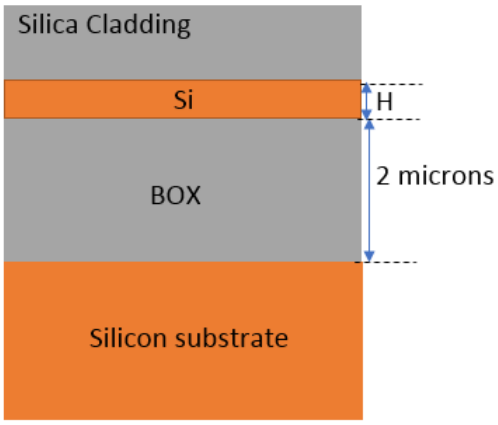


Figure 1.2: Cross section of an SOI wafer

symbol. The spectral efficiency for this type of modulation technique is 0.8 bits/s/Hz per polarization [3]. With the demand for higher bandwidths leading to subsequent increase in data rates in the range of 100's Gbps, OOK modulation cannot be used with the present 50 GHz channel bandwidth. In order to overcome this bandwidth limitation, advanced modulation formats such as in coherent digital modulation along with polarization multiplexing can be used with the present 50 GHz channel infrastructure at the expense of a more complex transmitter and receiver circuit [3, 4].

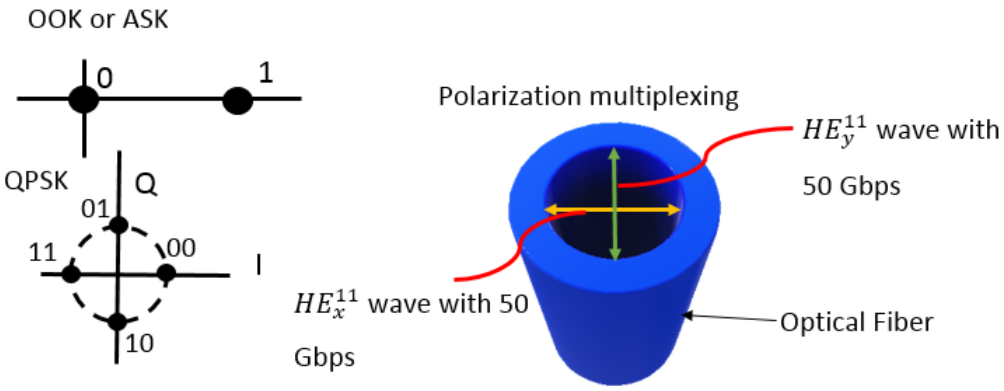


Figure 1.3: (a) Signal constellation for On-Off keying (OOK) or Amplitude Phase Shift Keying (ASK) and quadrature phase shift keying (QPSK) (b) polarization multiplexing concept in an optical fiber

Fig. 1.3(a) shows the signal constellation diagram for OOK also known as ASK (Amplitude Shift Keying) and Quadrature Phase Shift Keying (QPSK). In OOK

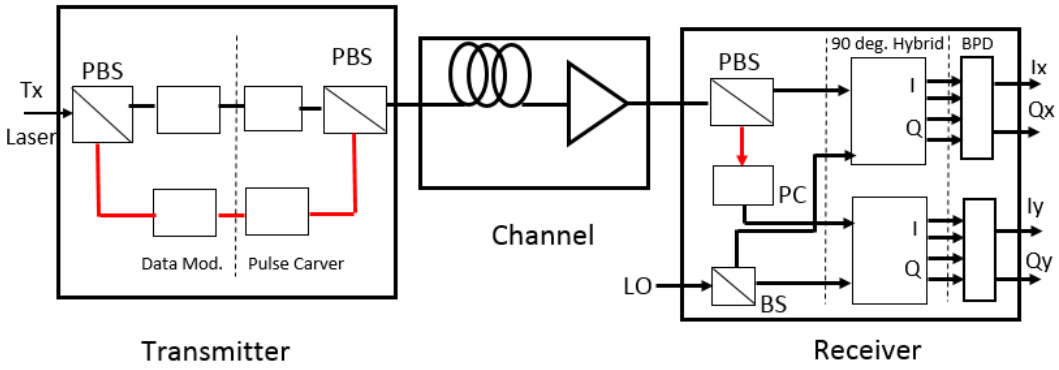


Figure 1.4: Implementation of a coherent transmission system [3, 4]

digital modulation, only 2 distinct signals (0 or 1) can be transmitted with a single source data bit. Here there is only amplitude variation between the signals and no quadrature phase component. In QPSK digital modulation, four distinct symbols (00, 01, 10, 11) can be transmitted with a single amplitude but their phases being in quadrature with each other as shown in the signal constellation for QPSK. Here two source data bits are utilized for each symbol and therefore the transmitted bits can be doubled in the same channel bandwidth as compared to OOK modulations. Using polarization multiplexing as shown in Fig. 1.3(b) where data is encoded in TE and TM polarized waves, one can achieve an aggregate data rate of 100 Gbps using the present 50 GHz channel bandwidth infrastructure

Fig. 1.4 shows a block diagram implementation of a coherent transmission system. Polarization beam splitters (PBS) are used in the transmitter section to achieve polarization multiplexing. Data modulators generally implemented using a Mach-Zehnder Interferometer (MZI) circuit are used to encode message data symbols onto the optical carrier followed by a pulse carver to shape the baseband signal to a binary data format such as NRZ (non return to zero) or RZ (return to zero).The channel comprises of long sections of optical fiber with amplifier sections at periodic intervals. The receiver part performs coherent detection by combining the received signal with a local oscillator.The front end of the receiver has a PBS and a polarization converter (PC) for polarization management and a beam splitter (BS) to to split the local oscillator light. This is followed by an optical 90 degree hybrid section that combines the received signal and local oscillator signal to produce in-phase (I) and quadrature (Q)

components. Differential (bipolar) photo diodes (BPD) are used to convert optical signal back to electrical signal. The photonic building blocks as used in the transmitter and receiver photonic integrated circuit sections of the coherent communication system can be implemented using silicon photonic components. Examples of practical implementation of 100 Gbps coherent communication system using silicon photonic integrated circuits have been demonstrated in [21, 22], with transmission and coherent detection of 112 Gbps polarization division multiplexed QPSK signal over 2560 Km standard single mode fiber being demonstrated in [22] .

It is highly desirable to have photonic devices used to implement the coherent transmission system to have a small device footprint, have low loss and for active devices such as a data modulator , have low energy consumption (i.e. low $V_\pi L$ or energy/bit) with capability to operate at data rates $\sim$ 100 Gbps. In this thesis, designs of a polarization beam splitter (PBS) using micron scale silicon photonics and a high performance data modulator using nanometer scale silicon photonics are presented. In addition devices applicable for a data modulator such as Mach-Zehnder Interferometers and slot waveguide Bragg gratings as a phase shifter structure are described in detail through design, fabrication end experimental data analysis.

The ability to develop high performance photonic functionalities using silicon platforms drives down cost to transmit data over the fiber therefore giving applications beyond data communications such as electromagnetic wave sensing [23, 24] and biosensors [25, 6] , Microwave photonics [26], LIDAR [27], and autonomous car applications [28, 29]

The following sections describe building block devices used in this thesis for silicon photonic integrated circuits. Specifically devices to split and combine light such are Mach Zehnder interferometers, multimode interferometers and wavelength selective devices such as ring resonators and slot waveguide Bragg gratings are discussed.

### 1.2.1 Mach Zehnder Interferometer

The MZI structure consists of two waveguide arms as shown in Fig. 1.5. The input light is made to propagate through the two arms and then made to interfere at the output to extract out the properties of the two waveguide arms such as path length difference, waveguide effective index or group index in the case of passive applications

or for modulation or switching of the input light for active applications.

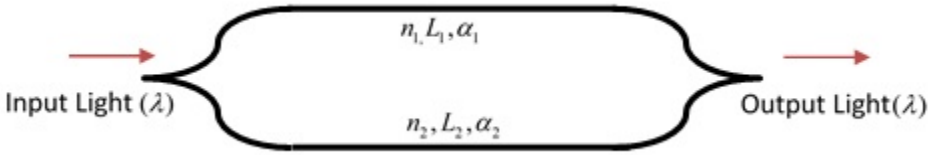


Figure 1.5: MZI structure schematic

The propagation constant in the two waveguide arms is given as $\beta_1 = 2\pi n_1/\lambda$ for the upper arm and $\beta_2 = 2\pi n_2/\lambda$ for the lower arm. Here $n_1, n_2$ are the effective indices of the upper and lower waveguide arms respectively. The waveguide arms have lengths of $L_1$ and $L_2 = L_1 + \Delta L$ with losses $\alpha_1$ and $\alpha_2$ respectively. The electric fields of the waves after propagating through the two waveguide arms [30] are,

$$E_1 = (E_i e^{-i\beta_1 L_1 - \alpha_1 L_1/2})/\sqrt{2} \tag{1.1}$$

$$E_2 = (E_i e^{-i\beta_2 L_2 - \alpha_2 L_2/2})/\sqrt{2} \tag{1.2}$$

Here $E_i$ is the input light electric field. The output light electric field after the Y branch combiner is,

$$E_o = (E_1 + E_2)/\sqrt{2} \tag{1.3}$$

Using (1.1) and (1.2), the intensity of the output light is,

$$I_o = \frac{I_i}{4} \, |e^{-i\beta_1 L_1 - \alpha_1 L_1/2} + e^{-i\beta_2 L_2 - \alpha_2 L_2/2}|^2 \tag{1.4}$$

Here $I_i$ is the input intensity light. We can observe that output light intensity is a function of the sum of the two phase components of the waves propagating through the two MZI arms. Considering negligible losses, equation (1.4) simplifies to

$$I_o = \frac{I_i}{2} \, [1 + \cos(\beta_1 L_1 - \beta_2 L_2)] \tag{1.5}$$

From equation (1.5), we observe that the output intensity is a sinusoidally varying function of the input light wavelength and the period is termed as the free spectral range (FSR) of the MZI.

$$FSR = \frac{\lambda^2}{n_g \Delta L} \tag{1.6}$$

Here $n_g$ is the group index of the waveguide. The analytical simulation for an MZI with a path length difference of 30 $\mu$m is shown in Fig. 1.6 where the FSR is 19.08 nm.

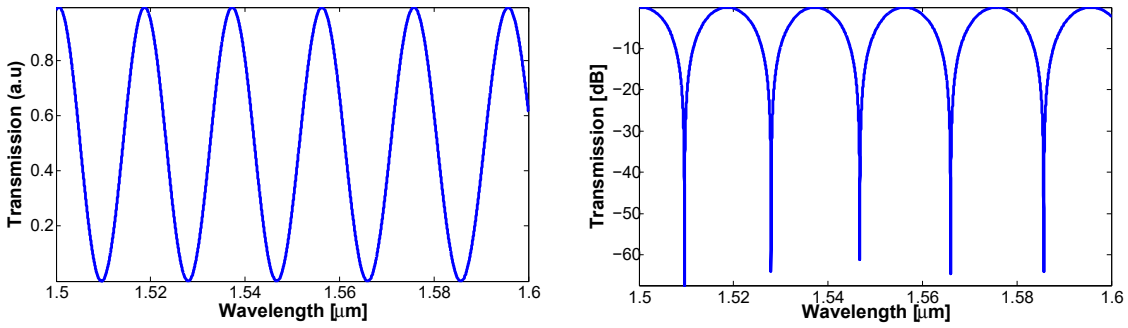


(a) (b)

Figure 1.6: Transmission spectra for an MZI with a path length difference of 30 $\mu$m in (a) Normalized units. (b) Log scale.

### 1.2.2 Multimode Interferometers

A multimode interferometer (MMI) a passive device used for splitting and combining light in integrated optics. It is based on the principle of self imaging [5]. In a multimode waveguide, the input mode profile is reproduced in single or multiple images along the direction of propagation in the multimode waveguide.This section provides a general operating principle of MMI's and is based on the more detailed theory and applications of MMI devices provided in [5].

The main structure of an MMI is the multimode waveguide which is designed to support large number of modes. An input wave is launched in the multimode waveguide and then recovered at the output using access waveguides. The access waveguides are placed on either side of the multimode section to form an NxM MMI coupler. Shown in Fig. 1.7 is the schematic of a 2x2 MMI coupler. The multimode section supports $m = 0, 1, 2...(n-1)$ number of lateral modes as shown in Fig. 1.8. The propagation constant of the excited modes in the multimode section has a quadratic relationship with the mode number $(m)$ and is given by [5],

$$\beta_m \simeq k_0 n_r - \frac{(m+1)^2 \pi \lambda_0}{4 n_r W_e^2} \tag{1.7}$$

where $k_0 = \frac{2\pi}{\lambda_0}$, $\lambda_0$ is the free space wavelength, $n_r$ is the material refractive index of the multimode section and $W_e$ is the effective width of the multimode section taking into account the evanescent decay of the mode into the cladding. From equation (1.7),the beat length ($L_\pi$) for the two lowest order modes is,

$$L_\pi = \frac{\pi}{\beta_0 - \beta_1} \simeq \frac{4 n_r W_e^2}{3\lambda_0} \tag{1.8}$$

with propagation constant difference of the modes in terms of the beat length as,

$$(\beta_0 - \beta_m) \simeq \frac{\pi m(m+2)}{3L_\pi} \tag{1.9}$$


Figure 1.7: Schematic of a 2x2 MMI coupler.

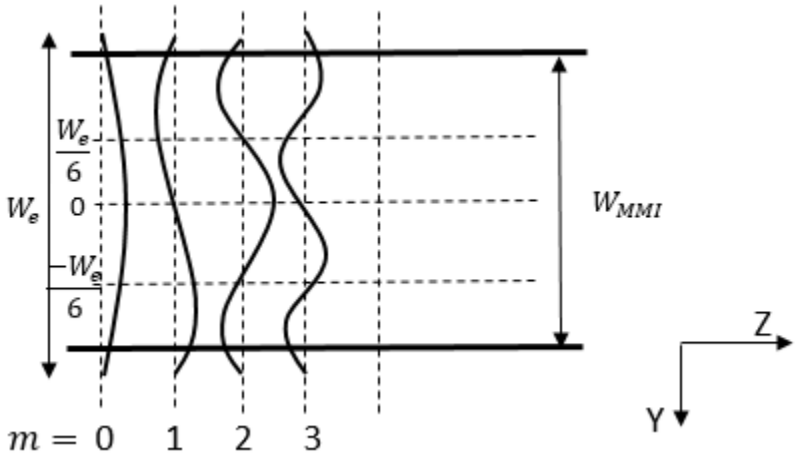


Figure 1.8: Example lateral field profiles in the multimode section.[5]

Consider an input field profile $\Psi(y, 0)$ present at $Z = 0$ as shown in Fig. 1.9.The

input filed $\Psi(y,0)$ can be decomposed as superposition of all the guided mode distributions $\psi_m(y)$ in the multimode section [5] and is given as,

$$\Psi(y,0) = \sum_{m=0}^{n-1} c_m \psi_m(y) \tag{1.10}$$

where $c_m$ is the field excitation coefficient. The field profile after a propagation

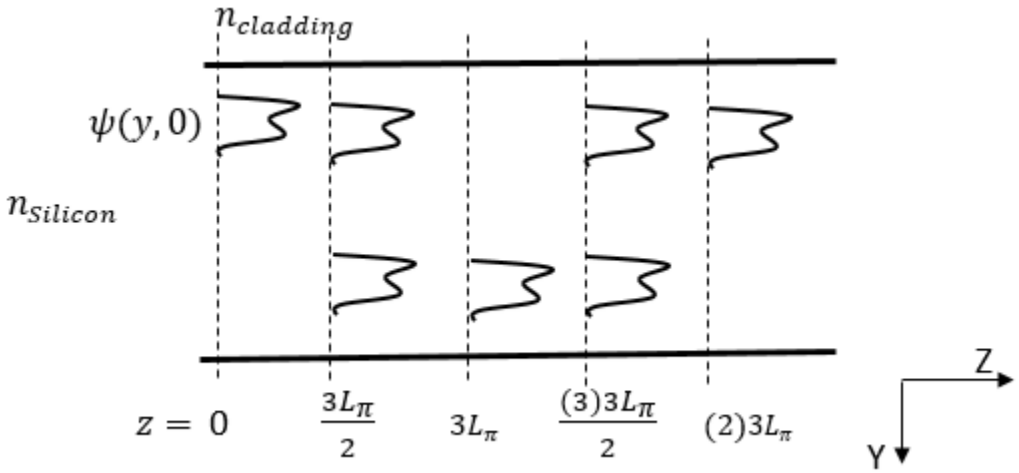


Figure 1.9: Multimode section show an input mode profile $\Psi(y,0)$ with a mirror self image at propagation distance of $3L_\pi$, direct self image at $(2)3L_\pi$ and two fold images at $\frac{3L_\pi}{2}$ and $\frac{(3)3L_\pi}{2}$.[5]

distance $Z = L$ is obtained to be as [5],

$$\Psi(y,L) = \sum_{m=0}^{n-1} c_m \Psi_m(y) e^{[\frac{j(m(m+2))\pi L}{3L_\pi}]} \tag{1.11}$$

We can observe from equation (1.11) that the field profile $\Psi(y,L)$ is dependant on the mode excitation coefficient $c_m$ and the phase factor,

$$[\frac{m(m+2)\pi L}{3L_\pi}] \tag{1.12}$$

At certain lengths of the MMI corresponding to multiples of $3L_\pi$, the field $\Psi(y,L)$ is a reproduction or a self-image of the input field $\Psi(y,0)$ as shown Fig. 1.9. At distances which are multiples of $\frac{3L_\pi}{2}$, we obtain a 2 fold self image of $\Psi(y,0)$ indicating 3dB splitting of the input field. Self imaging mechanisms in MMI which are independent of the modal excitation are called as general interference MMI and those

obtained by excitation of only certain modes are known as restricted interference MMI. Paired interference MMI is an example of restricted interference MMI where mode numbers 2,5,8,11,14... are not excited by placing the input excitation at a $y$ location that corresponds to zero crossing of the mode, as shown at $y = \pm\frac{W_e}{6}$ in Fig. 1.8. This way the length periodicity in the mode phase factor of (1.12) can be reduced by a factor of 3 [5].

Key metrics for the performance of a MMI include excess loss, imbalance in the output power and device size.The excess loss (EL) and imbalance (IB) for a 2x2 MMI shown in Fig. 1.7 are calculated through the equations,

$$EL(dB) = 10\log_{10}(\frac{P_{o1} + P_{o2}}{P_{in}}) \tag{1.13}$$

$$IB(dB) = 10\log_{10}(\frac{P_{o1}}{P_{o2}}) \tag{1.14}$$

where $P_{in}$ is the input power and $P_{o1}$, $P_{o2}$ are output powers in the individual output arms of the 2x2 MMI coupler. A detailed design procedure for high performance MMI couplers using a shallow etch rib waveguide on an SOI platform has been provided in [31].

### 1.2.3 Ring Resonators

Ring resonators in silicon also known as silicon micro ring resonators are compact wavelength selective devices. It consists of a straight waveguide and a looped or ring waveguide which is coupled to the straight waveguide. When the input wavelength is such that the optical waves in the ring waveguide acquire a round trip phase shift of an integer multiple of $2\pi$, the waves in the ring waveguide interfere constructively and the ring resonator is in a state of resonance [32].

There are two types of configurations namely, all-pass and add-drop ring resonators whose schematics are shown in Fig. 1.10. The all pass ring resonator also known as all-pass filter (APF) or a notch filter consists of a single straight waveguide and a coupled ring waveguide. The transmission intensity of an APF is given by equation (1.15) [32]

$$T_n = \frac{I_{pass}}{I_{input}} = \frac{a^2 - 2racos(\phi) + r^2}{1 - 2racos(\phi) + (ra)^2} \tag{1.15}$$

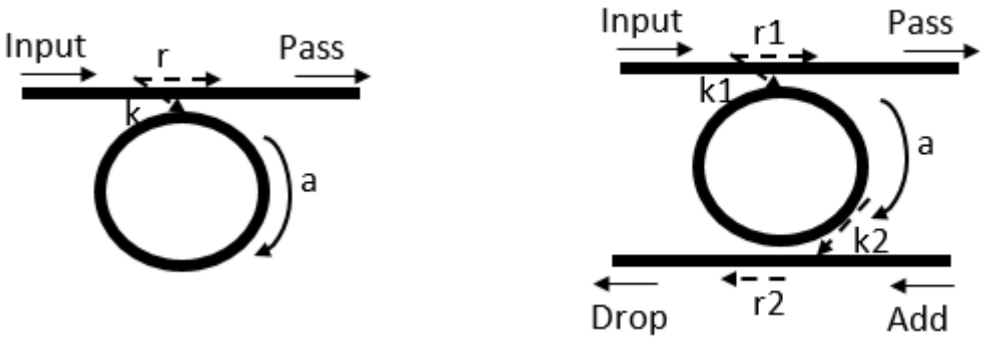


(a) (b)

Figure 1.10: Schematic of (a) All-pass (b) Add-drop ring resonators.

$\phi = \beta L$ is the single round trip phase shift, where $L$ is the circumference of the ring waveguide and $\beta$ is the propagation constant of the optical mode.$a$ is single round trip transmission that takes into account the propagation loss and coupling loss. $r$ is the self coupling coefficient, $k$ is cross-coupling coefficient such that $r^2 + k^2 = 1$ for a lossless coupler. The ring waveguide is in resonance when $\phi$ is an integer multiple of $2\pi$, which means that the optical path length in the ring waveguide is an integer multiple of the input wavelength.

$$m\lambda_{res} = n_{eff}L; m = 1, 2, 3... \tag{1.16}$$

The resonator is said to be critically coupled when the power coupled to the ring waveguide is equal to loss in the ring waveguide, i.e. when $1 - a^2 = k^2$ or $r = a$. Under critical coupling, transmission of the APF drops to zero at resonance.

Add-drop ring resonators have two straight waveguides that are coupled to the ring resonator. A part of the input field is transmitted to the drop port shown in Fig. 1.10(b). The normalized transmission intensity at the pass and drop ports are given by the following equations,

$$T_p = \frac{I_{pass}}{I_{input}} = \frac{r_2^2 a^2 - 2r_1 r_2 a cos\phi + r_1^2}{1 - 2r_1 r_2 a cos\phi + (r_1 r_2 a)^2} \tag{1.17}$$

$$T_d = \frac{I_{drop}}{I_{input}} = \frac{(1 - r_1^2)(1 - r_2^2)a}{1 - 2r_1 r_2 a cos\phi + (r_1 r_2 a)^2} \tag{1.18}$$

In the add-drop configuration, critical coupling occurs when $ar_2 = r_1$.

The spectral characteristics for ring resonators are shown Fig. 1.11. The transmission spectra which depend on the ring waveguide propagation loss and coupling loss

are calculated through equations (1.15),(1.17) and (1.18). In Fig. 1.8, example values of $a = 0.95$ and $r_1 = r_2 = r = 0.85$ are considered. Important spectral characteristics such as full width half maximum (FWHM) of the resonance, extinction ratio (ER) are also indicated for outputs at the pass port, drop port and for the notch filter.

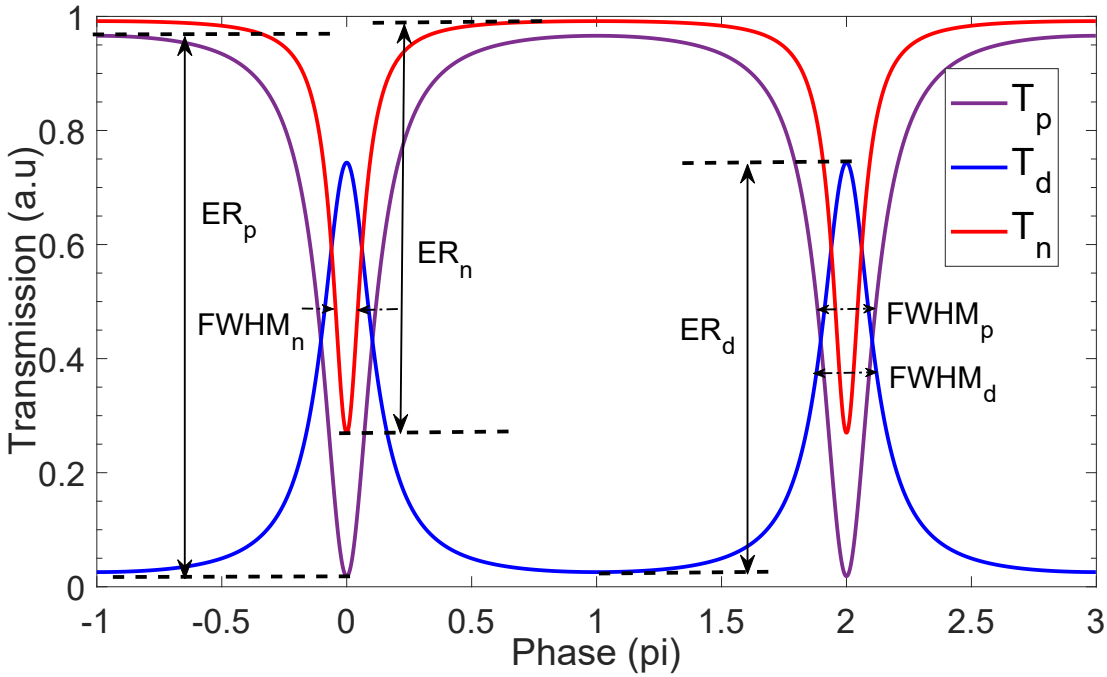


Figure 1.11: Transmission spectra for an all-pass ring (notch filter) and an add-drop ring resonator for $a = 0.95$ and $r_1 = r_2 = r = 0.85$ along with the indicated spectral characteristics.

From Fig. 1.11, we can observe that the add drop ring resonator has a greater extinction ratio than the all-pass ring as it operates closer to critical coupling for the considered $a, r_1, r_2, r$ values. Other important characteristics for ring resonators are the quality (Q) factor. Q factor indicates sharpness of the resonance around the resonant wavelength and is given as [32]

$$Q = \frac{\lambda_{res}}{FWHM} \tag{1.19}$$

Physically, Q factor indicates how many round trips are made before the optical energy in the ring decays to $1/e$ of the initial energy due to propagation loss or coupling to the bus waveguide [32]. This translates to how long the optical intensity

in the ring waveguide takes to decay by a factor of $1/e$ which is also known as resonator lifetime or cavity photon lifetime [33, 34].

### 1.2.4 Slot Waveguide Bragg Gratings

A slot waveguide structure allows for confinement and propagation of the optical mode in a low index medium [35, 36]. A silicon slot waveguide structure consists of two silicon arms separated by a narrow gap filled with a low index medium. The discontinuity in the dielectric medium at the silicon arm and slot region interface results in a strong optical field confined in the slot region. There are two types slot waveguide geometry, horizontal and vertical slot waveguide configurations as shown in Fig. 1.12. The electrical field ($E_x$) strength of the fundamental TE mode in a vertical silicon slot waveguide with oxide cladding is shown Fig. 1.13. We can observe a strong $E_x$ component of the optical mode in the narrow slot region.

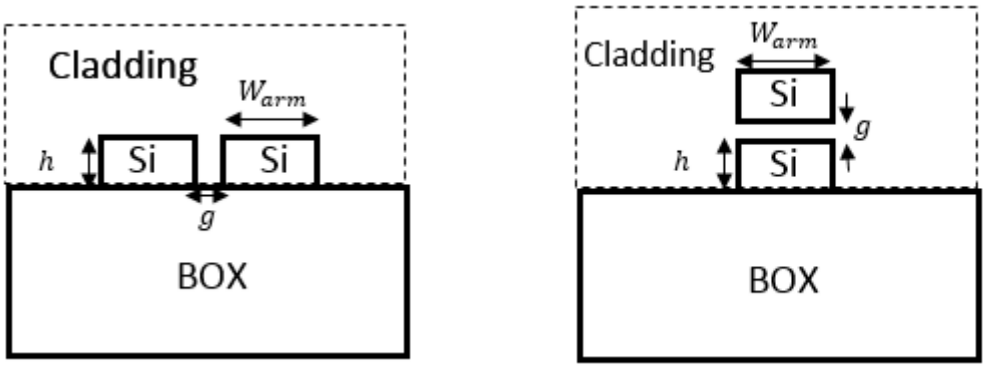


(a) (b)

Figure 1.12: Schematic of (a) Vertical slot waveguide (b) Horizontal slot waveguide. BOX: Buries oxide, Si: Silicon.

The slot waveguide Bragg gratings are unique structures which provide the advantage of using optical properties of the low index slot medium and the functionality of a Bragg grating structure. The schematic of the uniform Bragg grating structure with internal corrugations of width ($\Delta W_{in}$) and grating period ($\Lambda$) is shown in Fig. 1.14. A part of the incident light into the Bragg grating structure is reflected due to the grating corrugations and the rest is transmitted through. Depending on the wavelength of the input light, interaction of the input light and the grating structure

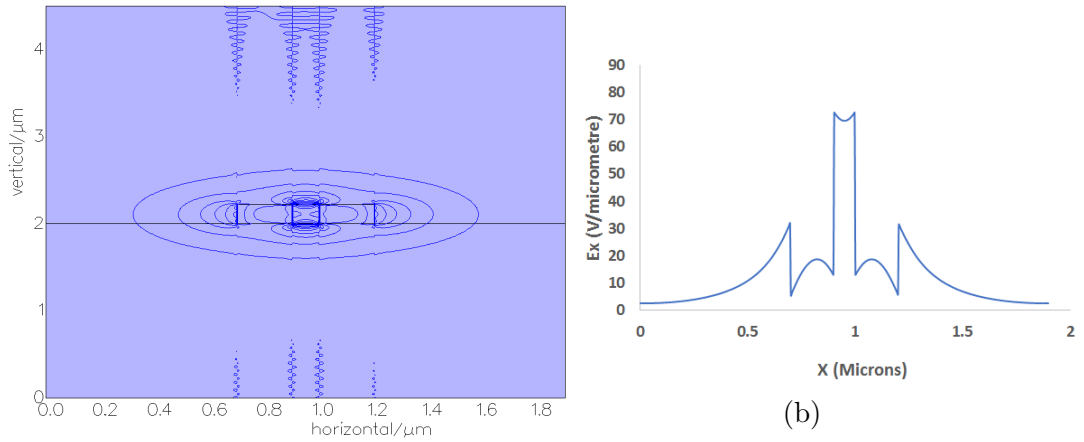


(a) (b)

Figure 1.13: Electric field ($E_x$) of the fundamental TE mode in vertical slot waveguide (a) Contour plot (b) $E_x$ field horizontal cross section profile.

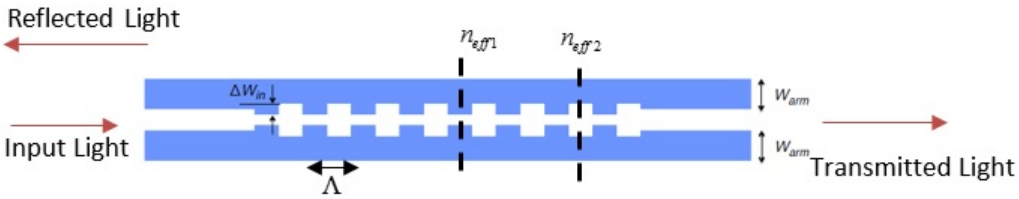


Figure 1.14: Top view schematic of a uniform vertical slot waveguide with internally corrugated Bragg gratings [6].

varies. At a particular wavelength, the reflected light waves occurring from multiple reflections due to the gratings interfere constructively to give a stop band in the transmission spectrum. This wavelength is called as the Bragg wavelength ($\lambda_B$) and is given as

$$\lambda_B = 2\Lambda n_{eff} \tag{1.20}$$

Here $n_{eff}$ is the average effective index. The bandwidth of the Bragg grating is defined as the wavelength separation between two successive maxima around the resonant stop band and is given as [30],

$$\Delta\lambda = \frac{\lambda_B^2\sqrt{(\kappa^2 + (\pi/L)^2)}}{\pi n_g} \tag{1.21}$$

Here $\kappa$ is the grating coupling coefficient, L the grating length and $n_g$ is the group index of the uncorrugated waveguide at the Bragg wavelength. The grating coupling coefficient refers to the amount of reflection per unit length and can be calculated

from the Fresnel's equations [30],

$$\kappa = \frac{2\Delta n}{\lambda_B} \tag{1.22}$$

Here $\Delta n = n_{eff1} - n_{eff2}$.

The typical response of a uniform Bragg grating is shown in Fig. displaying its wavelength selective transmission capabilities.

## 1.3 Thesis Outline

The organization of my thesis is divided into three main chapters. Each chapter describes a specific project I worked on in the field of silicon photonics.

Chapter 2 describes the project on Micron scale silicon photonics. This project was part of the internship at Lumentum LLC in Ottawa, Canada. Design of a single mode rib waveguide, fabrication process used and design of a polarization beam splitter using micron scale SOI thickness is described.

Chapter 3 describes the project on silicon optical modulators. The state of art in the field of silicon optical modulators is described. This is followed by detailed design of a novel ultrafast DC Kerr effect modulator with theoretical background, resonator structure implementation and photonic circuit simulation.

Chapter 4 describes silicon nanowire Mach Zehnder Interferometer (MZI) circuits and Slot waveguide Bragg gratings. The theory, modeling and simulation of MZI and slot waveguide Bragg gratings is presented. This is followed by e-beam fabrication process used in the multi-project wafer fabrication run and measurement data analysis. Novel low loss slow light property of slot waveguide Bragg gratings is described through simulation and experimental results and its potential application for high performance electro-optic modulators and integrated-optic sensors is discussed.

Finally, conclusions and future work from this thesis are summarized in chapter 5.

# Chapter 2

# Micrometer Scale Silicon Photonics

## 2.1 Introduction

Micrometer scale silicon photonics is an attractive platform to develop commercially viable products such as passive waveguides , switches, attenuators and filters relevant for optical transport applications.[1] This is because it can provide low insertion loss, and weak birefringence compared to nanometer scale silicon photonics. This is particularly well suited for single mode fiber-optic applications.

Commercial development of silicon photonics was led by Bookham Technologies, U.K in the 1990s during the telecom boom [37]. This was in part due to the research breakthroughs achieved in the late 1980s by G. Reeds group at the University of Surrey and by R.A Soref who was collaborating with Surrey University. Specifically, fabrication of silicon waveguides on a silicon-on-insulator (SOI) platform at telecom wavelengths (1.2-1.6 microns) was proposed. Issues of multi modal nature of micron scale strip waveguides and polarization dependent losses due to birefringence were investigated. In 1991, Soref et. al. proposed a theoretical condition on the micron scale rib waveguide dimensions to achieve single mode criteria in rib/ridge waveguide based on an SOI platform [38]. The idea involved designing the rib waveguide dimensions (slab height and rib width) such that higher order modes in the rib waveguide would couple into the fundamental slab mode and would experience significant side power loss due to lateral leakage to make the rib waveguide effectively single mode. The theoretical predictions showed reasonable agreement with experimental results for single mode SOI rib waveguides in [39].

Industrial application of micron scale silicon photonics has been demonstrated by

[1] A version of the this chapter is part of the technical report, D.V Simili , "Micron Scale Silicon Photonics for Optical Communication", Lumentum LLC, Ottawa, ON, December 2016. Exact device design dimensions are withheld in this chapter as per confidentiality agreement with Lumentum.

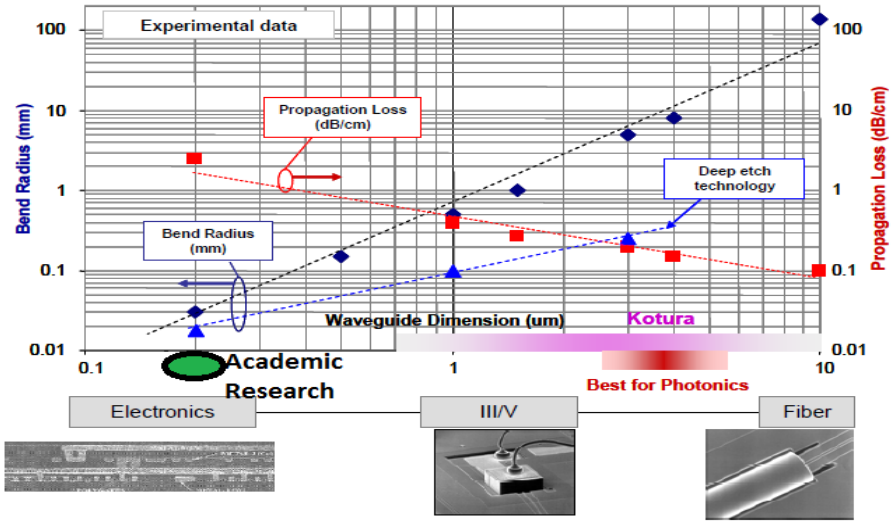


Figure 2.1: Propagation loss and bend radius versus waveguide dimensions [7]

Mellanox [7]. Figure 2.1 describes propagation loss and minimum bend radius performance for different waveguide thicknesses. As the waveguide thickness decrease, propagation loss increases because the mode is now closer to the waveguide sidewall resulting in a higher scattering loss. Though academic research is mainly focussed on nanometer scale silicon photonics as it allows for more compact devices due to tighter bend radii of nanometer scale strip waveguides and potential integration with nanometer scale electronics, Industrial research by Mellanox suggests 2-4 $\mu m$ waveguide thickness as a suitable platform for optical transport. This is because it offers superior propagation loss performance, better coupling from the chip to optical fiber and easier coupling to III/V group semiconductor components used for lasers and detectors. Secondly Mellanox has developed a multilayer etch fabrication capability with deep etch technology that allows for tighter bend radii in micron scale waveguide thicknesses as shown in Fig. 2.1. Other advantages of micron scale silicon waveguides are low propagation loss of 0.2 dB/cm for both TE and TM polarizations and negligible birefringence($\sim 10^{-4}$) [7].

This chapter is part of my industrial internship experience at Lumentum LLC in Ottawa, Canada. The design of single mode rib waveguide that is compatible with external fabrication foundry used by Lumentum LLC is described in section 2.2. The CMOS compatible fabrication process used by the external foundry is described in section 2.3. Section 2.4 describes the detailed design of a polarization beam splitter

device that is compatible with available fabrication process. Details of the fabricated polarization beam splitter and experimental data from my designs are not provided because of Lumentum LLC's proprietary on them.

## 2.2 Design of single mode rib waveguide

An important requirement in the design of a micron scale rib waveguide is that it support propagation of only the fundamental TE and TM modes in order to prevent loss of optical power from fundamental mode to higher order modes.The cross section of a rib waveguide is shown in Fig. 2.2. The theoretical condition for single mode operation in a rib waveguide was first predicted by Soref. et. al. [38]. The condition proposed is as follows,

$$t<c+(r/\sqrt{(1-r^2)}) \tag{2.1}$$

Here, $r = h/H, t = W/H, c = 0.3$ and $r \leq 0.5$ . Experimental results have shown agreement with the proposed Soref condition as in the academic publication [39] and also industrial research publications by Mellanox [40] and Intel [41]. The proposed rib waveguide geometry design are so that the etch depth and rib width chosen satisfy the Soref criteria. Fundamental TM and TE modes of the proposed rib waveguide are shown in Fig. 2.3 indicating negligible birefringence.

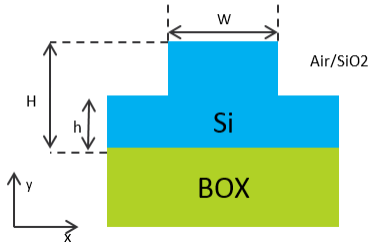


Figure 2.2: Cross section of a rib waveguide.

## 2.3 Fabrication Process

The fabrication process steps used to develop the SOI rib waveguide are shown in Fig. 2.4 with a micron scale SOI (Silicon on Insulator) layer on a 3 micron BOX (Buried Oxide layer)[42]. The process is also referred to as the single etch process.

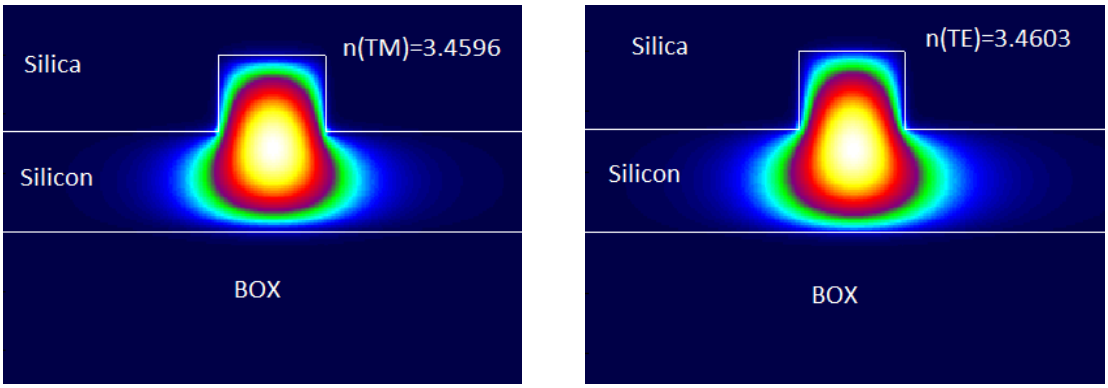


(a) (b)

Figure 2.3: Color coded fundamental TM (a) and TE (b) modes in the designed rib waveguide showing negligible birefringence ($\sim 10^{-4}$) at 1550 nm.

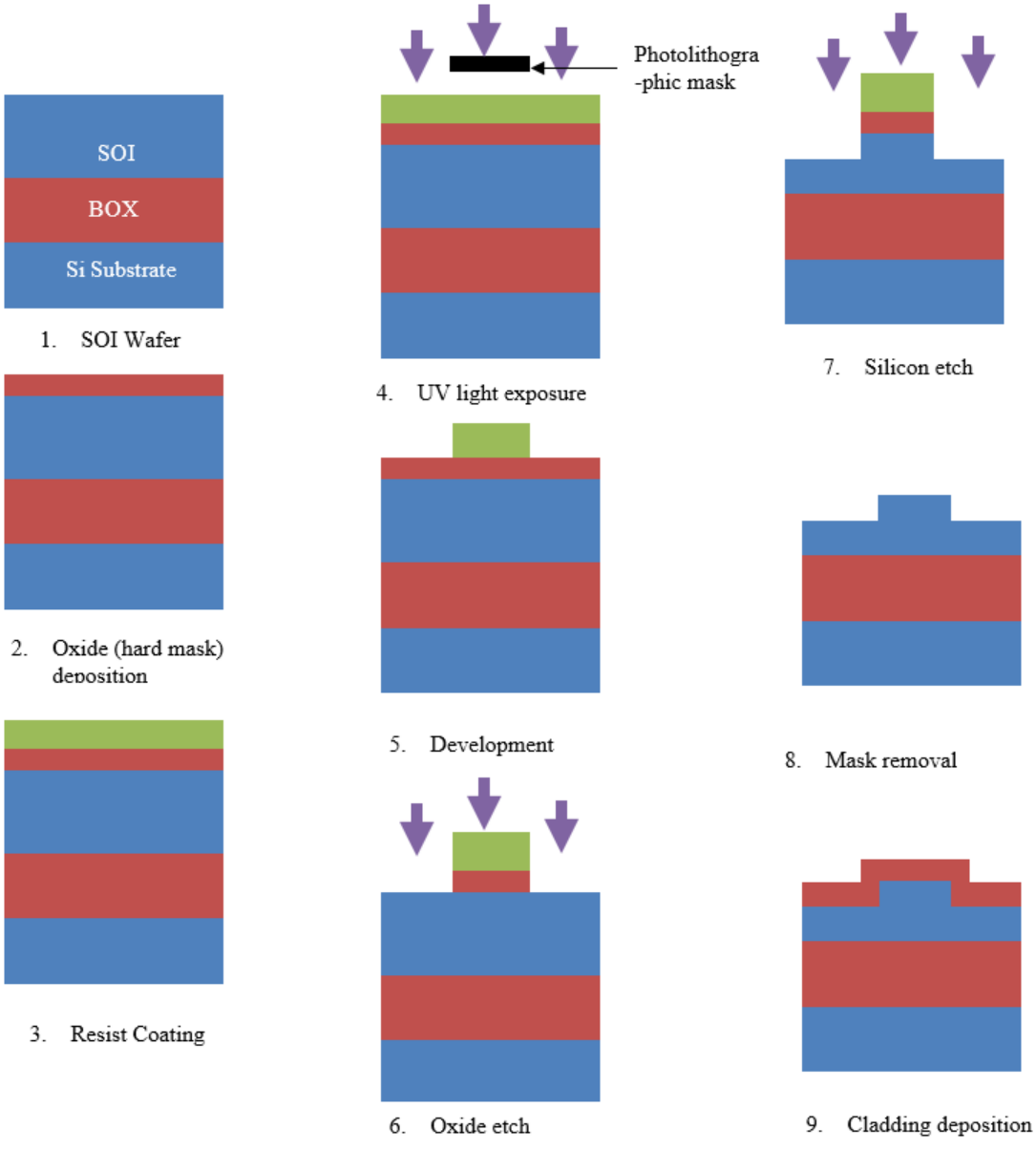


Figure 2.4: Fabrication process steps for single etch rib waveguide.

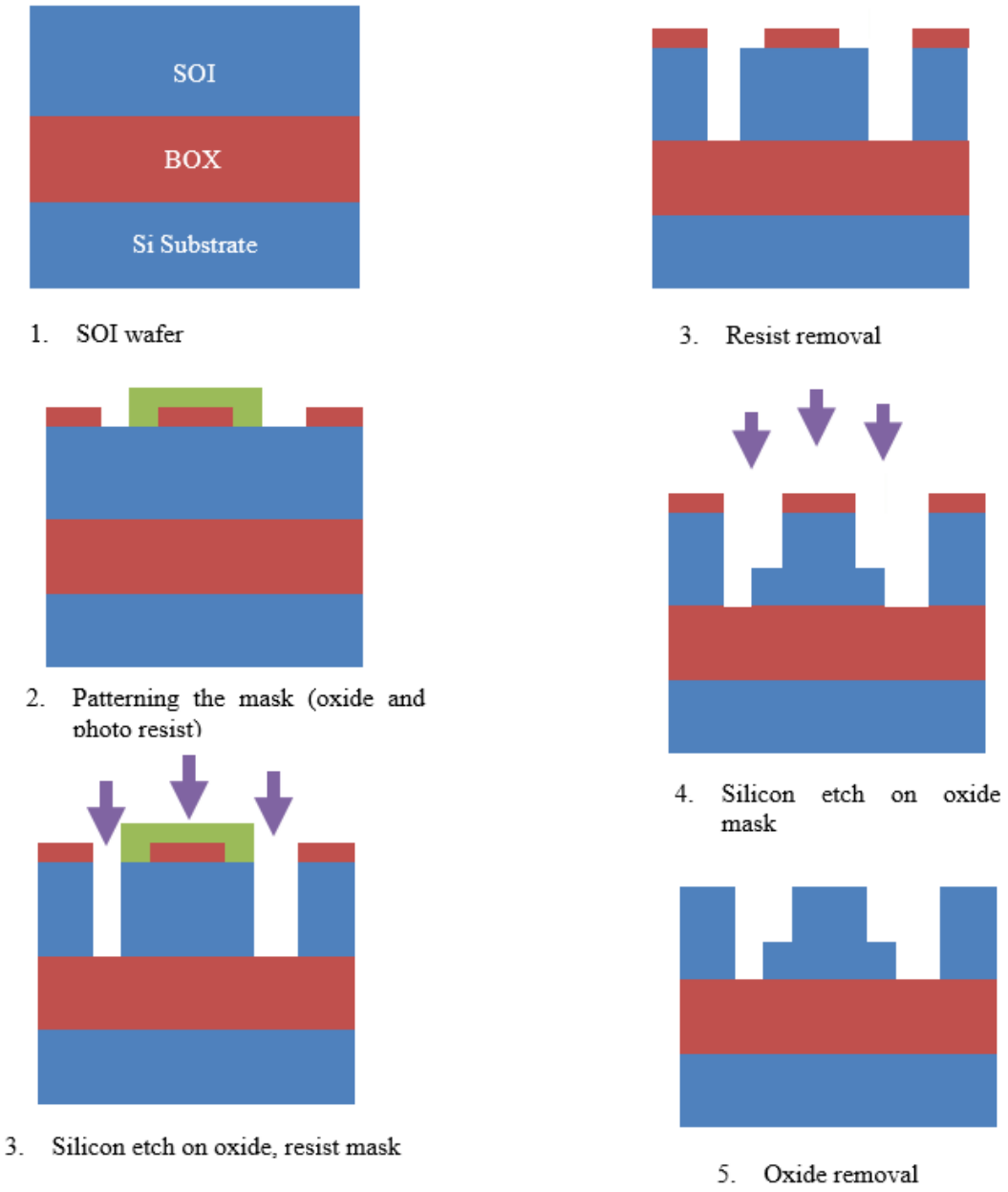


Figure 2.5: Fabrication process steps for double etch rib waveguide [8].

The oxide hard mask is deposited on the SOI wafer in order to protect the waveguide top surface during the silicon etch step. The pattern of the photomask which includes the waveguide structure is transferred to the oxide mask using the photolithography steps of resist coating, exposure and development followed by oxide dry etch.The waveguide pattern is transferred to the SOI layer after the silicon etch and mask removal steps. The cladding oxide is deposited using the TEOS (tetra-ethyl

ortho silicate process) process.

It is desirable to have a two etch depth fabrication process as shown in Fig. 2.5, because this would enable patterning the SOI layer with a rib waveguide and a strip waveguide. This is useful for certain applications such as bend sections, where a strip waveguide would be more advantageous as it requires a lower bend radius compared to a rib waveguide for the same bend loss [43].

## 2.4 Polarization Beam Splitter Design

A polarization beam splitter (PBS) is an important functional element in an integrated-optic chip. Its function is to route the fundamental TE and TM modes onto two separate paths. Its one of the functional units for applications such as a coherent communication on a chip [3], where to increase system bandwidth polarization multiplexing is used.

There are different techniques to implement a PBS such as using a single 2x2 multi mode interference [44, 45] (MMI ) coupler, an asymmetric MZI (Mach-Zehnder Interferometer) structure [46], directional couplers [47] and using photonic crystals [48]. The single 2x2 MMI design is based on the principle of quasi-state imaging. Due to birefringence of the multimode waveguide, the self imaging lengths for TE ($3L_{\pi}^{TE}$) and TM ($3L_{\pi}^{TM}$) polarizations are different. By adjusting the length of a single 2x2 MMI ($L_{MMI}$) such that the condition ($L_{MMI} = p \times 3L_{\pi}^{TE} = q \times 3L_{\pi}^{TM}; p + q = odd$) [44] is satisfied, one can use intermediate states or quasi states of the mode to achieve polarization splitting. Devices based on this principle had excess loss $\sim$ 1 dB and polarization extinction ratio of 11.93 dB and 14.35 dB for TE and TM polarizations at 1550 nm wavelengths respectively [45]. PBS based on directional couplers rely on strong birefringence in the waveguide as in silicon nanowires so the that cross over length and subsequent phase matching is satisfied for only one polarization. An asymmetric coupling between a silicon nanowire or strip waveguide and a slot waveguide was used to achieve an ultrashort PBS with a coupling length of 13.6$\mu$m and polarization extinction ratio of 21 dB and 17 dB for TE and TM polarizations over the telecom C band [47]. This type of PBS based on directional couplers is better suited for nanometer scale silicon photonics as it requires coupling gaps in the range of 100's of nm and features sizes of 100 nm or smaller when using slot

waveguides, making the designs fabrication sensitive. Similarly PBS based photonic crystals which utilize strong polarization dependent properties of photonic crystal structures, require feature sizes of the order of 100's of nm making them unsuitable for the micron scale fabrication process described in this chapter. Only the single 2x2 MMI and the asymmetric MZI based structures have a minimum required feature size that is greater than one micron. This condition of having a minimum feature size greater than one micron, so as to be compatible with the available micron scale SOI fabrication process limits available design options.

The schematic for an MZI based PBS is shown below,

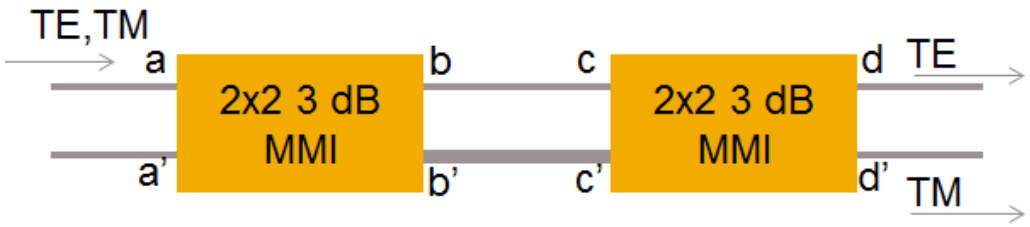


Figure 2.6: Schematic of a polarization beam splitter

Building blocks involved in the design are (a) 2x2 MMI 3 dB splitter, and (b) asymmetric birefringent MZI arms. The 2x2 MMI achieves 3 dB splitting of the input and by controlling the phase difference between the two MZI arms, one can achieve polarization splitting at the output. This is described through the equations below [46].

The electric fields at the output ports are given by the matrix relationship in equation (2.2).

$$\begin{bmatrix} E_d \\ E_d' \end{bmatrix} = \begin{bmatrix} k_{ad} & k_{a'd} \\ k_{ad'} & k_{a'd'} \end{bmatrix} \begin{bmatrix} E_a \\ E_{a'} \end{bmatrix} \tag{2.2}$$

where the coupling ratios are,

$$k_{ad} = k_{ab}k_{bc}k_{cd} + k_{ab'}k_{b'c'}k_{c'd}$$

$$k_{ad'} = k_{ab}k_{bc}k_{cd'} + k_{ab'}k_{b'c'}k_{c'd'}$$

$$\begin{bmatrix} k_{ab} & k_{a'b} \\ k_{ab'} & k_{a'b'} \end{bmatrix} = \begin{bmatrix} k_{cd} & k_{c'd} \\ k_{cd'} & k_{c'd'} \end{bmatrix} = \begin{bmatrix} \sqrt{1-K} & -j\sqrt{K} \\ -j\sqrt{K} & \sqrt{1-K} \end{bmatrix}$$

This gives the coupling ratios as,

$$k_{ad} = K\gamma_{b'c'}e^{-j\beta' l_{b'c'}} \left[ \frac{(1-K)\gamma_{bc}e^{-j\Delta\varphi}}{K\gamma_{b'c'}} - 1 \right] \tag{2.3}$$

$$k_{ad'} = -j\sqrt{K(1-K)}\gamma_{b'c'}e^{-j\beta' l_{b'c'}} \left[ \frac{\gamma_{bc}e^{-j\Delta\varphi}}{\gamma_{b'c'}} + 1 \right] \tag{2.4}$$

$$\Delta\varphi = \beta l_{bc} - \beta' l_{b'c'} \tag{2.5}$$

where $K_{bc} = \gamma_{bc}e^{-j\beta l_{bc}}$, $K_{b'c'} = \gamma_{b'c'}e^{-j\beta' l_{b'c'}}$.Here $\beta = nk_0$ and $\beta' = n'k_0$ are propagation constants. $l_{bc}$ and $l_{b'c'}$ are lengths of the two MZI arms, K is the power coupling ratio ,$\gamma_{bc}$ and $\gamma_{b'c'}$ are the amplitude attenuation coefficients for the two MZI arms. Equations (2.3) and (2.4) describe the power coupled to the output ports d and d′ with the input from port a. From equations (2.3) and (2.4), we can observe that the outputs at ports d and d′ can be controlled through the phase difference between the two MZI arms $\Delta\varphi$ described in equation (2.5). This can be physically achieved by having MZI arms of different rib widths and/or arms of different lengths.

To achieve polarization splitting in the two output arms , the following phase difference conditions would be required,

$$\Delta\varphi = (2m+1)\pi \tag{2.6}$$

$$\Delta\varphi = (2m)\pi \tag{2.7}$$

Here $m$ is an integer.The phase difference in equation (2.6) would result in $k_{ad} = 1$ and $k_{ad'} = 0$, while the phase difference in equation (2.7) would result in $k_{ad} = 0$ and $k_{ad'} = 1$, when $K = 0.5$. Therefore, it is desirable to have 3 dB splitting from the 2x2 MMI's with negligible imbalance between the two output arms.There are two design options, namely a completely shallow etch design with a single etch depth of e $\mu$m or a deep etch design.

The key performance metrics of the PBS with reference to Fig. 2.6 include device excess loss (EL) and polarization extinction ratio (PER) given by

$$EL = 10\log_{10}(\frac{P_d + P_d'}{P_a})$$

$$PER = 10\log_{10}(\frac{P_d}{P_d'})$$

along with device bandwidth and device size. In the following sections, designs of the two fundamental building blocks which are 2x2 3 dB MMI and MZI arms using only a shallow etch are described.

### 2.4.1 Shallow Etch MMI Design

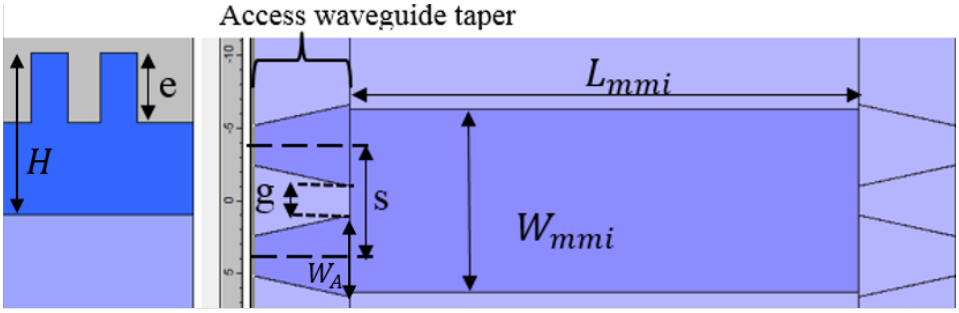


Figure 2.7: Schematic of a shallow etch MMI along with cross section of the access waveguide taper.

The design of the 2x2 MMI shallow etch is based on the R. Halir et. al. design procedure of the shallow etch 2x2 MMI [31]. The design steps are as follows,

1. Determination of the MMI access waveguide width.
2. Taper design.
3. Access waveguide separation.
4. MMI Block design.
5. Fabrication tolerance.

Step 1: Determination of MMI access waveguide width.

Having a wider access waveguide to the MMI provides better mode matching of the input waveguide to the wide multi mode section which then results in lower insertion losses and imbalance from the MMI. As per [31], design criteria for the access waveguide width in order for the MMI to have an excess loss below 0.1 dB is,

$$(W_A/H) \geq 3.01 - 2.95(e/H) \tag{2.8}$$

Here $W_A$ is the access waveguide width, H is the device layer thickness and e is the etch depth as shown in Fig. 2.7. Also, having a wider access waveguide increases the fabrication tolerance of the MMI [5].

Step 2: Taper Design

An adiabatic taper needs to be designed to gradually transition from the nominal rib waveguide width of 'w' $\mu$m to the wide access waveguide width of $2.07 \times w$ $\mu$m. The full vectorial FDM algorithm was used to simulate the propagation of the fundamental TE and TM modes.As the input waveguide is single mode as per design, no higher order modes should exist at the beginning of the taper.The boundaries for simulation of the taper are adjusted so that the fundamental mode electric fields completely decay before the boundary and the computation window is minimized. This would eliminate any unwanted reflection from the boundaries and reduce the computation time while maintaining the accuracy determined by the number of modes and grid size. The plot below shows the converged results for simulation of the taper.

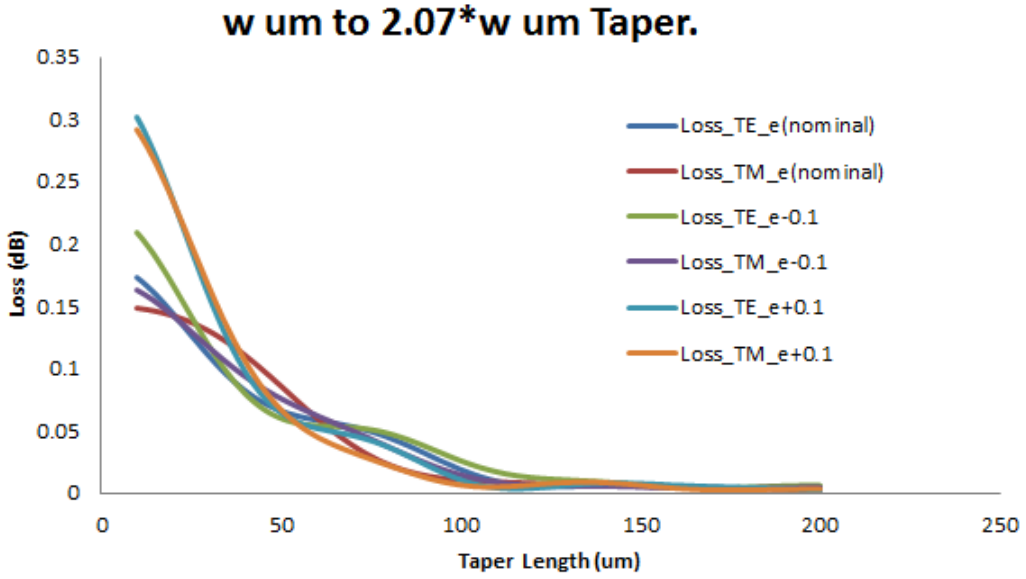


Figure 2.8: Excess Loss of the fundamental modes versus the taper length

We can observe that at a taper length of 150 $\mu m$, the loss in the fundamental TE and TM modes are below 0.05 dB for the nominal etch depth 'e' and also for 'e-0.1$\mu m$'

and 'e+0.1 $\mu m$' etch depths. The tapers were simulated using planar sections with constant widths at the input and output ends.

Step 3 : Access Waveguide Separation

A minimum separation gap between the access waveguides is required to ensure that the access waveguides to the MMI are practically decoupled, that is the coupling is lower than -30 dB. A small separation gap is desired as this would result in a small width for the MMI and therefore a more compact device. The limiting factors for the design are minimum separation gap that is allowed through the fabrication process and the coupling level for the two parallel access waveguides. The amount of coupling between two parallel waveguides is defined [31]as

$$C = 10 \times log \frac{Pout}{P_{in}} \tag{2.9}$$

The estimate for actual coupling between the two tapers can be obtained by analyzing parallel rib waveguides. By obtaining the coupling for parallel rib waveguides with widths $w$ $\mu$m and $(2.07 \times w)$ $\mu$m for a length of 150 $\mu$m, the actual coupling for the taper between $w\mu m$ and $(2.07 \times w)\mu m$ would lie in between these two extreme cases. This is a faster way to estimate the minimum separation gap required between the access waveguide tapers. From the analysis of [31], it is clear that the worst case scenario is when there is an etch depth error of -0.1 um from the nominal etch depth of e. This is because the fundamental modes have lower confinement in the rib section due to the etch depth error and therefore a stronger interaction between the parallel rib waveguides. The results presented for this step are for the worst case scenario for the etch depth of $(e - 0.1)\mu m$. It is found that when gradually increasing the center to center separation between the waveguides (s) to a value of (2.81 $\times$w) $\mu$m, the maximum parallel lengths are greater than the taper length of 150 um with coupling between them being below -30 dB. The corresponding separation gap at the access waveguides for the MMI is 2 $\mu$m which can be fabricated. Therefore the chosen s is (2.81 $\times$w) $\mu$m for the MMI design.

Step 4: Multimode Section

The design of the 2x2 multimode section can be either through general interference or paired interference mechanisms [5]. Design dimensions for the multimode section are MMI width ($W_{mmi}$) and MMI length ($L_{mmi}$) as shown in Fig. 2.7. The starting

widths for the general interference design is $W^G_{mmi} = (2W_A + g)\mu m$ and for the paired interference design is $W^P_{mmi} = 3(W_A + g)\mu m$ .

It is important to have relaxed tolerances in the MMI design to account for fabrication errors. The shift in MMI length from the nominal length (L) that results in 0.5 dB loss penalty is given by [5]

$$\delta L \cong \frac{(\pi n_r w_0^2)}{4\lambda_0} \tag{2.10}$$

In the above equation, $w_0$ is the Gaussian beam waist which equals the 1/e amplitude of the input field, $n_r$ is the material refractive index and $\lambda_0$ is the central wavelength of operation. The above equation gives the absolute length tolerance of the MMI independent of the MMI dimensions of width or length. We can observe that having a wider access waveguide would result in a greater MMI length tolerance because of the wide input field to the MMI. For the access waveguide rib width of (2.07 $\times$w)$\mu$m, the 1/e width for the fundamental mode is (1.74 $\times$w) $\mu$m. This gives a length tolerance of 38.6 $\mu$m , taking the silicon material refractive index of 3.45 and and the central wavelength as 1.55 $\mu$m.

The MMI length tolerance translates to width tolerance ($\delta W_e$), bandwidth ($\delta\lambda_0$) and refractive index tolerance ($\delta n_r$) through the following expression [5],

$$\frac{\delta L}{L} = 2\frac{\delta W_e}{W_e} \cong \frac{|\delta\lambda_0|}{\lambda_0} \cong \frac{\delta n_r}{n_r} \tag{2.11}$$

From the above expression , it can be concluded that the MMI length L needs to be as short as possible to allow for greater tolerances to other parameters (i.e. $W_e, \lambda_0, n_r$) in equation (2.5). This indicates optimizing the design to a shorter MMI width ($W_e$) would achieve a greater overall tolerance for the MMI. The 2x2 general interference MMI was optimized from a starting width of $W_{estart}$ to a final width of $W_{estart} - 0.6\mu m$. Decreasing the MMI widths in steps of $0.1\mu m$ improved the trade-off between the excess loss and imbalance for the MMI till the width of $W_{estart} - 0.6\mu m$ below which it got worse. Figures 2.9 (a) and (b) plot the variation of the excess loss and imbalance versus the MMI length at the wavelength of 1.55 $\mu m$ respectively. The chosen MMI length has a minimum excess loss of 0.11 dB and 0.10 dB for the TE and TM modes respectively and the imbalance is -0.13 dB and -0.06 dB for TE and TM modes respectively.

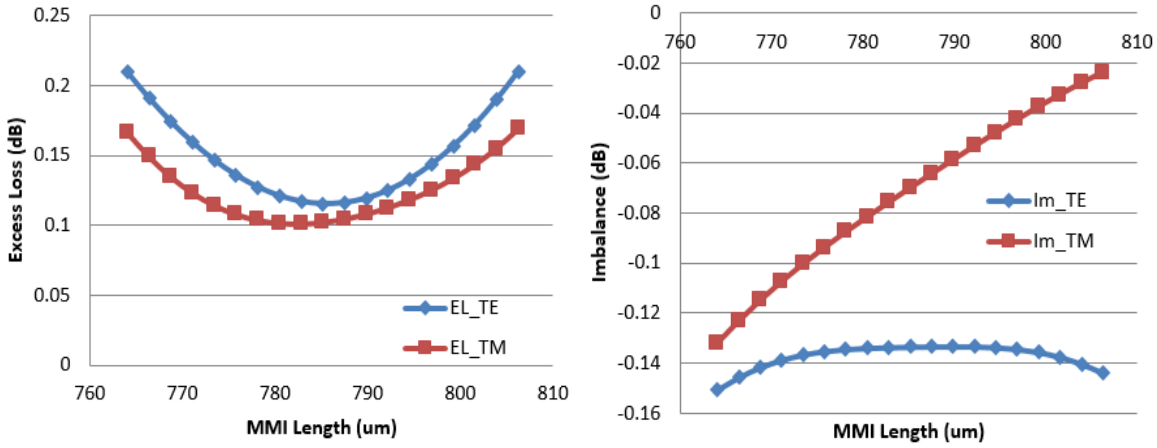


(a) (b)

Figure 2.9: (a) Excess loss versus MMI length (b) Imbalance versus MMI length at 1550 nm.

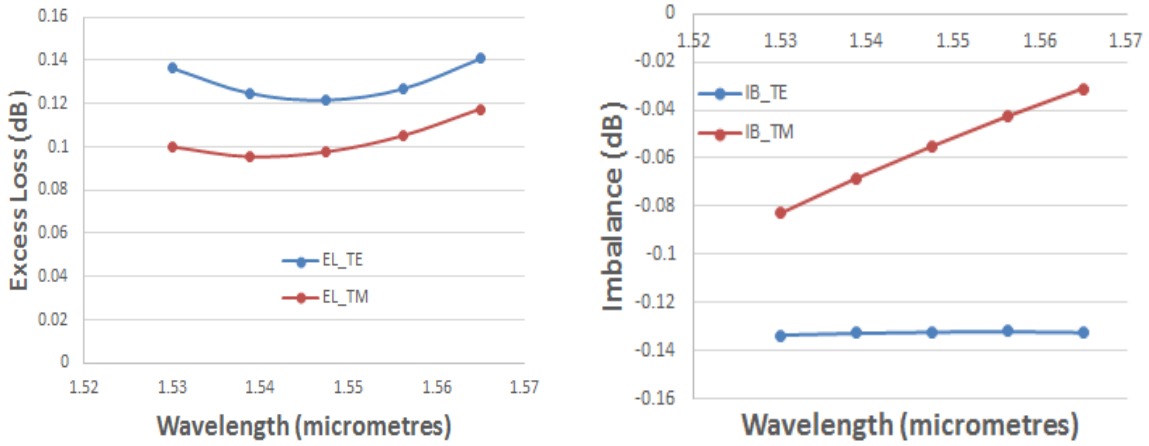


(a) (b)

Figure 2.10: (a) Excess loss versus wavelength (b) Imbalance versus wavelength.

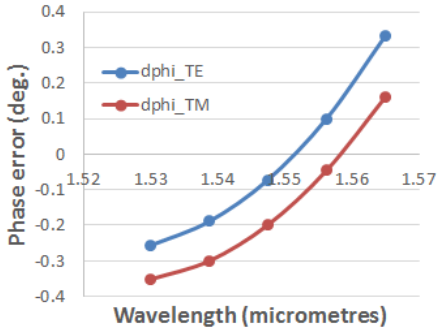


Figure 2.11: Phase error versus wavelength for the nominal design.

Figs 2.10 and 2.11 give the nominal shallow etch MMI design with respect to excess loss , imbalance and phase error. We can observe that maximum excess loss and imbalance is below 0.14 dB in the C band with phase error in the output below 0.4 degrees.

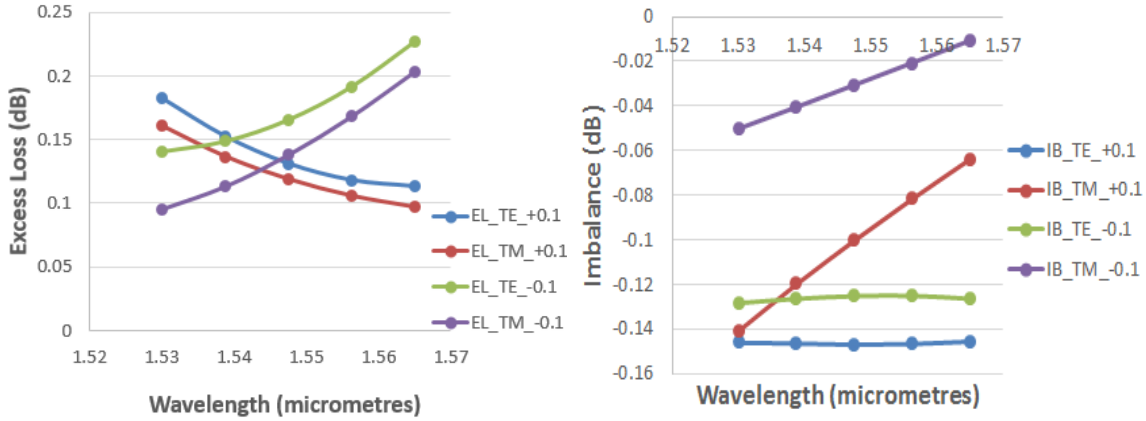


(a) (b)

Figure 2.12: Fabrication tolerance analysis for MMI width error of +/- 100 nm (a) Excess loss versus wavelength (b) Imbalance versus wavelength.

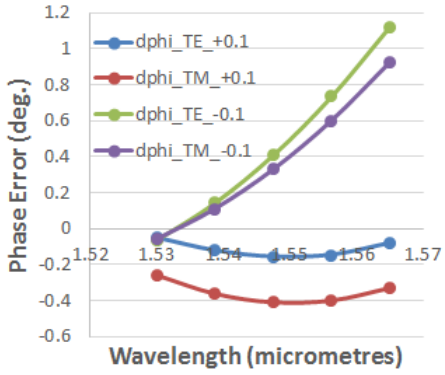


Figure 2.13: Phase error versus wavelength for fabrication width error of 100 nm.

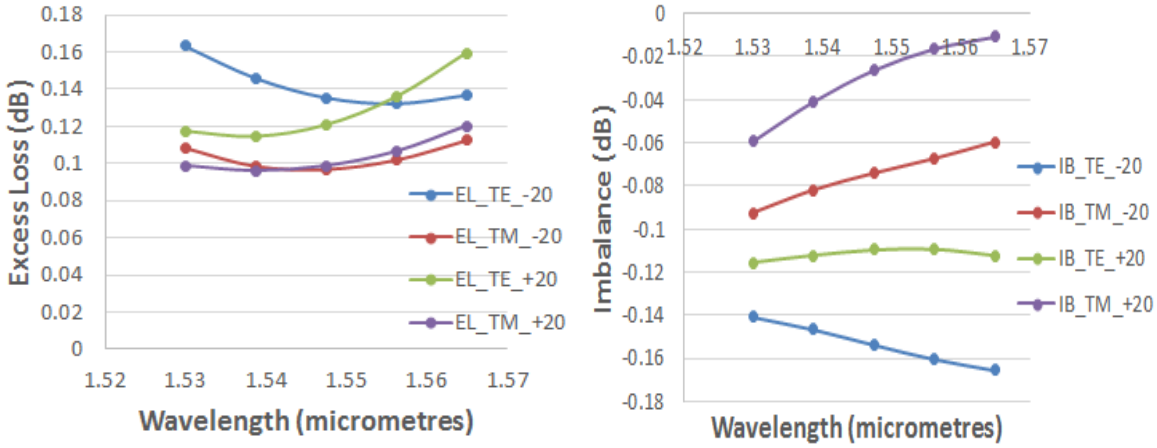


(a) (b)

Figure 2.14: Fabrication tolerance analysis for etch depth error of +/- 20 nm (a) Excess loss versus wavelength (b) Imbalance versus wavelength.

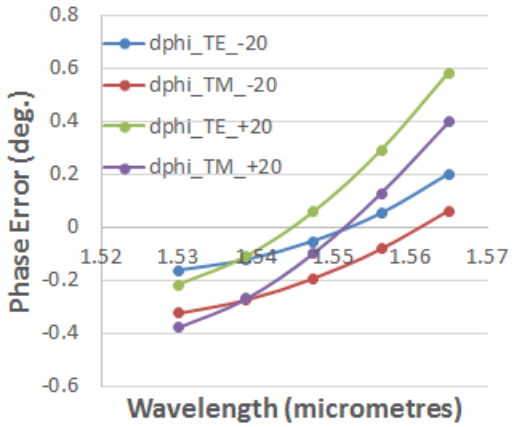


Figure 2.15: Phase error versus wavelength for fabrication etch depth error of +/- 20 nm.

Sensitivity of the nominal shallow etch design to MMI width error of +/- 100 nm and etch depth of +/- 20 nm are shown in Figs. 2.12-2.15. We can observe that excess loss and imbalance remains below 0.25 dB and 0.18 dB respectively while phase error has a maximum value of 1.12 degrees for these fabrication errors.

### 2.4.2 MZI Arm Design

Design of the MZI arms are based on governing equations for an MZI PBS which are described through equations (2.2-2.7).

One can choose the polarization with a higher imbalance from the 2x2 MMI splitter to satisfy the phase relationship in equation (2.10) as this phase condition does not require 50:50 splitting of the output power from the 2x2 MMI. From the analysis of the 2x2 MMI, the TE polarization has a higher imbalance than the TM polarization. Therefore the TE mode is selected to be output from the through port (d) and TM mode is output from the cross port (d′).

Thus, the phase relationships that need to be satisfied are as follows,

$$\Delta\varphi_{TE} = (n_{TE} - n'_{TE}l')(\frac{2\pi}{\lambda}) = (m_{TE} + 0.5)(2\pi) \tag{2.12}$$

$$\Delta\varphi_{TM} = (n_{TM} - n'_{TM}l')(\frac{2\pi}{\lambda}) = (m_{TM})(2\pi) \tag{2.13}$$

Here $n_{TE/TM}$ is the effective index of the wider arm and $l$ is its corresponding length. $n'_{TE/TM}$ is the effective index of the the narrower arm and $l'$ is the corresponding arm length. $m_{TE}$ and $m_{TM}$ are integers which correspond to the interference orders for the TE and TM modes respectively.

There are two unique design approaches, one in which the arms widths are equal with arm lengths being different and the other being unequal arm widths having an equal arm length. The option in which the arm widths are equal i.e. $n_{TE} = n'_{TE} = n_{TE0}$ and $n_{TM} = n'_{TM} = n_{TM0}$ would require the condition,

$$\frac{n_{TE0}}{n_{TM0}} = (\frac{m_{TE} + 0.5}{m_{TM}}) \tag{2.14}$$

As the ratio of the fundamental TE and TM mode effective indices for the rib waveguide with a fixed width are are close to 1.0, large interference orders (greater than 10) would be required to satisfy the condition in equation (2.14). This is would reduce the bandwidth of operation for the PBS and is therefore not desired.

The alternative approach of having unequal arm widths with an equal arm length would require the following condition to be satisfied,

$$(\frac{n_{TE} - n'_{TE}}{n_{TM} - n'_{TM}}) = (\frac{m_{TE} + 0.5}{m_{TM}}) \tag{2.15}$$

The advantages of this approach are that one would require smaller interference orders such as (1,2) to satisfy the condition in equation (2.15) and it is easier to draw the

physical layout with a constant arm length ($l_0$). The steps followed in this approach are based on the asymmetric MZI arm design described in [46]. These are as follows,

(1) Calculation of the effective indices for the fundamental TE and TM modes for rib widths in the range 1.0 $\mu m$ to 3.0 $\mu m$. These widths correspond to the single mode condition for the rib waveguides.

(2) Calculation of the ratio in equation (2.15) and determination of the allowed width combinations for the specific interference orders and the corresponding MZI arm lengths.

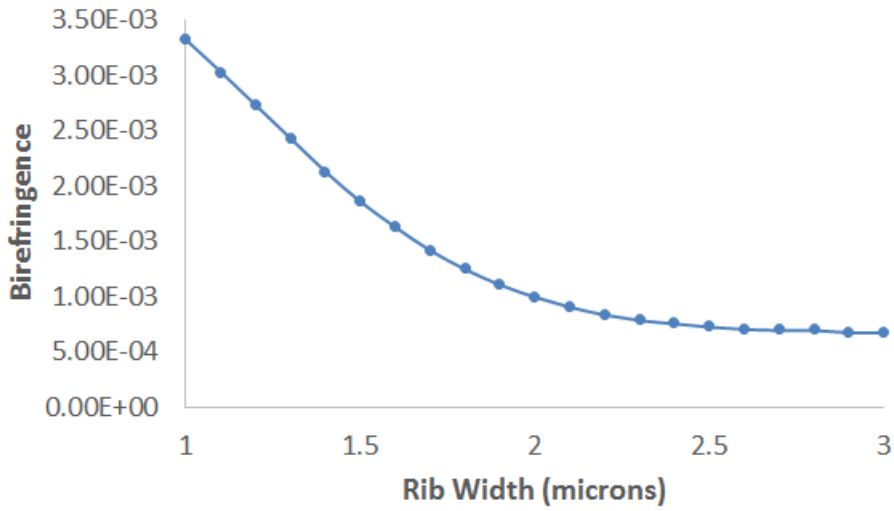


Figure 2.16: Birefringence versus waveguide width at 1550 nm.

Fig. 2.16 is the calculated waveguide birefringence for rib waveguides with varying rib width at 1.55 $\mu m$.

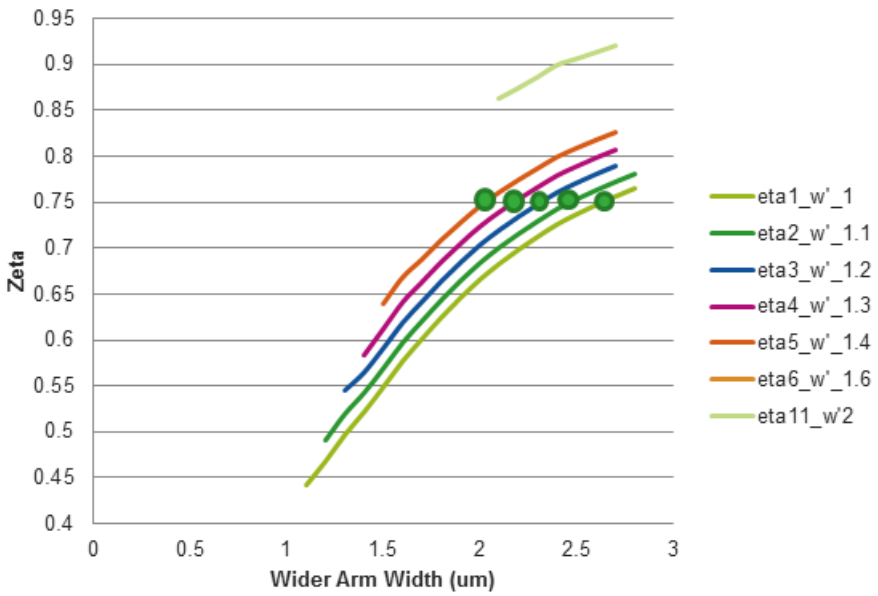


Figure 2.17: Zeta versus MZI wider arm width for a set of narrow arm widths

The above plot (Fig. 2.17) is a function of zeta versus the wider arm rib widths for the narrow arm widths in the range 1 um to 2 um. Here zeta is the ratio defined in equation (2.15) which is,

$$\zeta = (\frac{n_{TE} - n'_{TE}}{n_{TM} - n'_{TM}}) = (\frac{m_{TE} + 0.5}{m_{TM}}) \tag{2.16}$$

For interference orders of $(m_{TE}, m_{TM}) = (1, 2)$ , we have $\zeta$ equal to 0.75. This value of zeta is satisfied for a set of wide and narrow arm rib widths as shown in Fig. 2.17. The corresponding narrow and wide MZI arm rib widths are (1.0,2.7), (1.1,2.5), (1.2,2.3), (1.3,2.2) and (1.4,2) microns respectively. Other alternative options for MZI arm widths are (1.0, 1.3),(1.1,1.2) where interference orders are $(m_{TE}, m_{TM}) = (0, 1)$ with $\zeta = 0.5$.

## 2.5 Polarization Beam Splitter Simulation

Combining designs of the MMI and MZI arms described in section 2.4, performance of the MZI-based polarization beam splitter can be analyzed. Implementation of the MZI arms can be through a combination of tapers and straight waveguides. In this respect, one could have two designs with asymmetric and symmetric tapers. In the asymmetric taper design, there are two unequal tapers from the access waveguide to

the narrow and wide straight MZI arms. The layout schematic is shown below in Fig. 2.18 ,

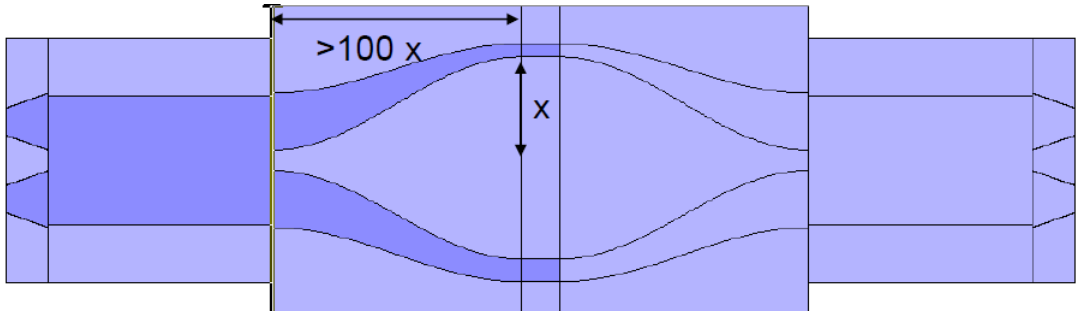


Figure 2.18: Schematic of shallow etch PBS with asymmetric MZI taper arms.

Nominal design performance for this design is shown in Figs. 2.19 and 2.20,

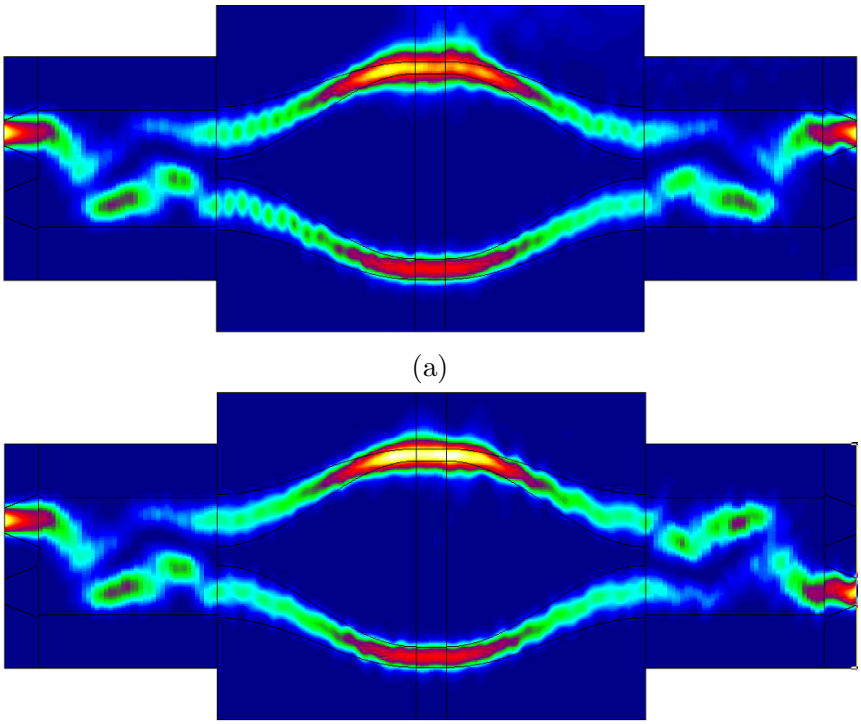

(a)

(b)

Figure 2.19: Nominal shallow etch PBS design Intensity plot (a) TE mode input (b) TM mode input.

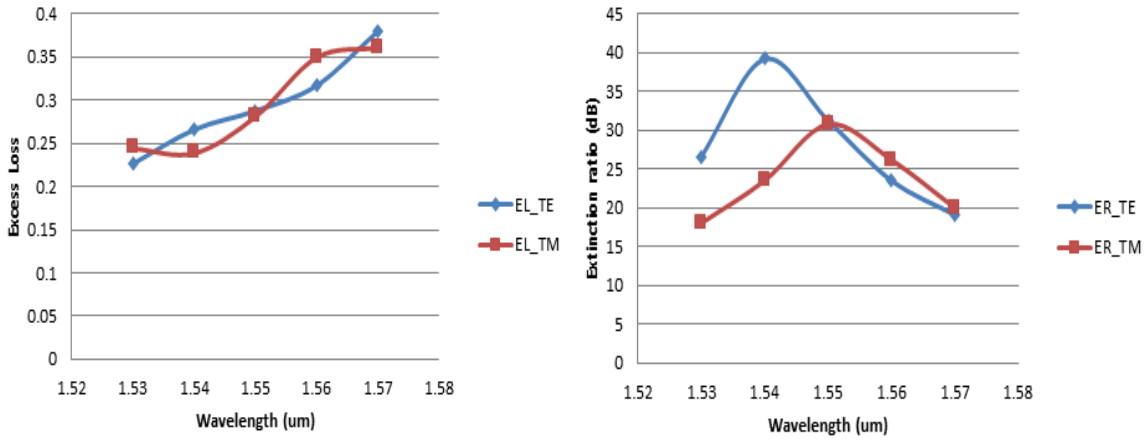


(a) (b)

Figure 2.20: Nominal shallow etch PBS design performance (a) Excess loss versus wavelength (b) Polarization extinction ratio versus wavelength.

The nominal design was obtained by increasing separation gap between the two straight MZI arms so as to ensure there is no coupling between the arms as this lowers extinction ratio of the PBS. After a certain separation distance the extinction ratio is limited by imbalance of the MMI and not by potential coupling between the two MZI arms. The above design is optimized so as to get close to 30 dB extinction ratio at the central wavelength of 1.55 $\mu$m.

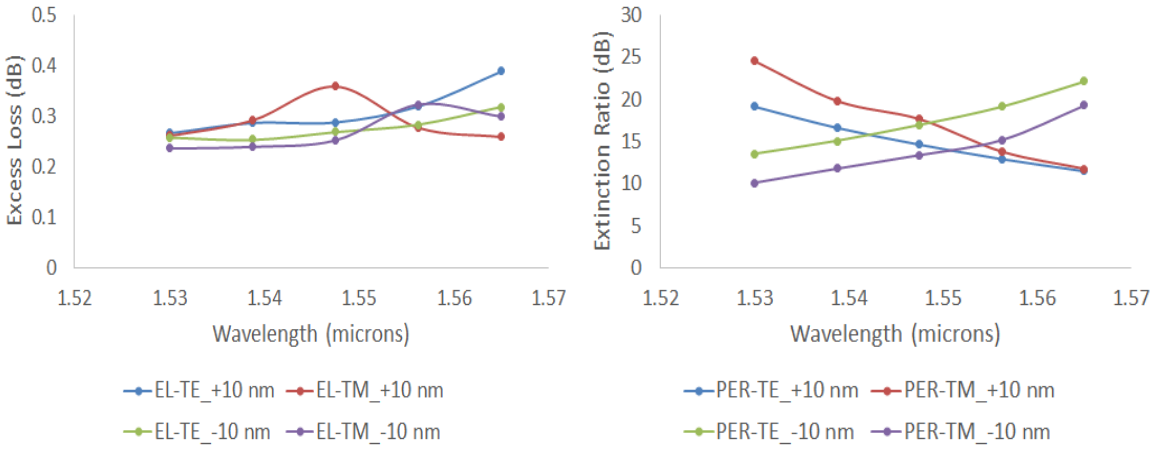


(a) (b)

Figure 2.21: Etch depth error analysis of +/- 10 nm from nominal PBS design. (a) Excess loss versus wavelength (b) Polarization extinction ratio versus wavelength.

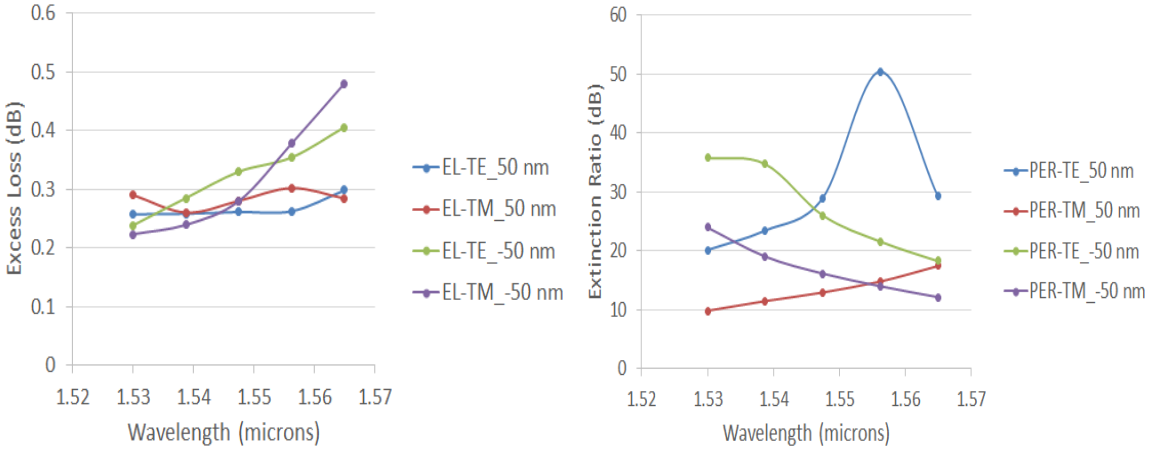


(a) (b)

Figure 2.22: Width error analysis of +/- 50 nm from nominal PBS design. (a) Excess loss versus wavelength (b) Polarization extinction ratio versus wavelength.

Fig. 2.21 (a) shows sensitivity analysis to etch etch depth error of +/- 10 nm from the nominal design of the shallow etch PBS. We can observe that the nominal PBS design is robust to +/- 10 nm etch depth error as excess loss is below 0.4 dB and polarization extinction ratio is better than 10 dB over C band wavelengths of 1530-1565 nm. Similarly the nominal design PBS shows good robustness for 50 nm width error with excess loss below 0.5 dB and polarization extinction ratio above 10 dB between 1530-1565 nm wavelengths as shown in Fig. 2.22.

## 2.6 Summary and Conclusion

The nominal design MZI PBS is summarized and compared with other MZI and a single 2x2 MMI based PBS in Table 2.1.

Table 2.1: Comparison of demonstrated PBS and the proposed nominal design PBS at 1550 nm wavelength.

| Design description | Excess loss (dB) | Extiction ratio-TE(dB) | Extiction ratio-TM(dB) | Device size (mm) |
|---|---|---|---|---|
| MZI with 2x2 MMI (400 nm SOI)[[49]] | 1-4 | 18 | 10 | 0.2 |
| MZI with 2x2 MMI (5.1 micron SOI)[[50]] | 1.1 | 16 | 16 | 10 |
| Single 2x2 MMI (Quasi state imaging) (Photodefinable Polyimide)[[45]] | 1 | 11.93 | 14.35 | 1.073 |
| Proposed nominal design(micron scale SOI) | 0.28 | 30 | 30 | 3-4 |

The proposed nominal design has the least excess loss of 0.28 dB and the highest extinction ratio of 30 dB for both TE and TM polarizations at 1.55 $\mu$m in comparison to other micron scale or nanometer scale MZI PBS and a micron scale single 2x2 MMI design.The simulation results predict excellent performance for the nominal design with device excess loss below 0.4 dB and polarization extinction ratio greater than 15 dB in the telecom C band (1530-1565 nm) for both TE and TM waves. The cost of micron scale MZI PBS performance over nm scale PBS is device size. The nominal design for the micron scale PBS is between 3-4 mm whereas a nm scale MZI PBS is $\sim$ 200 $\mu$m in length [49]. The device size of micron scale PBS could be reduced using a deep etch instead of shallow etch, but its sensitivity to fabrication errors would need to be analyzed.

A novel shallow etch polarization beam splitter (PBS) has been designed that is compatible with micrometer scale CMOS fabrication. The nominal design with its low excess loss, high polarization extinction ratio over the telecom C band wavelengths and robustness to fabrication variation, make it a good candidate for practical low loss micron scale silicon photonic integrated circuits.

# Chapter 3

# Silicon Electro-Optic Kerr Effect Modulator

Electro-optic modulators are key components for future optical interconnects and for optoelectronic integration. As has been described in the Introduction chapter, optical interconnects are vital in order to scale up with demands for rapid increase in data rates in today's data centers. In this regard, optical modulators are active devices where high modulation bandwidth, small device footprint, low loss and low energy per bit consumption are desired. Silicon photonics has the capabilities to meet these complex requirements. In this chapter, state of the art in silicon electro-optic modulators are described followed by design of a novel high speed electro-optic Kerr effect modulator [1].

## 3.1 State of the art

The most commonly used electro-optic effect to achieve modulation in silicon devices has been the plasma dispersion effect. This is because electric field effects based on electro-refraction such as the Pockels effect do not exist in silicon while the Kerr effect induces a small refractive index change of $\Delta n = 10^{-6}$, for an applied electric field of $10^7$ V/m [51] at 1.55 micrometer wavelength. Electric field effects in silicon, based on electro-absorption such as the Franz-Keldysh effect also induce a low refractive index change ($\Delta n = 1.5 \times 10^{-6}$ ,E=$10^7$ V/m) at 1.55 micrometers [51] to be useful. For device applications, a $\Delta n \sim 10^{-4}$ or greater is desired while avoiding the danger of an electrical breakdown of the medium. For intrinsic silicon at room temperature, the dielectric breakdown field is of the order of $3 \times 10^7$ V/m [52].

The plasma dispersion effect is based on a change in the free carrier concentration

[1] A version of the section 3.1 has been published in :D.V. Simili, M. Cada, "Silicon Kerr Electro-Optic Switch" in Proceedings of DCPHOTOPTICS, Scitepress pp. 74-79, 2015 and a version of sections 3.2-3.4 have been published in :

of silicon to induce a change in the absorption spectrum and therefore a change in the refractive index. The change in the refractive index of silicon was computed through experimentally obtained absorption spectrum in [51]. A refractive index change of the order of $10^{-3}$ was obtained for free carrier (electrons) concentration change of $10^{18}/cm^3$ at 1.55 micrometer wavelength. The different mechanisms used to achieve the plasma dispersion effect in the medium through which light is propagating are carrier accumulation, carrier injection and carrier depletion.

In the carrier injection technique, electrons and holes are injected into an intrinsic waveguide region. The structure used is a p-i-n junction diode. The injection of electrons and holes into the waveguide region is controlled by changing the voltage applied to the highly doped p and n regions of the structure. The charge transport mechanism is based on carrier diffusion. The switch off time for the device would depend on the electron-hole recombination lifetime for silicon which is 100 ns for n-type silicon at temperature of 300 K [34]. An example of a top performing modulator employing this technique uses a micro ring resonator structure to achieve speeds of 12.5 Gbps with a high extinction ratio greater than 9 dB at a modulation voltage of approximately 4 V [53].

In the carrier accumulation technique, mobile carriers are diffused into the intrinsic waveguide region. The concentration of mobile carriers in the waveguide region is controlled by adjusting the potential of the doped regions. The intrinsic waveguide region is split into two halves separated by an insulator region so the mobile carriers begin to accumulate on both sides of the insulator to form a capacitor structure. This type of structure would avoid the slow recombination process of the diffused mobile carriers. The first implementation of this technique reported a bandwidth in the neighborhood of 1-2 GHz with an extinction ratio greater than 16 dB and a device phase efficiency ($V_\pi L$) of approximately 8 V.cm [54]. Subsequent optimizations to this technique reported 10 GHz bandwidth with 3.8 dB extinction ratio and a better $V_\pi L$ of 3.3 V.cm [55].

In the carrier depletion technique, the silicon waveguide is a lightly doped p-n junction. The width of the depletion layer is controlled by reverse biasing the structure and therefore carrier concentration experienced by the propagating light in the waveguide is changed. This technique reported the highest bandwidth of 30 GHz,

Table 3.1: Comparison between demonstrated silicon plasma dispersion effect based modulators and the proposed silicon DC Kerr effect modulator.

| **Description** | **Modulation Bandwidth (GHz)** | **Modulation Speed (Gb/s)** | $V_\pi.L$ **(V.cm)** | **E/bit** | **Insertion Loss (dB)** | **Extinction Ratio (dB)** | **Footprint ($\mu m^2$ )** |
|---|---|---|---|---|---|---|---|
| Carrier Injection-MRR [[53]] | | 12.5 | | 4 fJ | | 9 | 78.5 |
| Carrier Accumulation-MZI [[54]] | 1 to 2 | 1 | 8 | | 6.7 | ∼16 | ∼1000 |
| Carrier Accumulation-MZI [[55]] | 10 | 10 | 3.3 | | 10 | 3.8 | ∼1000 |
| Carrier Injection-MRR [[60]] | 25 | 50 | 0.28 | | 5.2 | 4.58 | ∼75 |
| Carrier Depletion-MZI [[56]] | 30 | 40 | 4 | | 3.3 | 1.1 | ∼1000 |
| Carrier Depletion-MRR [[61]] | | 60 | 1.5-1.8 | | 1-2 | 4.2 | 380 |
| Carrier Depletion-MRR with PAM encoding [[58]] | 11 | 80 | | 7 fJ | ∼1 | | 201 |
| Proposed DC Kerr effect modulator-MRR | 45 | 90 | | 25 fJ | 3.5 | 6-17 | ∼1000 |

with an extinction ratio of 1.1 dB and a $V_\pi L$ of 4 V.cm [56]. The carrier transport mechanism in this case is carrier drift which is faster than the carrier diffusion used in previous techniques. Recent developments in modulators using the carrier depletion technique employ advanced modulation formats such as pulse amplitude modulation (PAM) to increase the data rate transmitted to 60 Gbps [57], 80 Gbps [58] and 112 Gbps [59] at the cost of energy efficiency and device complexity for short reach applications.

As shown in Table 3.1, the drawback of plasma dispersion effect is that the modulation speed is limited to 10's of Gbps without using advanced modulation formats due to carrier transport dynamics and faces a trade-off between modulation speed, extinction ratio, efficiency represented by energy per bit (E/bit) or $V_\pi.L$ and device footprint. In addition there are challenges in thermal stability due to the high thermo-optic coefficient of silicon [62].

An alternative option of using the ultrafast electro-optic or DC Kerr effect in silicon nanocrystals embedded in silica and a slot waveguide structure to potentially achieve high modulation speeds in the range of 100 GHz has been proposed [63, 64]. The DC Kerr effect is a bound electron effect and is inherently ultrafast with response times $\sim 10^{-16}$s [65] as it depends on the displacement of bound electrons to the applied electric field [63]. The advantage of silicon nanocrystals is that it has

shown at least two orders of magnitude greater optical Kerr coefficient than silica [1], and has been used to demonstrate an ultrafast all-optical Kerr effect switch [66]. The possibility of using the DC Kerr effect in silicon nanocrystals for modulation [67] along with experimental validation of the DC Kerr effect in silicon nanocrystals has been reported [68]. The advantage of using silicon nanocrystals in silica as the active medium is that the material is CMOS compatible in contrast to other electro-optic modulator designs [69, 70] where polymers are used as the active medium along with the Pockels effect. The performance metrics for the proposed DC Kerr effect modulator using a micro ring resonator structure (MRR) are summarized in Table 3.1. The proposed silicon DC Kerr effect modulator has the highest modulation speed of 90 Gbps using simple OOK modulation format as the device is not limited by the physical effect causing the refractive index change unlike silicon plasma dispersion effect modulators shown in Table 3.1. The proposed modulator also has a low energy/bit consumption of 25 fJ/bit with a useful predicted extinction ratio of 6-17 dB. As the silicon DC Kerr effect modulator is limited in modulation speed only by design of the modulator (for example RC effects and cavity photon lifetime in a MRR structure) and not by the actual physical effect causing refractive index change in waveguide, this type of design is well suited for next generation silicon electro-optic modulators targeting modulation speeds of ∼100 Gbps with energy/bit consumption of a few fJ/bit. In the following sections, a slot waveguide design using standard 220 nm silicon-on-insulator (SOI) platform that is suitable for the ultrafast electro-optic D.C Kerr effect modulator is described . The theoretical background is presented along with discussion on implementing the modulator using a slot waveguide ring resonator.

## 3.2 Background

Silicon nanocrystals embedded in silica with moderate silicon excess has a refractive index comparable to that of silica and therefore would provide weak optical mode confinement when used in a conventional strip waveguide with silica cladding configuration. An alternative structure is the slot waveguide [36] configuration where the light predominantly propagates in the low index medium in the narrow slot region. The geometry and electric field profiles for the horizontal configuration of the slot

waveguide with silicon nanocrystals in silica as the slot medium is shown in Figs. 3.1 and 3.2. One can observe that there is a significant portion of the optical mode in the slot region filled with silicon nanocrystals in silica. The parameters used in the mode simulation are in Table 3.2.

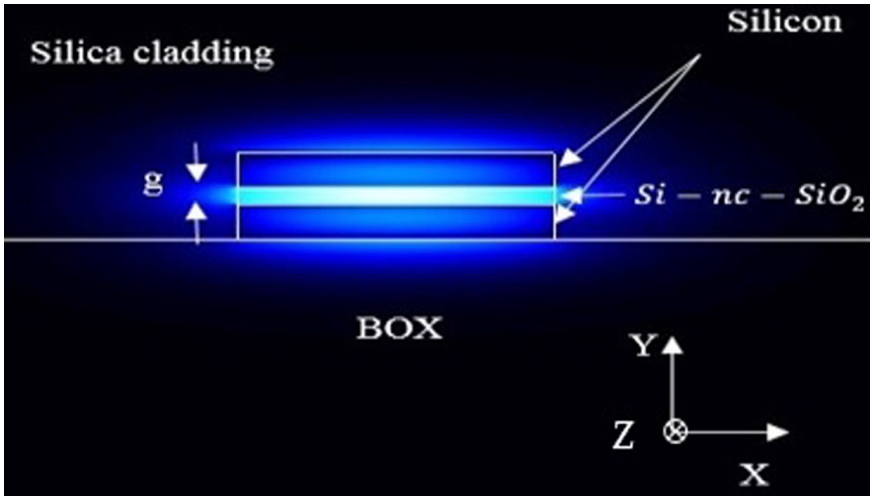


Figure 3.1: Cross section view of horizontal slot waveguide with color coded fundamental quasi-TM optical mode.

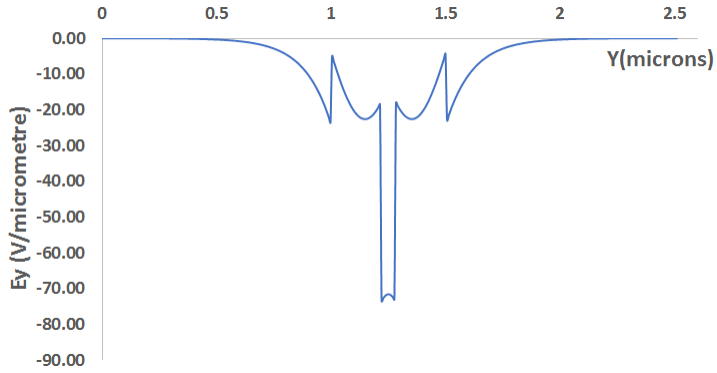


Figure 3.2: Vertical cross section electric field ($E_y$) of the fundamental TM mode along Y axis for the horizontal slot waveguide.

The fabrication of the horizontal or sandwich slot waveguide configuration with silicon nanocrystals in the slot region has been demonstrated with the deep-UV lithography techniques [71]. Here a thin layer of silicon nanocrystals embedded in silica is deposited over a crystalline silicon strip through LPCVD (Low Pressure Chemical Vapor Deposition) or PECVD (Plasma Enhanced Chemical Vapor Deposition) methods. This is followed by the deposition of an amorphous silicon layer on the silicon

nanocrystal slot region.

Table 3.2: Material parameters at 1.55 $\mu$m wavelength. [1]

| **Material Parameter** | **Value** |
|---|---|
| Silicon refractive index | 3.475 |
| Silica cladding refractive index | 1.444 |
| Silicon nanocrystals in silica refractive index | 1.7 |
| Silicon nanocrystals in silica third order nonlinear susceptibility ($m^2/V^2$) | $2 \times 10^{-18}$ |
| Two photon absorption coefficient (cm/GW) of silicon nanocrystals in silica | 70 |

The slot waveguide has been shown to be a suitable waveguide geometry for electro-optic applications as one can concentrate a significant portion of the optical mode across a narrow low index material gap and have electrically isolated silicon strip waveguides that serve as electrodes in close proximity for the vertical slot waveguide configuration [72]. The DC Kerr effect is a special case of the third order nonlinear time dependent perturbation where the electric field is static [73]. The ratio $(\frac{\delta n_{\text{eff}}}{\delta \epsilon})$ which represents shift in the modal effective index due to a differential amount of a uniform change in the relative dielectric constant in some part of the waveguide geometry is as described in [74],

$$(\frac{\delta n_{\text{eff}}}{\delta \epsilon}) = \frac{\iint |E|^2 dxdy}{2z_0 \iint Re(\vec{E} \times \vec{H}^*) \cdot \hat{e_z} dxdy} \tag{3.1}$$

Here, $\vec{E}$ is the electric field, $\vec{H}$ is the magnetic field of the optical mode and $\hat{e_z}$ is the unit vector along the direction of propagation (Z axis as shown in Fig. 3.1). The effect of the third order perturbation due to the DC Kerr effect is represented in the change in the relative dielectric constant of the medium($\Delta\epsilon$) . The material refractive index change due to D.C Kerr effect($\Delta n$) for a fully applied external electric field can be derived from [75] as,

$$\Delta n = \frac{3\chi^{(3)}}{2n} E_{\text{DC}}^2 \tag{3.2}$$

Here $n$ is the material refractive index,$(\chi^{(3)})$ is the material's third order nonlinear susceptibility and $E_{\text{DC}}$ is the applied DC electric field along the Y axis as shown in

Fig. 3.1. Considering the slot waveguide geometry where the applied voltage ($V$) can be dropped across the slot gap ($g$) of refractive index $n$, the DC electric field is $E_{\mathrm{DC}} = \frac{V}{g}$ . Taking $\Delta\epsilon = 2n\Delta n$ , the total shift in the modal index can be calculated from equations (3.1) and (3.2) as,

$$\delta n_{\mathrm{eff}} = \Gamma(\frac{3\chi^{(3)}}{2n})(\frac{V}{g})^2 \tag{3.3}$$

Here $\Gamma$ is the interaction factor [16],

$$\Gamma = \frac{\iint_{\mathrm{gap}} n|E|^2 dxdy}{z_0 \iint Re(\vec{E} \times \vec{H}^*) \cdot \hat{e_z} dxdy} \tag{3.4}$$

$\Gamma$ represents the ratio of the optical power in the transverse component ($|E_x|$ for TE mode and $|E_y|$ for TM mode) of the propagating mode that interacts with the material medium of refractive index $n$ in the slot gap and the applied DC electric field ($E_{\mathrm{DC}}$) to the total optical power. The expression in equation (3.4) is a simplification of the interaction factor definition [76] which is for a photonic crystal waveguide. The novelty in equation (3.3) is that it characterizes a waveguide in a DC Kerr effect based modulator as one can calculate the effective index change for a given applied voltage by taking into account the waveguide's interaction factor ($\Gamma$) as well as gap between the electrodes ($g$), both of which depend on the waveguide structure and electrode configuration, and the material's third order nonlinear susceptibility .

The effect of two photon absorption leading to slow free carrier effects would be negligible based on the material parameters of silicon nanocrystals [1]. There is an experimental proof that the horizontal slot waveguide with silicon nanocrystals as the slot medium has weaker free carrier effects compared to the conventional strip waveguide [77] and it has been shown that the ultrafast AC Kerr effect dominates over the response due to free carriers in the demonstration of the all-optical Kerr effect switch [66].

## 3.3 Results and Discussion

### 3.3.1 Slot waveguide optimization for the D.C Kerr effect

Based on the optimization results of silicon nanocrystal slot waveguides for nonlinear applications [78], the optimum slot waveguide dimensions for a horizontal slot waveguide with a silicon layer thickness (h) of 220 nm is, 60 nm slot gap (g) leading to a

device layer thickness of 500 nm and 200 nm slot arm width (w) for the fundamental TM mode at 1550 nm wavelength. The corresponding effective modal area is 0.05 $\mu m^2$ [78]. The horizontal slot waveguide is single mode for the optimum dimensions and the interaction factor for the slot waveguide is 0.36. The shift in effective index for the horizontal slot waveguide with respect to the applied voltage using the material parameters in Table 3.2 is shown in Fig. 3.3.

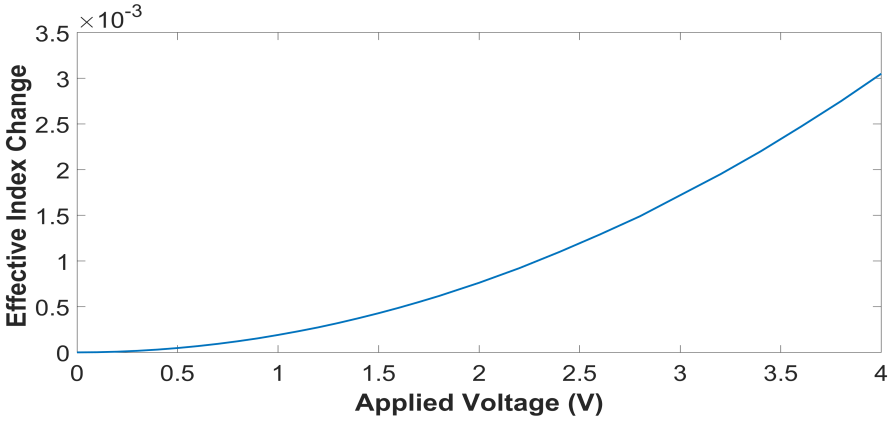


Figure 3.3: Effective index change versus voltage (V) for horizontal slot waveguide with 60 nm slot gap thickness.

A useful effective index change of the order of $10^{-4} - 10^{-3}$ is obtained in the voltage range of 0.8 V to 3 V for the considered slot waveguide. This corresponds to a phase efficiency of 0.63 V.cm for the silicon nanocrystal slot waveguide. These values are comparable with the effective index change and voltages obtained in silicon free carrier plasma dispersion effect-based modulators as reported in the review in [79] where the modulation speeds are at best in the range of 40-50 Gbps. Also, the typical electric breakdown field for silicon dioxide films is of the order of $10^8$ V/m, which implies a maximum of 6V for a 60-nm slot gap. Similar work of utilizing the D.C Kerr effect in an active medium embedded silicon slot waveguide has been presented in [80, 81, 82]. Here the active medium used is a nonlinear optical polymer. The theoretical background described in the previous section to calculate $\delta n_{\text{eff}}$ is verified experimentally in the determination of $\chi^{(3)}$ for the nonlinear optical polymer in [80] . A good agreement is obtained between experimentally obtained bulk $\chi^{(3)}$ for the polymer and it's $\chi^{(3)}$ determined in the silicon slot waveguide due to resonant wavelength shift caused by $\delta n_{\text{eff}}$ [80].

### 3.3.2 Resonator Structure Implementation

A schematic of a resonator structure along with electrodes to apply the required DC bias is shown in Fig. 3.4. A strip loaded section of thickness $t = 90$ nm is used to provide a connection between the coplanar electrodes and the n-doped silicon horizontal slot waveguide arms. This horizontal slot waveguide structure with electrical contacts can be fabricated by the technique of epitaxial lateral overgrowth [55]. Similar type of a resonator structure has been proposed for an electrically driven light emitting device [83]. The design of the resonator structure in this analysis is the double bus

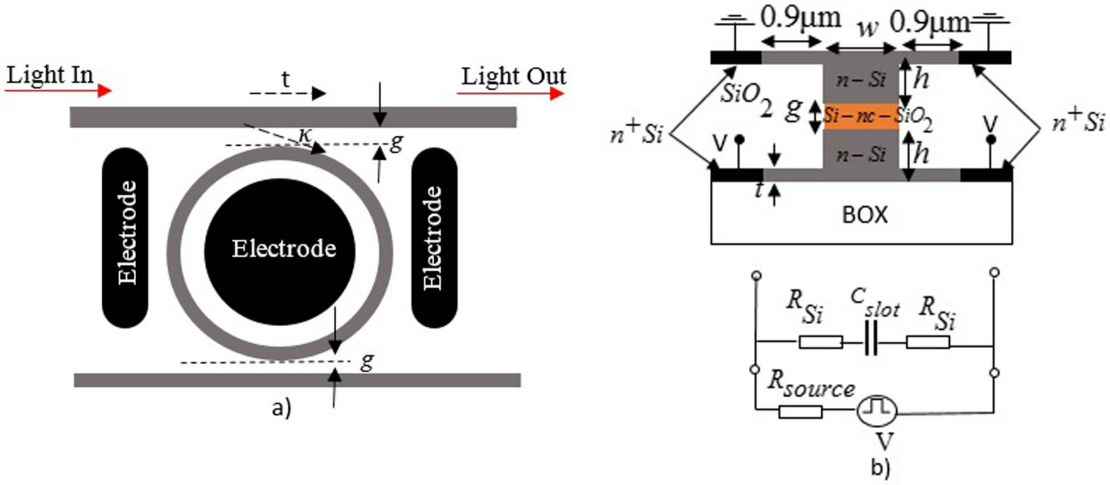


Figure 3.4: (a) Top view schematic of ring resonator structure for D.C Kerr effect device. (b) Schematic cross section view of horizontal strip-loaded slot waveguide in ring resonator along with lumped circuit model for ring resonator structure where $R_{\text{source}} = 50\ \Omega$ is the internal source resistance and $R_{\text{Si}}$ is the resistance of silicon stripload.

ring resonator as the second bus waveguide adds extra coupling loss compared to a single bus ring resonator and therefore allows for a variation in the ring waveguide propagation loss values to meet a target Q factor for the ring resonator. The ring waveguide diameter (D) is 40 $\mu$m. The device size is much smaller than the RF wavelength which is of the order of mm and therefore the device can be modeled as a lumped circuit with open termination as shown in Fig. 3.4(b) [84]. The RC limited bandwidth ($f_{3\text{ dB}}^{\text{RC}}$) for this case is due to the finite resistivity of doped silicon stripload and the slot gap capacitance. Using the slot waveguide dimensions, the capacitance

($C_{\text{slot}} = \epsilon_0 \epsilon_{\text{r(avg.)}} w\pi D)/g$) for the slot gap is 22.99 fF. Here $\epsilon_{\text{r(avg.)}}$ is the average relative permittivity which for silicon nanocrystals in silica is 6.2 which is dependant on the silicon excess percentage in Si-nc/SiO2 matrix and can be controlled in the fabrication process[1]. Using the finite element solver result of $\sim 2 \times 10^{-10}$ F/m for a 60 nm slot gap [85] with a dielectric having a refractive index of 1.7, a slightly greater capacitance of 25.13 fF is obtained. Using this capacitance value, the RC limited bandwidth is calculated to be $f_{3\text{ dB}}^{\text{RC}} \simeq 50$ GHz considering the resistivity of doped silicon ($n_{\text{D}} \approx 10^{17}/cm^3$) as 0.04 Ωcm.

In order to predict the performance of the microring resonator, the following design parameters are used: the radius (R) of 20 $\mu$m, the operation wavelength of 1.55 $\mu$m, the target total Q factor of 1935 which corresponds to a cavity photon lifetime limited bandwidth of 100 GHz, and a ring waveguide propagation loss of 30 dB/cm [86]. The steady state frequency domain transmission response of the resonator is shown in the Fig. 3.5.

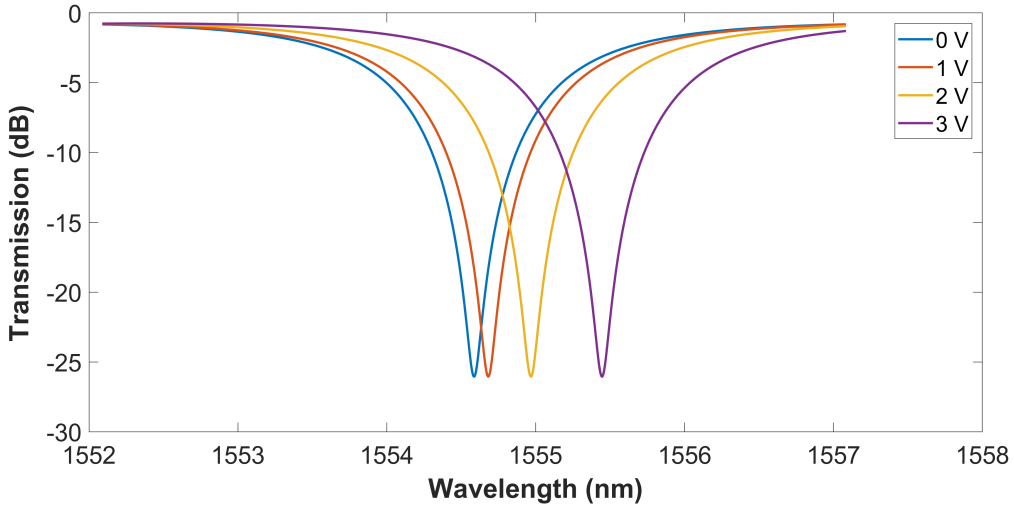


Figure 3.5: Through port transmission spectra plot for DC Kerr effect device with varying input voltages.

The resonant wavelength at 0V bias is 1554.58 nm. We can observe from the plot that a bias voltage of 3V results in a resonant wavelength shift of 0.86 nm which corresponds to a frequency detuning close to 100 GHz and the insertion loss at a wavelength of 1554.58 nm is close to 3 dB. The overall modulation bandwidth $f_{3\text{dB}} = (f_{\text{ph}} f_{\text{RC}})/\sqrt{(f_{\text{ph}}^2 + f_{\text{RC}}^2)}$ [33] taking the RC limited bandwidth ($f_{\text{RC}}$) of 49.74

GHz and the cavity lifetime limited bandwidth ($f_{\mathrm{ph}}$) of 100 GHz is calculated to be $\approx$ 45 GHz.

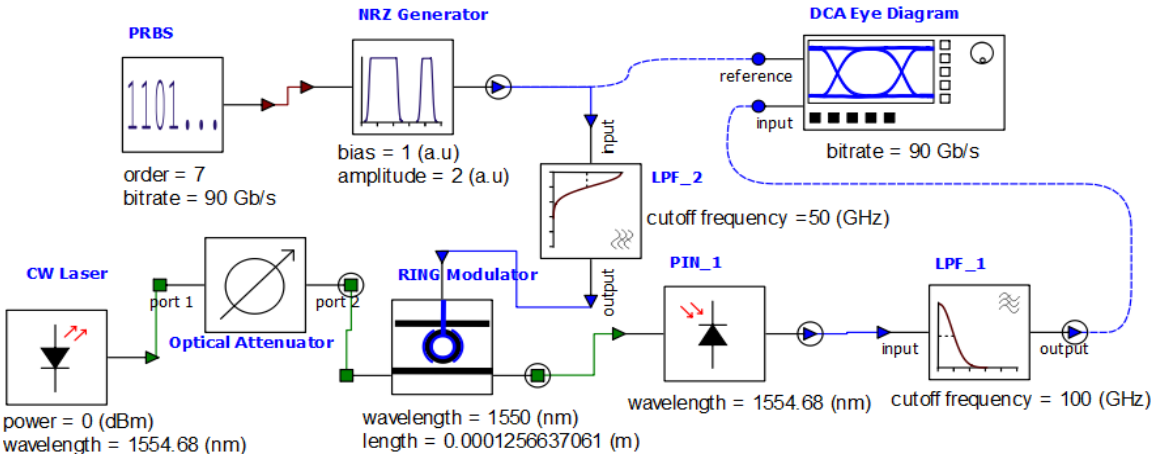


Figure 3.6: Circuit schematic to obtain time domain response of DC Kerr effect modulator.

Considering practical values for pseudo random bit sequence (PRBS) generator data rate and a 100 GHz Digital Communication Analyzer (DCA) oscilloscope, time domain simulation for the device was carried out using Lumerical INTERCONNECT software and the circuit schematic is shown in Fig. 3.6 . Taking the ring modulator's RC limited bandwidth of 50 GHz, and the resonant cavity quality factor of 1935, the simulated eye diagram without without photodiode noise using a non return to zero (NRZ) pseudo random bit sequence (PRBS) is shown in Fig. 3.6(a). The on-chip coupling loss to couple laser light in and out of the photonic integrated circuit with the ring modulator is taken as $\sim$ 15 dB which is practical considering input-output grating couplers [87] . The modulating signal is a NRZ 90 Gb/s PRBS7 with a d.c bias voltage of 1 V and a peak to peak amplitude ($V_{\mathrm{pp}}$) of 2 V. From Fig. 3.7 (a), we can observe a clear eye opening at 90 Gb/s with an extinction ratio $\sim$ 17 dB for the operating wavelength of 1554.68 nm. Considering the practical case of thermal noise and shot noise in the photodiode, we can observe noise and jitter in the eye diagram which cause partial closing of the eye as shown in Fig 3.7(b).An extinction ratio of 6.35 dB with a bit error rate (BER) of $6.25 \times 10^{-8}$ is obtained for this case.Here a Ge photodiode is considered which has a responsivity of 0.95 A/W and noise equivalent power of $4 \times 10^{-12}$ W/$\sqrt{Hz}$ at a wavelength of 1550 nm [88]. The average energy per bit consumption for NRZ modulation is ($C_{\mathrm{slot}} V_{\mathrm{pp}}^2/4$) [33], which for $V_{\mathrm{pp}}$ of 2 V is

25.13 fJ/bit.

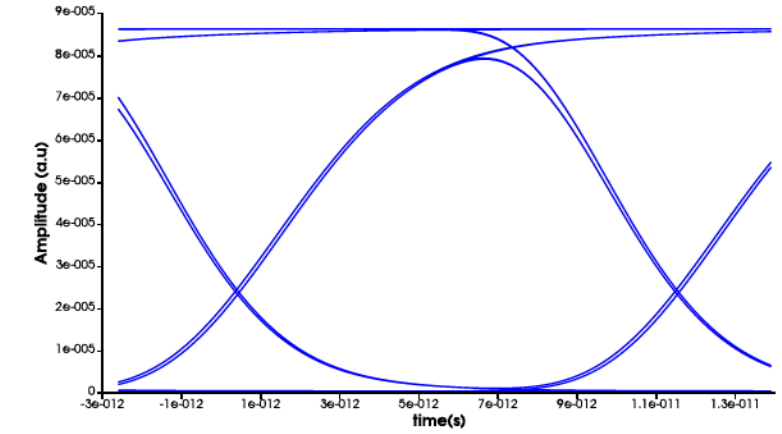


(a)

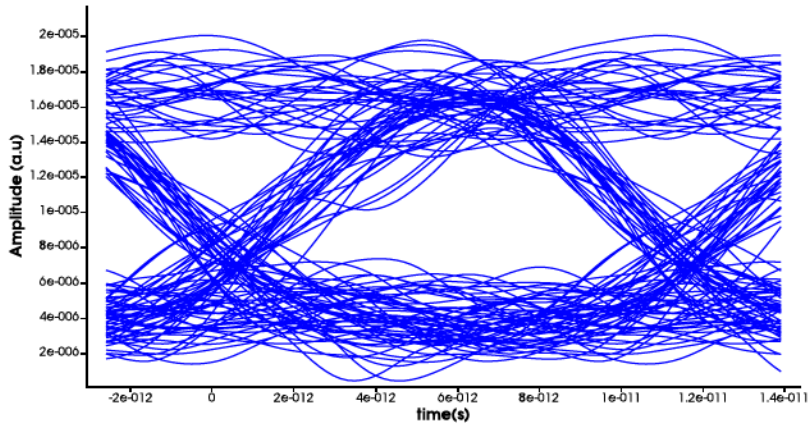


(b)

Figure 3.7: (a) Eye diagram at 90 Gb/s driven by PRBS7 NRZ signal with $V_{pp}$ of 2 V and a DC bias of 1 V. (b) Eye diagram taking a noise equivalent power of $4 \times 10^{-12}$ W/$\sqrt{Hz}$ in the photodiode.

In order to physically implement the ring resonator structure with a Q factor of 1935 that corresponds to a straight through coefficient ($t^2$) of 0.69, the required coupling gap between the bus waveguide and the ring waveguide is 510 nm. This is obtained through the 3D finite difference time domain (FDTD) simulation of the coupling section of the ring resonator at 1.55 $\mu m$ for varying coupling gaps as shown in Fig. 3.8.

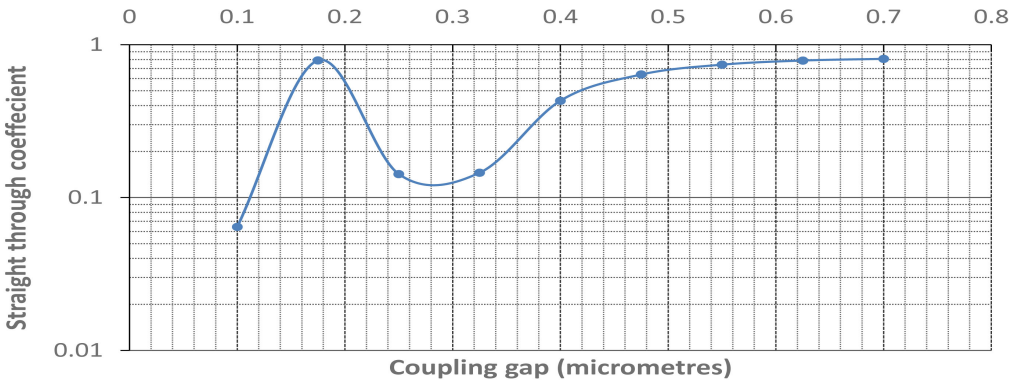


Figure 3.8: Straight through coefficient ($t^2$) versus coupling gap at 1.55 $\mu m$.

## 3.4 Conclusion

A CMOS compatible electro-optic modulator structure using the ultrafast DC Kerr effect and a slot waveguide with silicon nanocrystals in silica as the active material medium is proposed. The theoretical background to calculate the effective index shift using a slot waveguide is presented. A useful modulation efficiency of 0.63 V.cm is obtained. A compact ring resonator structure of 20 $\mu$m radius to implement the D.C Kerr effect modulator is described. The overall modulation bandwidth is 45 GHz, thereby allowing for 90 Gb/s data transmission rate with a useful extinction ratio ∼20 dB extinction ratio and an average energy per bit consumption of 25.13 fJ/bit. Such structures would be useful for wavelength division multiplexing (WDM) optical interconnect applications where large modulation speeds are desired at specific wavelength channels.

# Chapter 4

# Silicon Nanowire Mach Zehnder Interferometer Circuits and Slot Waveguide Bragg Gratings

## 4.1 Introduction

Silicon nanowire Mach Zehnder Interferometer(MZI) and Bragg grating (BG) structures are fundamental building blocks for silicon photonic integrated circuits. In this chapter design simulation , fabrication and experimental characterization of MZI and BG structures in slot waveguides are described.This chapter originated from the academic collaboration of NSERC SiEPIC (Silicon Electronic Photonic Integrated Circuits) program based at the University of British Columbia (UBC), Canada. Section 4.2 covers modeling and simulation of MZI circuits and slot waveguide BG's along with fabrication tolerance analysis and mask layout preparation for e-beam fabrication.The building blocks for the mask layout were obtained from the SiEPIC e-beam process design kit (PDK) library [89]. The fabrication of the silicon photonic chip was done through the ebeam multi project wafer fabrication process at Applied Nanotools, Inc., Edmonton, Canada which is described in section 4.4 and through University of Washington's (UW) Washington Nanofabrication Facility (WNF) described in section 4.8. Characterization of the devices in the multi project wafer silicon photonic chip was carried out using a custom built automated test setup [90] at UBC. Details about the characterization setup and subsequent measurement data analysis are described in section 4.5. Following this fabrication run, the slow light properties of slot waveguide BG's are further investigated and analyzed in sections 4.6-4.10. [1]

[1] A version of sections 4.2-4.5 is part of Deepak V. Simili, "Design, Fabrication and Experimental Data Analysis of Silicon Nanowire Mach Zehnder Interferometer Circuits and Slot Waveguide Bragg Grating Structures", UBC edX Phot1X course project report. A version of sections 4.6-4.6.6 is part of : D.V Simili, M. Cada, "Low loss slow light propagation in silicon slot waveguide" Optics Express, to be published.Manuscript accepted on 01 July 2019. A version of section 4.10 was submitted as D.V Simili, M. Cada,"Improved Coupling to Slow Light in Internally Corrugated Silicon Slot Waveguide Bragg Gratings" to IEEE Photonics Technology

## 4.2 Modeling and Simulation

### 4.2.1 Mach Zehnder Interferometer Circuit

The routing element to guide light in the photonic circuit is the nanowire waveguide or the strip waveguide.The nominal width for the strip waveguide is chosen as 500 nm, as a low propagation loss of 1.5 dB/cm is achieved using the 220 nm SOI fabrication process [19] for the fundamental TE polarization mode. Smaller waveguide widths (i.e. below 445 nm) would guarantee single mode operation but at the cost of higher propagation loss as the mode becomes more sensitive to scattering from the sidewall roughness. The mode simulation for the nominal strip waveguide from Lumerical MODE solutions software is shown in Fig. 4.1.

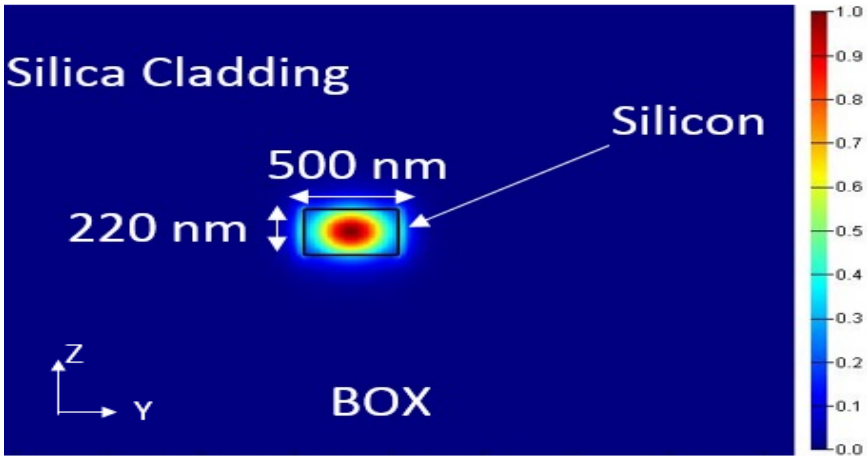


Figure 4.1: Cross section Intensity plot of the fundamental quasi-TE mode at a wavelength of 1.55 micrometers for the nominal 500x220 nm strip waveguide.

The variation in the effective index of the nominal strip waveguide over a span of 1.5-1.6 $\mu m$ is shown in Fig. 4.2.

The dispersion of the effective index can be represented in the form of a compact equation or a polynomial fit equation as shown below,

$$n_{eff}(\lambda) = n_1 + n_2(\lambda - \lambda_0) + n_3(\lambda - \lambda_0)^2 \tag{4.1}$$

Here $n_1, n_2, n_3$ are the polynomial fit coefficients,$\lambda$ is the wavelength in micrometers and $\lambda_0$ is the nominal wavelength of 1.55 micrometers. The polynomial expression for the nominal 500x200 nm strip waveguide is given by the equation (4.2).

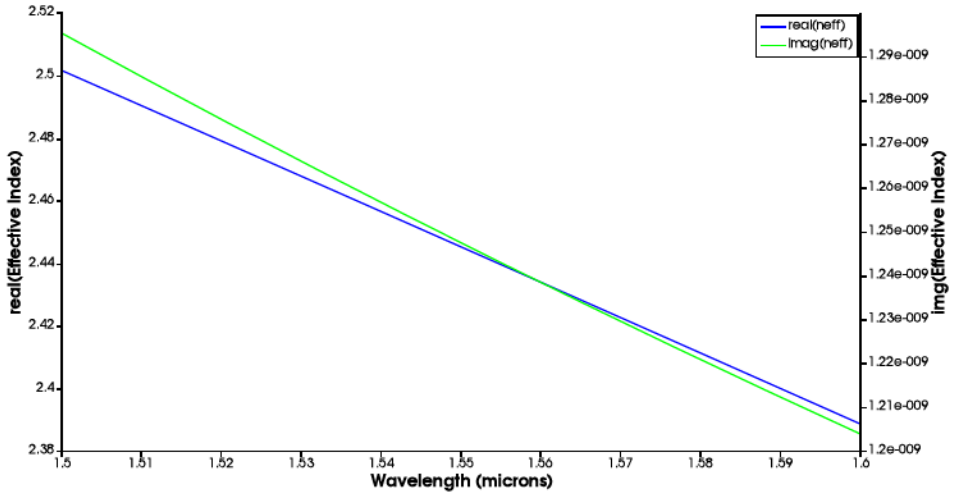


Figure 4.2: Effective index versus the wavelength for the strip waveguide shown in Fig. 4.1.

$$n_{eff}(\lambda) = 2.44531 - 1.12947(\lambda - \lambda_0) - 0.0421(\lambda - \lambda_0)^2 \tag{4.2}$$

For the nominal strip waveguide, the bend loss in the fundamental quasi-TE mode for a 10 $\mu m$ bend radius is 0.0039 dB, which is less than 0.1% optical loss in the bend. For a 5 $\mu m$ bend radius, the bend loss is 0.0157 dB which is less than 0.2% optical loss.

The plot of the group index versus wavelength for the nominal strip waveguide is shown in Fig. 4.3. The group index of the waveguide is an important parameter as it determines the free spectral range of the MZI. In order to get the circuit level performance of the MZI, one needs to consider the effect of the input/output grating couplers and Y branches required to implement the MZI circuit. The circuit level simulation was carried out using Lumerical INTERCONNECT software. The INTERCONNECT simulation software takes into account the s-parameters of the grating couplers and Y branches in the photonic circuit to give a more realistic transmission spectra for the MZI device.Shown in Fig. 4.4 is the INTERCONNECT simulation for an MZI circuit with a path length difference of 30 $\mu$m.

The table of design variants for the MZI with varying path length differences is shown in Table 4.1. Also shown are the calculated free spectral ranges from the simulated group index for the nominal waveguide at 1550 nm.

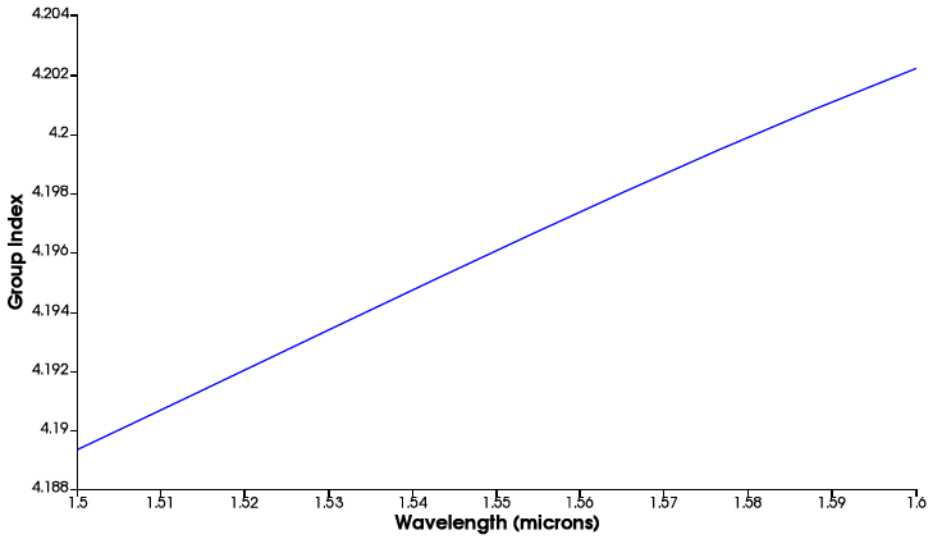


Figure 4.3: Group index versus the wavelength for the strip waveguide.

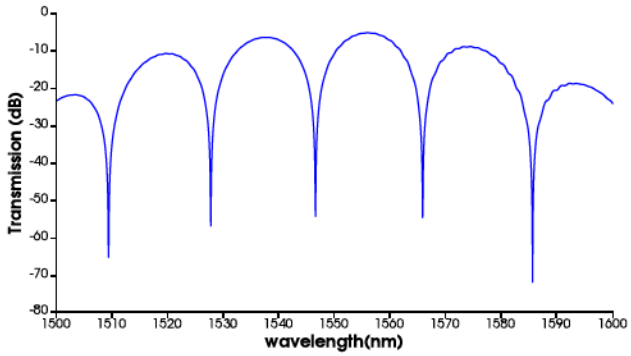


Figure 4.4: Circuit level simulation for an MZI circuit with a path length difference of 30 $\mu$m.

The MZI design variants are converted into a .gds file using the open source Klayout software tool.The .gds file is then used by the e-beam fabrication process to transfer the pattern of the .gds file onto the silicon layer of the SOI (Silicon-on-Insulator) wafer.The design area allowed for a single .gds file is 605x410 $\mu m$. Fig. 4.5(a) shows the MZI circuit drawn on the Klayout tool using the built-in optimized TE mode input/output grating couplers and Y branches and a path length difference of 29.91 $\mu m$. In order to analyze the effect of manufacturing variability on the MZI circuits, a corner analysis is performed. The corner analysis involves calculation of the waveguide properties such as effective index and group index considering the fabrication variability of the waveguide dimensions.

Table 4.1: Design variants for the MZI circuits with calculated FSR for the nominal waveguide group index at 1550 nm

| **w(nm)** | **Polarization** | **$\Delta L(\mu m)$** | **FSR (nm)** | **Group Index** |
|---|---|---|---|---|
| 500 | TE | 30 | 19.08563711 | 4.196 |
| | | 120 | 4.771409279 | |
| | | 150 | 3.817127423 | |
| | | 180 | 3.180939519 | |

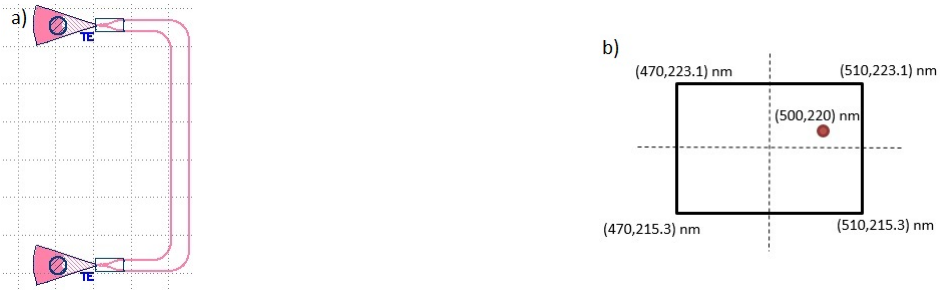


Figure 4.5: (a)MZI circuit drawn on Klayout with a path length difference of 29.91 $\mu m$. (b) Corner analysis points with nominal design point.

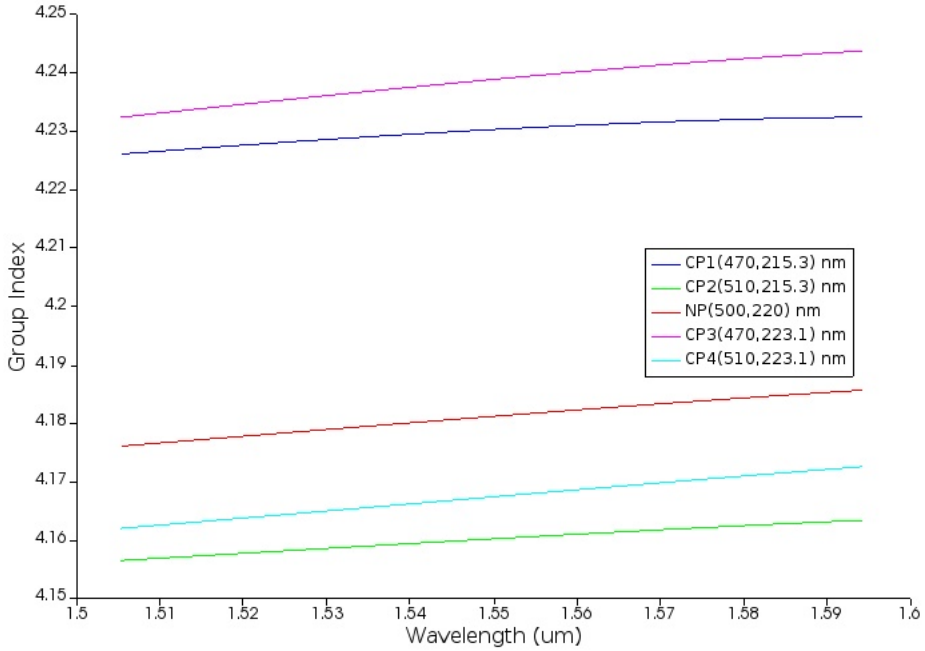


Figure 4.6: Corner analysis dispersion plot of the waveguide group index

Figure 4.5(b) shows the corner analysis points for the strip waveguide dimensions

for the fabrication process used. Also shown is the nominal point with waveguide dimensions of 500x220 nm. Calculating the group indices for the four corner points and the nominal point, one can obtain the range of group indices that the actual fabricated waveguide would have. From Fig. 4.6, the expected group index range is between 4.16 - 4.24 at a wavelength of 1550 nm.

### 4.2.2 Slot waveguide Bragg grating structures

The fundamental unit in a slot waveguide Bragg grating structure is the slot waveguide. In order for the mode in the nanowire strip waveguide to transition to the slot waveguide mode, a strip waveguide to slot waveguide mode converter is required.This is implemented using the low loss design in [6]. Here the 500 nm wide strip waveguide tapers to a slot waveguide with 200 nm arm width and 100 nm slot gap.

| $W_{slot}(nm)$ | $W_{arm}(nm)$ | $n_{eff}$ | $\Lambda(nm)$ | $\Delta W_{in}(nm)$ |
|---|---|---|---|---|
| 100 | 200 | 1.66 | 466 | 10,20,30 |

Table 4.2: Design variants for the uniform slot waveguide Bragg grating

The design variants for the uniform slot waveguide Bragg grating structures are shown in the Table 4.2.The 3D FDTD unit cell simulation result of the uniform grating structure to calculate the stopband bandwidth (nm) and coupling coefficient ($\kappa(m^{-}1)$) is shown in the Figs 4.7(a) and 4.7(b).

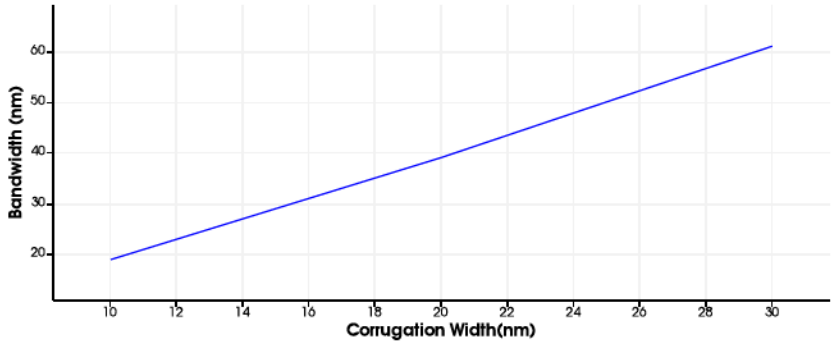


(a)

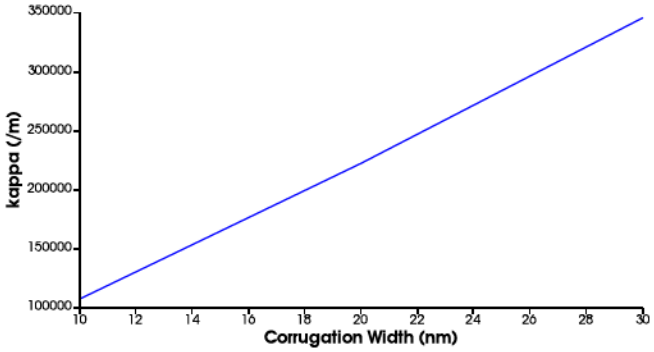


(b)

Figure 4.7: (a) Stopband bandwidth of the Uniform Bragg grating structure versus the internal corrugation width. (b) Coupling coefficient $\kappa(m^{-}1)$ versus the corrugation width.

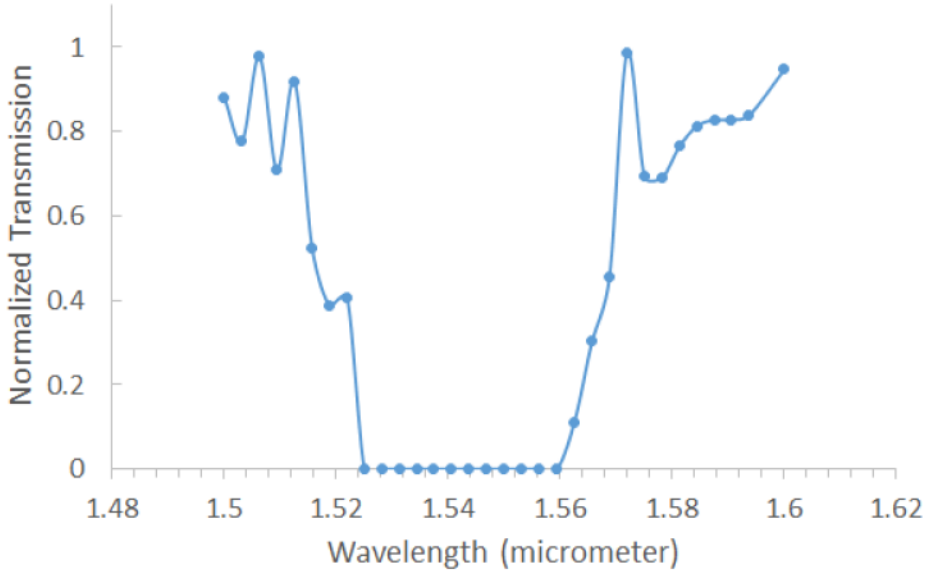


Figure 4.8: 3D FDM simulation result of normalized transmission spectrum for the uniform Slot Bragg grating structures with $\Delta W_{in} = 20$ nm .

The number of grating periods considered in the uniform Bragg grating structures is 650. The 3D Finite Difference Method (FDM) simulation result for the transmission spectra of a uniform slot Bragg grating structure is shown in Fig. 4.8. As predicted by the 3D FDTD unit cell analysis, the stopband bandwidth for slot Bragg grating with $\Delta W_{in} = 20$ nm is $\sim 40$ nm. In order to understand the effect of manufacturing variability on the central Bragg wavelength, a corner analysis for the slot waveguide is carried out. From the corner analysis slot waveguide dimensions shown in Fig. 4.9(a), a minimum effective index of 1.611 and maximum effective index of 1.7215 was obtained at a wavelength of 1550 nm. This corresponds to a minimum Bragg wavelength of 1501.5 nm and a maximum Bragg wavelength of 1604.4 nm for the designed grating period of 466 nm.The photonic circuit drawn on the mask layout to characterize the slot waveguide Bragg grating structures is shown in Fig. 4.9(b).

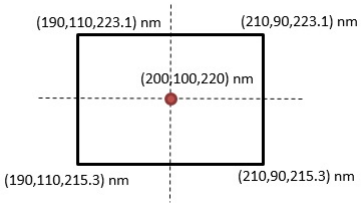


(a)

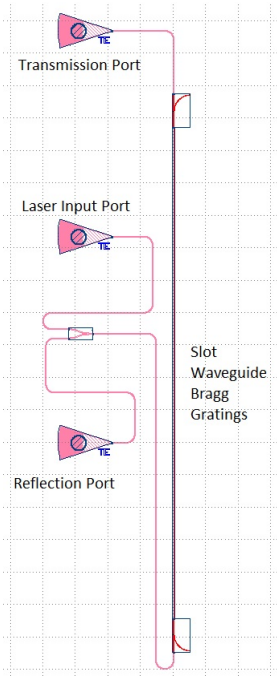


(b)

Figure 4.9: (a) Slot waveguide dimension variation for the corner analysis.The nominal point at the center corresponds to nominal slot waveguide dimensions of 200 nm arm width, 100 nm slot gap width and 220 nm device layer thickness. (b) Klayout implementation of the slot waveguide grating structure.

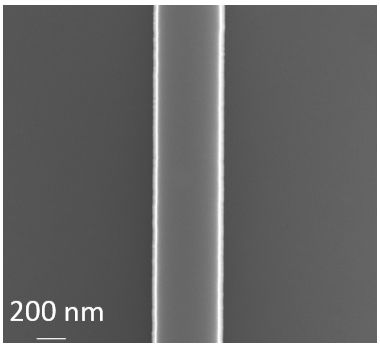


Figure 4.10: Top view SEM image of the fabricated 500x220 nm silicon strip waveguide

## 4.3 Fabrication

The photonic devices were fabricated using the NanoSOI MPW (Multi Project Wafer) fabrication process by Cameron Horvath at Applied Nanotools Inc. Edmonton, Canada [19] which is based on direct-write 100 keV electron beam lithography technology. Silicon-on-insulator wafers of 200 mm diameter, 220 nm device thickness and 2 $\mu m$ buffer oxide thickness are used as the base material for the fabrication. The wafer was pre- diced into square substrates with dimensions of 25x25 mm, and lines were scribed into the substrate backsides to facilitate easy separation into smaller chips once fabrication was complete. After an initial wafer clean using piranha solution (3:1 H2SO4:H2O2) for 15 minutes and water/IPA rinse, hydrogen silsesquioxane (HSQ) resist was spin-coated onto the substrate and heated to evaporate the solvent. The photonic devices were patterned using a Raith EBPG 5000+ electron beam instrument using a raster step size of 5 nm. The exposure dosage of the design was corrected for proximity effects that result from the backscatter of electrons from exposure of nearby features. Shape writing order was optimized for efficient patterning and minimal beam drift. After the e-beam exposure and subsequent development with a tetramethylammonium sulfate (TMAH) solution, the devices were inspected optically for residues and/or defects. The chips were then mounted on a 4 inch handle wafer and underwent an anisotropic ICP-RIE etch process using chlorine after qualification of the etch rate. The resist was removed from the surface of the devices using a 10:1 buffer oxide wet etch, and the devices were inspected using a scanning

electron microscope (SEM) to verify patterning and etch quality. A 2.2 micrometer oxide cladding was deposited using a plasma-enhanced chemical vapor deposition (PECVD) process based on tetraethyl orthosilicate (TEOS) at $300^0$ C. Reflectrometry measurements were performed throughout the process to verify the device layer, buffer oxide and cladding thicknesses before delivery. SEM image of the fabricated strip waveguide is shown in Fig. 4.10.

## 4.4 Experimental Data Analysis

### 4.4.1 MZI Circuits

The characterization of the devices were carried using a custom-built automated test setup [90] with the automated control software written in Python [91]. The input source is an Agilent 86100B tunable laser and the output detectors are Agilent 81635A optical power sensors. The measured wavelength range is 1520-1580 nm in 10pm steps and the measurement temperature is $20^0C$. A polarization maintaining fiber is used to couple TE polarized light from the input laser to the grating couplers [87]. Coupling light into and out of the chip was achieved using a polarization maintaining fibre array [92].

The input power of the laser source is set to 1 mW or 0 dBm.The input and output grating couplers have a wavelength dependent transmission as shown in Fig. 4.11. In order to overcome this characteristic of the grating couplers and compare the experimental device results to the analytical simulation results, a baseline correction is performed. The free spectral range of the MZI and the waveguide group index can then be extracted out using an MZI model fit with the autocorrelation technique [30]. We can observe from Fig. 4.12 that the free spectral range of measurement data, MZI model fit data and the INTERCONNECT circuit simulation are quite close. There is discrepancy in the device loss between the measurement data and INTERCONNECT circuit simulation data which is most likely due to inaccurate s-parameters for the grating couplers in the INTERCONNECT simulation model.

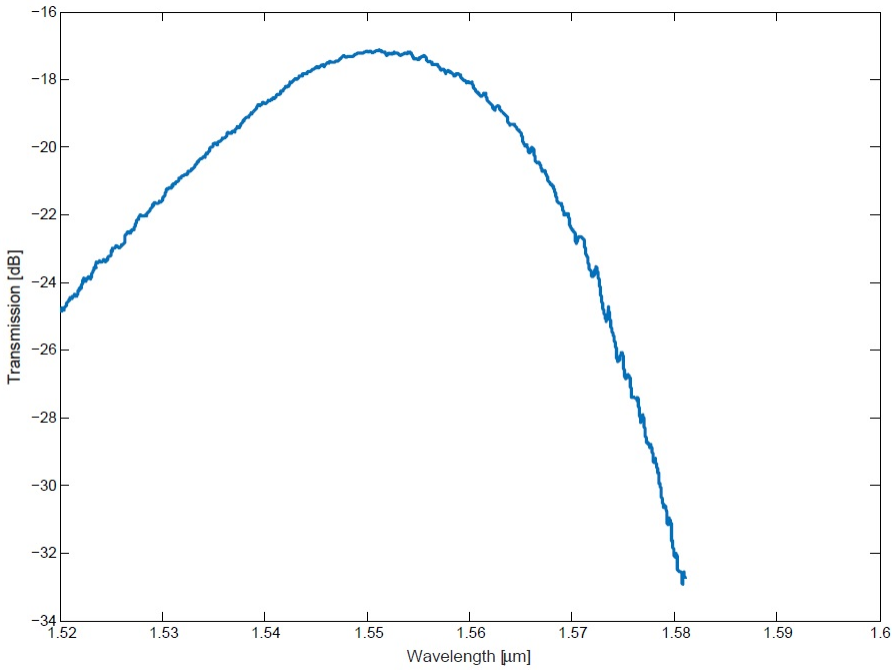


Figure 4.11: Input and output grating coupler experimental data

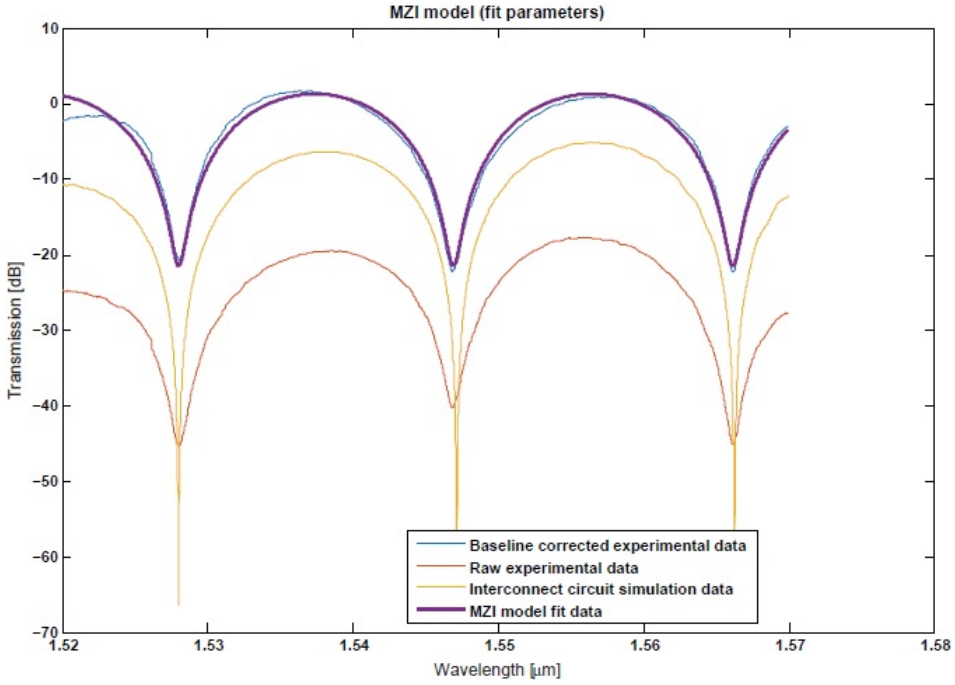


Figure 4.12: Experimental data plot for the MZI with a path length difference of 29.91 $\mu m$ along with MZI model fit data and Interconnect circuit simulation data

The experimentally obtained free spectral range and the waveguide group index

for the MZI design variants is summarized in the Table 4.3.

| w(nm) | Polarization | $\Delta L(\mu m)$ Layout | FSR (nm) | $n_g$ | $n_g$(%difference) |
|---|---|---|---|---|---|
| 500 | TE | 29.9119 | 19.16926111 | 4.19 | 0.142993327 |
| | | 119.993 | 4.772825097 | 4.195 | 0.023832221 |
| | | 149.9906 | 3.820097887 | 4.193 | 0.071496663 |
| | | 180.0006 | 3.184723868 | 4.191 | 0.119161106 |

Table 4.3: Experimentally obtained Free spectral range and waveguide group indices at a wavelength of 1550 nm

The extracted group index from the experimental data for the MZI design variants is within 0.15 % of the simulated group index and lies within the corner analysis range of 4.16- 4.24 .

### 4.4.2 Slot waveguide Bragg grating structures

The raw spectrum for the uniform Bragg grating with 10 nm internal corrugation width is shown in Fig. 4.13. The extinction ratio for the stopband is in excess of 30 dB. The center wavelength is in between 1535-1540 nm. Fig. 4.14 shows the

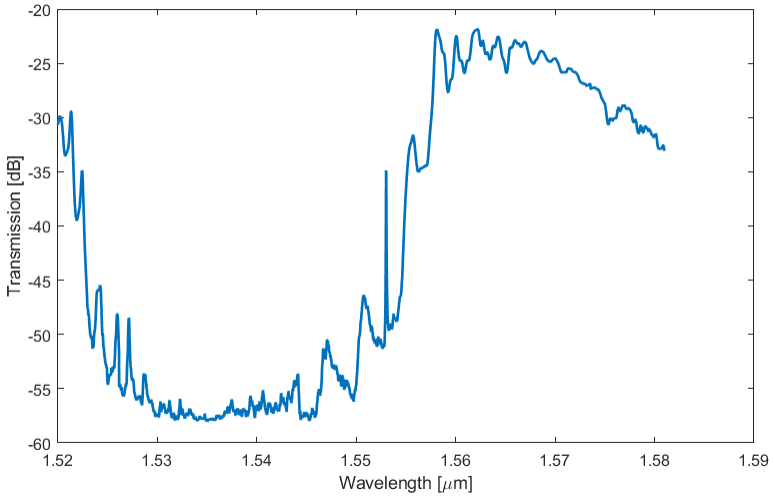


Figure 4.13: Measured raw spectra for the uniform slot waveguide Bragg grating with $\Delta W_{in} = 10nm$

measured transmission spectra for the uniform Bragg gratings with $\Delta W_{in}$ = 10 nm

and $\Delta W_{in}$ = 20 nm. Here the spectra has been normalized by using a straight waveguide as a reference and subtracting the transmission of the straight waveguide reference to the raw data transmission from the uniform Bragg gratings. From Fig. 4.14, we can observe that the extinction ratio of the stop bands is between 30-35 dB . As the corrugation width is increased the width of the stopband becomes wider due to increase in the grating coupling coefficient as predicted in the simulation. The measurement bandwidths are approximately of 20 nm for $\Delta W_{in} = 10$ nm and 40 nm for $\Delta W_{in}$ = 20 nm which are in agreement with simulation results in Figs. 4.7(a) and 4.8. The measurement central wavelength for the Bragg gratings lies within the corner analysis range of 1501.5 - 1604.4 nm.

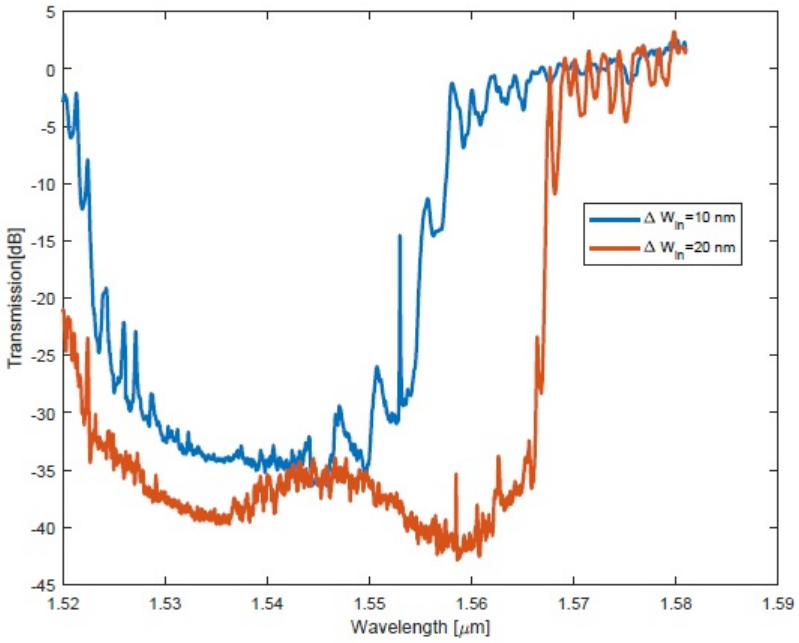


Figure 4.14: Measured transmission spectra for the uniform slot waveguide Bragg grating with $\Delta W_{in} = 10nm$ and $\Delta W_{in} = 20nm$

In summary, an average waveguide group index of 4.192 for a 500 nm strip waveguide at 1550 nm wavelength was experimentally obtained using the fabricated MZI circuits. This is in excellent correlation with simulated waveguide group index of 4.196 and within the corner analysis range of 4.16-4.24. The slot waveguide uniform Bragg gratings showed high extinction ratios in the range of 30-35 dB and bandwidths in the range of 20-40 nm were experimentally obtained. The central Bragg wavelength for the slot waveguide uniform Bragg gratings is almost 1540 nm which is within the

corner analysis range of 1501.4-1604.4 nm.

Using the experimentally obtained group index for the strip waveguide and stopband properties of the slot waveguide Bragg gratings, slow light properties of slot waveguide Bragg grating are determined as described in the following sections.

## 4.5 Slow Light Property of Slot Waveguide Bragg Gratings

Silicon slot waveguides [36] are a key component in active and passive photonic devices to enable development of silicon-based photonic integrated circuits (PIC). It has been used to provide ultra compact, broadband polarization handling for application to large scale PIC's [93], high performance electro-optic modulators [94, 69, 95, 96] as well as biosensor applications [25, 6]. Silicon slot waveguide with Bragg gratings [97] offers the possibility of combining advantages in a slot waveguide with functionality of a Bragg grating (BG). Specifically, they are one-dimensional (1D) periodic structures wherein light is confined in the low index slot medium thereby allowing for utilization of optical properties of the low index slot medium and it possesses a stopband which is characteristic of a photonic crystal (PC) structure. Slot waveguide BG structures have been demonstrated for its sensing and resonator based capabilities [97] and has been theoretically investigated for its slow light effects [98]. Enhancement of the in-device electro-optic coefficient (effective $r_{33}$) of a silicon-organic hybrid electro-optic modulator using slow light effect has been demonstrated in a 1D PC slot waveguide using external corrugations [99]. Although slow light using two-dimensional (2D) PC slot waveguides has been used to greatly enhance the effective $r_{33}$ [100, 101], it suffers from higher propagation loss due to scattering from the 2D PC holes and lower fabrication tolerance due to a more complex arrangement of PC holes as in the case of dispersion engineered PC slot waveguides [100] . It has been reported that the propagation loss for a 2D PC slot waveguide is sensitive to roughness in the hole surface and slot width [102]. The advantage of 1D PC slot waveguides considered in this work over 2D PC slot waveguides is that it has lower fabrication complexity and potential for lower propagation loss [99].

## 4.6 Modeling and simulation

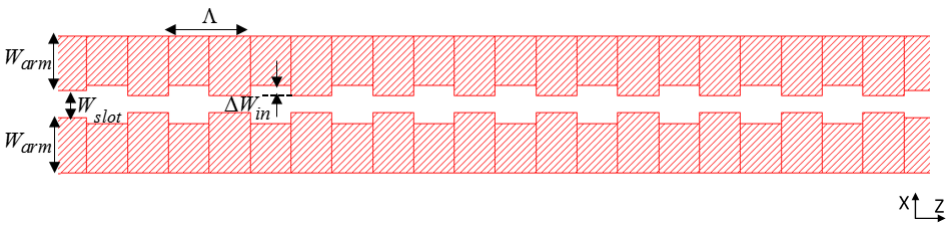


Figure 4.15: kLayout screen capture of silicon slot waveguide BG sections with Internal corrugations.

The fundamental unit in a slot waveguide BG structure is the slot waveguide which has an arm width ($W_{arm}$) and a slot gap ($W_{slot}$) as shown in Fig. 4.15. The geometry of a uniform slot waveguide BG structure with internal corrugations is shown in Fig. 4.15 where $\Lambda$ is the Bragg period, $\Delta W_{in}$ is the internal corrugation width.

The theoretical photonic band structure of the fundamental quasi TE mode for a unit cell of the internally corrugated slot waveguide BG with $\Delta W_{in} = 20\ nm$ is shown in Fig. 4.16(a). We can observe flattening of the mode close to the band edge indicating slow propagating light. The optical mode is strongly confined in the low index slot medium with a confinement factor ($\sigma$) of 0.36 as shown in Fig. 4.16(b).

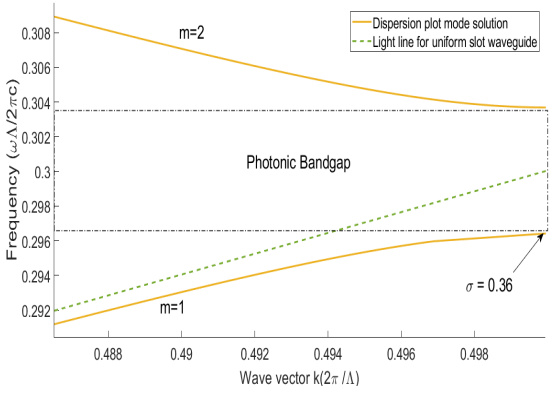


(a)

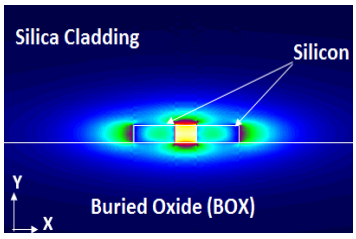


(b)

Figure 4.16: (a) Photonic band structure for internal corrugated slot waveguide with $\Delta W_{in} = 20\ nm$. (b) TE mode profile at the band edge for the fundamental mode band (m=1), where the optical mode confinement factor ($\sigma$) is 0.36 in the slot region.

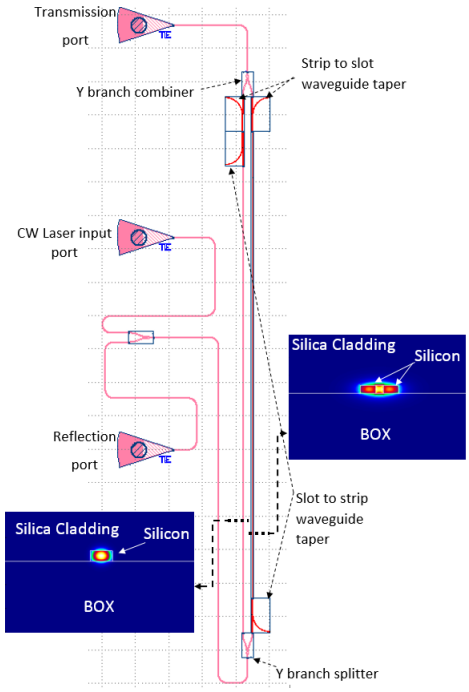


(a)

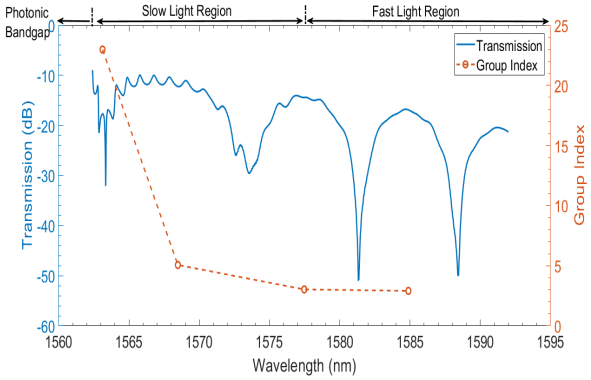


(b)

Figure 4.17: (a) kLayout screen capture of MZI circuit along with strip waveguide and slot waveguide cross sections in two arms with fundamental quasi-TE mode intensity plots. (b) Simulated transmission spectrum for $\Delta W_{in} = 20$ nm along with calculated group index.

### 4.6.1 Photonic circuit simulation

Mask layout screen capture of the MZI photonic circuit with a slot waveguide BG section in one of the arms is shown in Fig. 4.17(a). The two MZI arms have the same length with difference being one arm has a slot waveguide BG section and the other arm has a strip waveguide section. Both the arms have strip to slot waveguide tapers to cancel the effect of each other. Thus, the resulting transmission spectrum from the MZI would be a combination of the strip waveguide properties and the slot waveguide BG section. With group index of the strip waveguide experimentally determined to be 4.19 in the wavelength region of 1.52-1.58 $\mu$m, group index of the slot waveguide BG section can be extracted out in this wavelength region.

In order to get a realistic simulation , the circuit in Fig. 4.17(a) is simulated using Lumerical INTERCONNECT which is a commercial photonic circuit simulation software tool. Photonic circuit simulation is an important step in the design flow of

photonic integrated circuits (PIC) as one can optimize an individual component by performing several iterations and variations and then integrate the component in the circuit so that it performs as intended [103].

The slot waveguide arm width is chosen as 200 nm , with a slot gap of 100 nm. The Bragg period is 460 nm so that the stopband edge is within 1.5-1.6 $\mu$m.The number of grating periods considered is 600 which gives the length of the BG section as 276 $\mu$m.

The photonic circuit simulation uses a combination of Process Design Kit (PDK) library [89] building block elements that are calibrated based on foundry fabrication process experimental results and custom components whose S parameters are obtained through simulation using computer-aided design (CAD) tools. Specifically, the strip to slot waveguide tapers were modeled using 3D FDTD technique and slot waveguide Bragg gratings were modeled using Rigorous Coupled Mode Theory (RCMT). The frequency domain simulation is based on scattering data analysis which is obtained through the physical device or component modeling. Building block elements from the PDK library [89] are Y branch, Input/output grating couplers and the strip waveguide. Custom components used are strip to slot waveguide mode tapers and slot waveguide Bragg gratings.

Simulated transmission spectrum of the photonic circuit is shown in Fig. 4.17(b). From the transmission spectrum we can observe a variation in the fringe minima. This is because of increase in group index of the slot waveguide BG arm as one approaches with wavelengths close to the photonic bandgap.The group index can be extracted from the transmission spectrum using the relation [104],

$$n_g(\lambda) = \pm \frac{\lambda^2}{[FSR(\lambda)]L} + n_{g(ref.)} \tag{4.3}$$

Here $n_g(\lambda)$ is the group index of the slot waveguide BG section at a wavelength $\lambda$ , $FSR(\lambda)$ is the corresponding free spectral range in the MZI transmission spectrum, $L$ is the length of the slot waveguide BG section and $n_{g(ref)}$ is the group index of the reference arm strip waveguide which is experimentally determined to be 4.19 in the considered wavelength range. In the fast light region shown in Fig. 4.17(b), the group index of the slot waveguide arm is smaller than that of the strip waveguide indicating a shorter optical path length than the strip waveguide arm. As one approaches the

slow light region, the group index of slot BG waveguide increases and becomes equal to that of the strip waveguide resulting in broadening of the fringe compared to the fast light region. In the slow light region, the group index of slot BG waveguide is now greater than that of the strip waveguide resulting in greater optical path length in the slot BG waveguide arm. The plus symbol is applied in (4.3) when calculating group index in the slow light region and minus symbol is applied in the fast light region [104]. A peak group index of 22.98 is obtained in the slow light region as shown in Fig. 4.17(b).

We can observe Fabry-Perot type oscillations due to group index mismatch in the slow light region. This contributes to coupling losses in the slot BG waveguide arm at the slow light wavelength region. Insertion loss for the for the slot waveguide Bragg gratings which includes coupling loss and propagation loss can be estimated from difference in contrast ratios of MZI transmission spectrum fringes in the slow and fast light regimes [104] wherein the positive and negative symbols are used in Eq. (4.4) respectively.

$$IL(\lambda) = C_p(\lambda) + \alpha_{sw}(\lambda)L \approx \alpha_{fw}L + E_{mean} \pm E(\lambda) \tag{4.4}$$

where ,

$$E(\lambda) = 20log_{10}(\frac{E_{max}(\lambda) + E_{min}(\lambda)}{E_{max}(\lambda) - E_{min}(\lambda)}) \tag{4.5}$$

Here $E_{max}(\lambda)$ and $E_{min}(\lambda)$ are maximum and minimum electric fields at the MZI output. $E_{mean}$ is mean value of $E(\lambda)$ in the fast light region, $\alpha_{fw}$ is propagation loss in the fast light region, approximated as 10 dB/cm which is comparable to that of a slot waveguide and $L$ is the length of the slot waveguide BG section which is 276 $\mu$m. Taking the ratio to calculate $E(\lambda)$ filters out the effect of the input output grating couplers, 3 dB splitter and combiner and strip to slot mode converters as they are identical for both the MZI arms. This leaves only coupling loss $C_p(\lambda)$ to the slow light mode and propagation loss of slow light ($\alpha_{sw}$) [104]. Using this technique for the simulated transmission spectrum shown in Fig. 4.20(b), a phase shifter insertion loss of 4.39 dB at a wavelength of 1563 nm with an extinction ratio of $\sim$ 14 dB is obtained in the slow light region.

### 4.6.2 Fabrication tolerance analysis

In order to understand the effect of manufacturing variability on the central Bragg wavelength, a slot arm width of +/−10 nm from the design dimension of 200 nm and a SOI thickness variation of +3.1 to −4.7 nm from the nominal thickness of 220 nm is considered in the analysis. The corresponding slot waveguides had a minimum effective index of 1.611 and maximum effective index of 1.7215 at a wavelength of 1550 nm . This corresponds to a minimum Bragg wavelength of 1482.1 nm and a maximum Bragg wavelength of 1583.7 nm for the designed grating period of 460 nm. This shift in Bragg wavelength from design target due to manufacturing variability can be overcome by having design variants with varying Bragg periods and through thermal tuning. By introducing air trenches through under etching around the MZI arms , thereby providing better thermal isolation, a tuning efficiency of 0.49 mW/FSR has been demonstrated [105]. This corresponds to 0.98-4.9 mW for 2-10 FSR wavelength shifts. For the mask layout preparation, several design variants were considered with varying Bragg periods in order to compensate for fabrication variation.

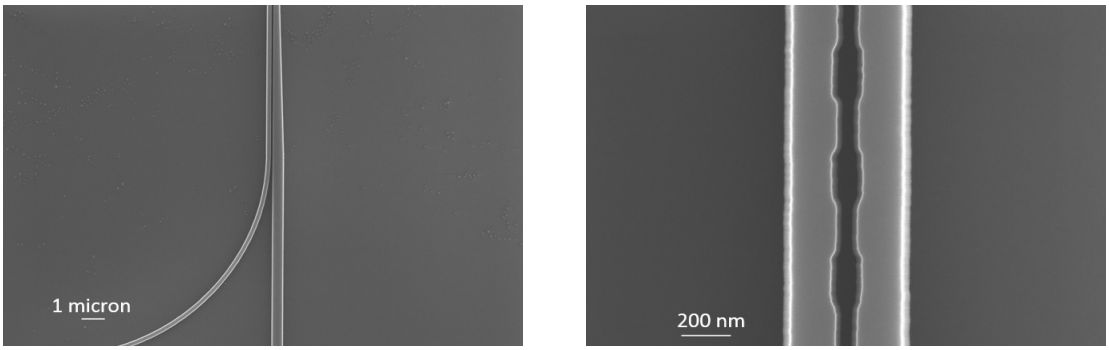


(a) (b)

Figure 4.18: (a) Top view SEM image of strip waveguide to slot waveguide mode converter. (b) Top view SEM image of slot waveguide uniform BG with internal corrugation width of $\Delta W_{in} = 20$ nm.

## 4.7 Fabrication

The devices were fabricated using 100 KeV Electron Beam Lithography [106] by Richard Bojko at the University of Washington Washington Nanofabrication Facility, part of the National Science Foundation's National Nanotechnology Infrastructure

Network (NNIN) . The fabrication used silicon-on-insulator wafer with 220 nm thick silicon on 3 $\mu$m thick silicon dioxide. The substrates were 25 mm squares diced from 150 mm wafers. After a solvent rinse and hot-plate dehydration bake, hydrogen silsesquioxane resist (HSQ, Dow-Corning XP-1541-006) was spin-coated at 4000 rpm, then hotplate baked at $80^0$ C for 4 minutes. Electron beam lithography was performed using a JEOL JBX-6300FS system operated at 100 KeV energy, 8 nA beam current, and 500 $\mu$m exposure field size. The machine grid used for shape placement was 1 nm, while the beam stepping grid, the spacing between dwell points during the shape writing, was 6 nm. An exposure dose of $2800\mu C/cm^2$ was used. The resist was developed by immersion in 25% tetramethylammonium hydroxide for 4 minutes, followed by a flowing deionized water rinse for 60 s, an isopropanol rinse for 10 s, and then blown dry with nitrogen. The silicon was removed from unexposed areas using inductively coupled plasma etching in an Oxford Plasmalab System 100, with a chlorine gas flow of 20 sccm, pressure of 12 mT, ICP power of 800 W, bias power of 40 W, and a platen temperature of $20^0$C, resulting in a bias voltage of 185 V. During etching, chips were mounted on a 100 mm silicon carrier wafer using perfluoropolyether vacuum oil. Figures 4.18(a) and 4.18(b) show top view SEM images of a fabricated strip to slot waveguide mode converter and a section of slot waveguide Bragg gratings with internal corrugation width of 20 nm described in the modeling and simulation section.

## 4.8 Experimental data results and discussion

The characterization of the devices were carried out using a custom-built automated test setup [90] with the automated control software written in Python [91]. The input source is an Agilent 86100B tunable laser and the output detectors are Agilent 81635A optical power sensors. The measured wavelength range is 1520-1580 nm in 10 pm steps and the measurement temperature is $25^0C$. A polarization maintaining fiber is used to couple TE polarized light from the input laser to the grating couplers [87]. Coupling light into and out of the chip was achieved using a polarization maintaining fiber array. The input power of the laser source is set to 1 mW or 0 dBm.

The input and output grating couplers used to couple light into the photonic circuit have a wavelength dependant transmission as shown in Fig. 4.22 with least

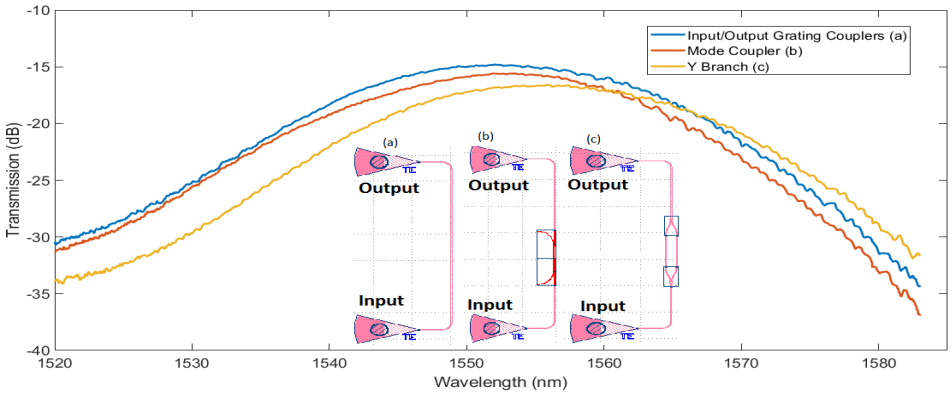


Figure 4.19: Measured transmission spectra for input output grating couplers, strip to slot waveguide mode couplers and Y branches connected back to back, which correspond to the kLayout screen capture photonic circuits shown inset as (a), (b), and (c) respectively along with labeled input and output grating couplers.

loss at 1555 nm. Also shown in Fig. 4.19 are measured transmission spectra for strip to slot waveguide mode couplers and Y branches connected back to back with zero path length difference. We can observe that for both these case, the transmission spectra follows a similar uniform profile as the input output grating couplers and we observe no fringes due to Fabry-Perot reflections as result of inserting the mode couplers and Y branches into the photonic circuit.

The transmission spectrum for the slot BG's with $\Delta W_{in} = 20$ nm show a clear stopband with an extinction ratio around 30 dB as shown in Fig. 4.20. We can observe strong fluctuations in the transmission at the stop band edge from 1520-1530 nm for the slot BG with $\Lambda = 466$ nm. This is due to group index mismatch from the slot mode to the slow light mode in the slot BG.This results in high losses as shown in the transmission response of the MZI circuit in Fig. 4.21, where small fringes of extinction ratio lower than 5 dB are obtained in the wavelength region of 1520-1530 nm. However, at the longer wavelength stopband edge, the fluctuations are minimized due to lower group index mismatch in the transition from slow light to fast light. This can be understood from the photonic band diagram of a 1D periodic structure where the first frequency photonic band corresponding to the higher wavelength stopband edge location has a lower group index dispersion compared to the second frequency photonic band where the lower wavelength stopband edge is present[107]. This causes a more efficient interference between the slow light mode and strip waveguide mode

resulting in larger fringes with extinction ratio $\sim$ 15 dB at wavelengths near 1555 nm and 1569 nm as shown in Fig. 4.21.

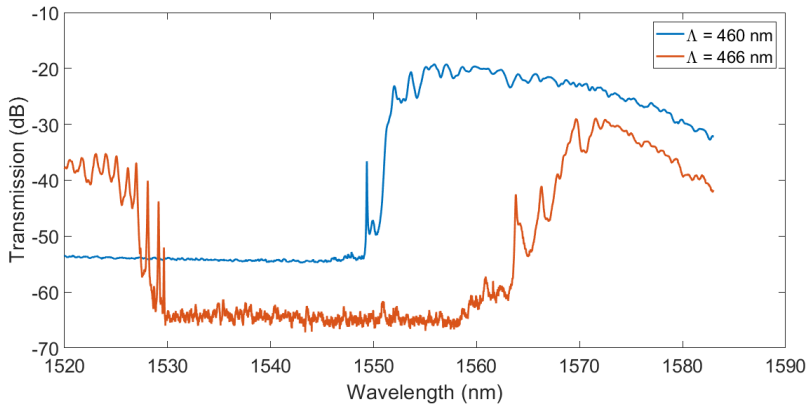


Figure 4.20: Measured transmission spectra for slot BG's with $\Delta W_{in} = 20$ nm having Bragg periods of 460 nm and 466 nm.

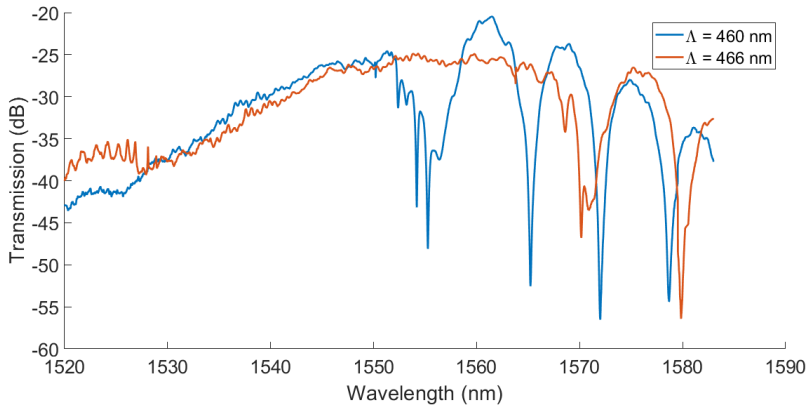


Figure 4.21: Measured transmission spectra for the MZI circuits with one arm as strip waveguide and the other arm as slot BG with $\Delta W_{in} = 20$ nm and for Bragg periods of 460 nm and 466 nm.

Using the MZI circuit shown in Fig. 4.22(b), which has one arm as a slot waveguide obtained by setting $\Delta W_{in}$ to 0 and the other arm as a strip waveguide, we observe clear MZI fringes with nearly uniform spacing indicating small variation in the group index of the slot waveguide over the entire wavelength range of 1520-1580 nm. The effect of grating coupler loss which is higher around 1520 nm and 1580 nm can be observed in the transmission spectrum shown in Fig. 4.22(a). Also shown in Fig. 4.22(a) is the calculated group index for the slot waveguide from the transmission spectrum data, which is 2.503 at a wavelength of 1553 nm.

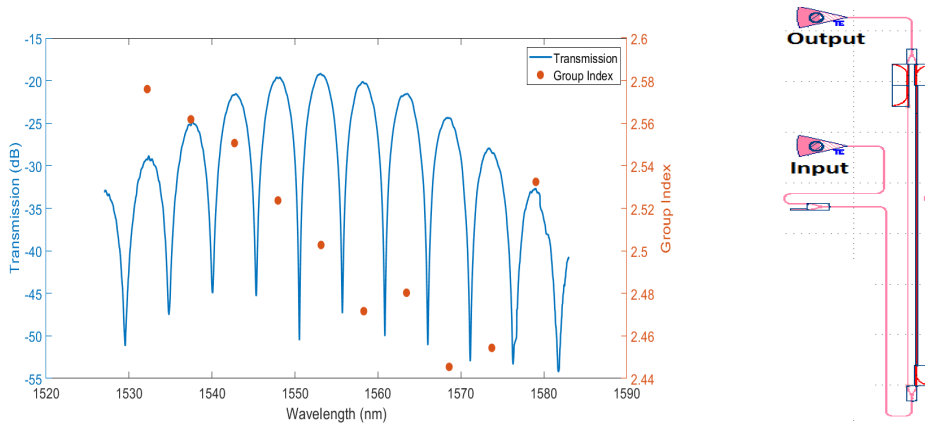


(a) (b)

Figure 4.22: (a) Measured transmission spectrum for MZI circuit with one arm as slot waveguide (i.e. with $\Delta W_{in} = 0$) and calculated group index for the slot waveguide. (b) kLayout screen capture of the MZI circuit.

The measured MZI transmission spectrum for slot BG with period of 460 nm and internal corrugation width of 20 nm shown in Fig. 4.21 is analyzed for its slow light properties around 1550 nm as shown in Fig. 4.23. We can clearly observe a fast light region with uniform fringe spacing and having a higher contrast ratio between maxima and minima, followed by a slow light region next to the photonic bandgap boundary where fringe minima are closely spaced and have lower contrast between maxima and minima. This is because of interference between higher loss slow propagating wave in the slot waveguide BG arm and light wave from the reference arm strip waveguide which has higher optical power.

The extracted group index from the measured transmission spectrum is shown in Fig. 4.23 with a peak group index $\sim 15$ at 1553 nm respectively which is comparable to the peak group index of $\sim 22$ at 1563 nm obtained in simulation. Also, we can observe in the slow light region of Fig. 4.23, a useful extinction ratio of 13.8 dB is obtained with group index of 12.94 at a wavelength of 1554 nm. This is a significant improvement is the extinction ratio in contrast to 2-5 dB obtained for externally corrugated 1D PC slot waveguide for comparable group indices [99]. This translates to lower phase shifter insertion loss as discussed in the photonic circuit simulation section.By considering the maxima and minima of electric field in the MZI transmission output, an insertion loss of 3.5 dB at 1554.7 nm wavelength where the group index is 12.38 is obtained. Alternatively, one could obtain the slow light phase shifter

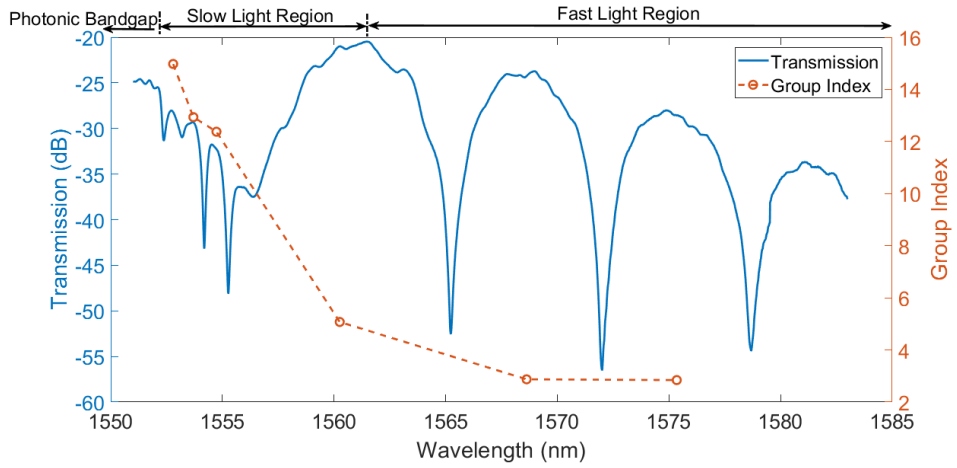


Figure 4.23: Measured raw transmission spectra for $\Delta W_{in} = 20$ nm with Bragg period of 460 nm along with calculated group index.

insertion loss from the normalized transmission spectrum of the slot BG waveguide section. Fig. 4.24(a) shows the normalized version of the measured transmission spectrum data of slot waveguide BG with $\Delta W_{in} = 20$ nm and Bragg period of 460 nm.In the normalized transmission spectrum, effect of the input output grating couplers, Y branches and strip waveguide bends were subtracted out by using the transmission spectrum from a replica photonic circuit which has a straight strip waveguide instead of the slot waveguide BG section as shown in Fig. 4.24(b). Effect of strip to slot waveguide mode couplers were subtracted out using the measurement data shown in Fig. 4.19 leaving only the transmission spectrum response of the slot waveguide Bragg section as shown in the normalized data plot in Fig. 4.24(a). Fig. 4.25 shows combined plot of the normalized spectrum in Fig. 4.24(a) and the corresponding measured MZI spectrum in Fig. 4.23. We can observe that at the wavelength corresponding to the group index of 12.38 in the slow light region, a low insertion loss of $\sim$ 2.9 dB is obtained from the normalized spectrum data.

From Fig. 4.25, we can observe that for the wavelength region 1553-1555 nm , one obtains slow light with group indices of 12-13 and a low insertion loss of 2.906 dB. Slow light coupling loss determined from 3D FDTD simulation of direct coupling between slot waveguide and the slot waveguide BG is $\sim$ 1.5 dB. This gives a slow light propagation loss of $\sim$ 5.1 dB/mm near 1555 nm wavelength. To the best of our knowledge , this is the lowest reported slow light propagation loss in 1D photonic crystal slot waveguides.

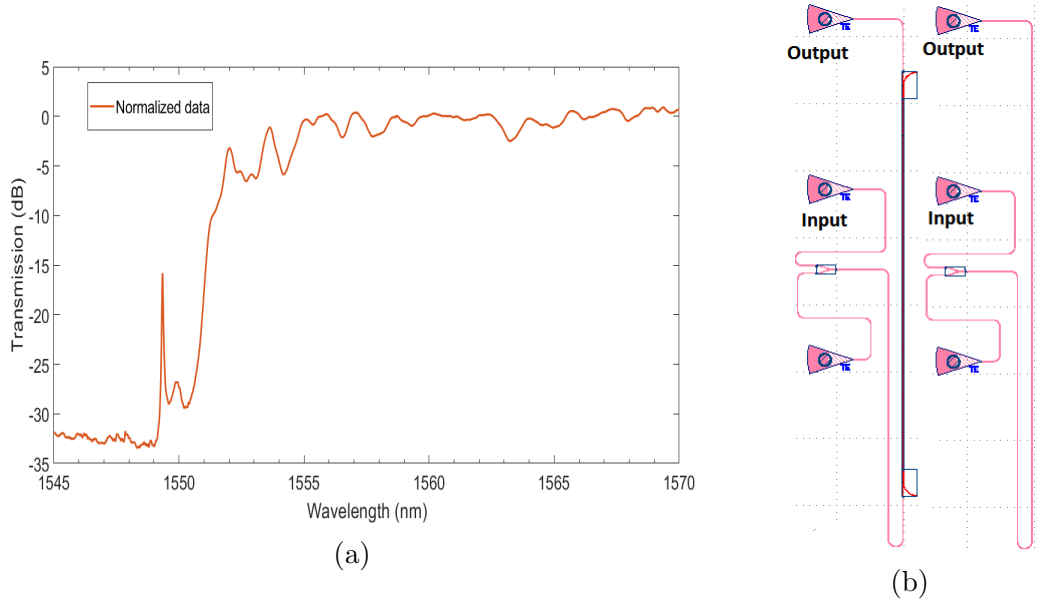


(a) (b)

Figure 4.24: (a) Measured transmission output spectrum and normalized data for slot waveguide BG with $\Delta W_{in} = 20$ nm and Bragg period of 460 nm. (b) kLayout screen capture of photonic circuits with the slot wave BG section and a reference straight strip waveguide section to obtain the normalized data plot.

The measurement derived results and simulation results confirm that slow light with low loss propagation is possible with internally corrugated slot waveguide Bragg gratings. Internal corrugated slot waveguide BG design with $\Delta W_{in} = 20$ nm have slow light group indices of 12-13 with a comparatively low phase shifter insertion loss of 3-5 dB as shown in Fig. 4.25. Both simulation and measurement data have a group index in the range ∼10-20 in the slow light region and internal corrugation provides a more efficient interaction compared to an externally corrugated 1D PC slot waveguide where a propagation loss of 15 dB/mm was obtained for a similar group index [99]. The insertion loss could be further reduced by introducing a step taper [99] in the slot BG section thereby providing better coupling from slot mode to slow light mode.

Although the current designs were fabricated using e-beam lithography which is a prototyping tool, the device dimensions considered in the design are compatible with deep ultra violet (UV) CMOS fabrication. The grating corrugations are on the sidewalls of the slot waveguide arms and therefore can be defined in single lithography step. Slot waveguide Bragg gratings with 10 nm width corrugations have been fabricated using CMOS fabrication tools [97]. The critical dimension for fabrication

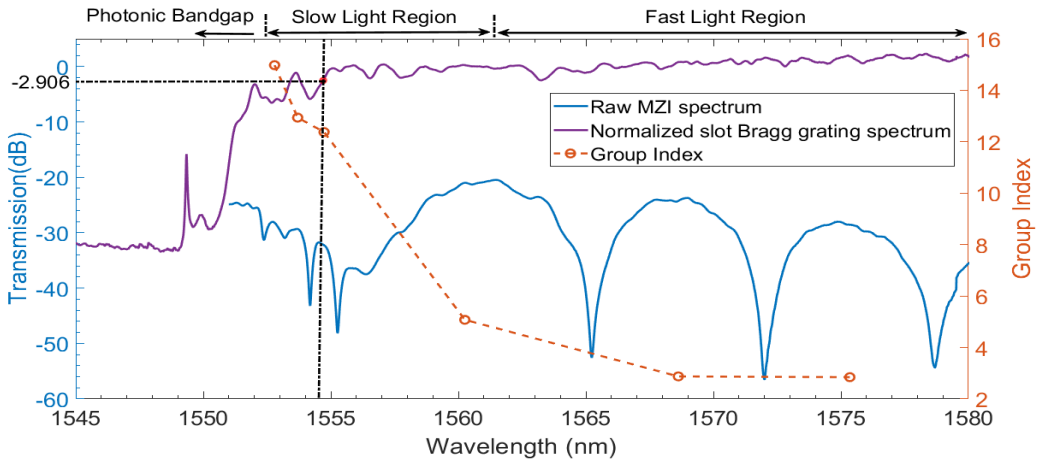


Figure 4.25: Combined plot of phase shifter insertion loss and group index along with the measured transmission spectra for slot waveguide BG with $\Delta W_{in}$ = 20 nm and Bragg period of 460 nm.

in designs considered here is the minimum separation gap between the slot waveguide arms, which is 80 nm for the slot waveguide BG with $\Delta W_{in}$ = 20 nm, as the slot gap is 100 nm. It has been shown that with advanced 193 nm deep UV immersion lithography, photonic devices with feature sizes including narrow trenches of 50 nm width can be fabricated [108]. Therefore, the considered slot waveguide BG designs are CMOS foundry compatible.

### 4.8.1 Device application potential

A key application of silicon slot waveguides is as a phase shifter for high speed, low voltage electro-optic modulator applications [69, 95, 94, 96]. The advantage of slot waveguide over conventional low loss strip waveguides for this application is that slot waveguide geometry enables a stronger electric field as the electrodes can be connected to the silicon slot waveguide arms allowing for electrode spacing in the range of $\sim$ 100 nm as compared to several micrometers which is the case for strip waveguide phase shifters. This results in at least an order of magnitude improvement in the modulator device figure of merit $V_{\pi}.L$ compared to similar modulators using strip waveguide phase shifters which generally have a $V_{\pi}.L$ over 1 V.cm [109] .

Polymer materials exhibit low loss of below 0.1 dB/cm in communication window wavelengths, possess refractive index in the range of 1.5-1.7 and a strong Pockels coefficient [110] making them an attractive material for hybrid silicon-based electro-optic

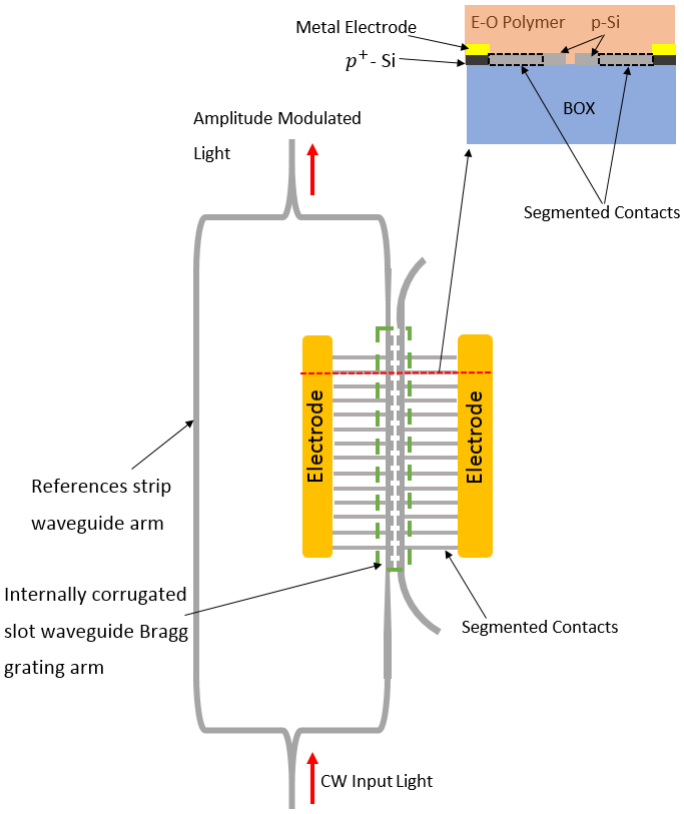


Figure 4.26: Schematic of Mach Zehnder modulator (MZM) using the internally corrugated slot waveguide Bragg gratings and cross section view in the slot waveguide BG arm.

modulator applications [111]. Modulation is achieved using the linear Pockels effect in the electro-optic polymer medium. The schematic for an electro-optic modulator using the internally corrugated slot waveguide BG in an MZM configuration is shown in Fig. 4.26. The device schematic is similar to the demonstrated MZM in [99] and MZI structure based electro-magnetic wave sensor in [24] where electro-optic polymer SEO125 from Soluxra LLC was used as the active medium. The proposed design uses the same narrow contacts with sub wavelength period as in [24] to provide electrical connection and achieve voltage drop across the slot with low optical loss. Segmented contacts with a sub wavelength period of 300 nm and segment width of 100 nm as in the demonstrated polymer clad electro-optic modulator [95] are considered in this design. Considering doping concentration of $10^{17}/cm^3$ for the silicon slot waveguide and segmented contact sections, the propagation loss of the doped segmented slot waveguide section is estimated to be 10 dB/cm [112].

Interaction factor is an important parameter for modulator applications as it quantifies the strength of interaction between light in the waveguide and the electro-optic medium. The phase shift experienced by an optical wave depends on this interaction factor and is given as [76],

$$\Delta\phi = \Gamma \Delta n k_0 L \tag{4.6}$$

Here $\Gamma$ is interaction factor of the waveguide, $\Delta n$ is the induced material refractive index change, $k_0$ is the free space wave number and $L$ is length of the phase modulator section. We can observe from Eq. (4.15) that having a phase modulator section with a higher interaction factor would make the electro-optic device more phase sensitive for the same material refractive index change and therefore more energy efficient. The interaction factor varies inversely with the group velocity [76] and is therefore directly proportional to the group index. Using this relationship, the interaction factor for slot waveguide Bragg gratings can be estimated as follows,

$$\Gamma(\lambda) = (\frac{n_g(\lambda)}{n_{g(slot)}(\lambda)}).\Gamma_{slot}(\lambda) \tag{4.7}$$

Here, $\Gamma_{slot}(\lambda)$ is the interaction factor for the nominal slot waveguide which simplifies to the confinement factor, $n_{g(slot)}(\lambda)$ and $n_g(\lambda)$ are the group indices of the slot waveguide and slot waveguide BG at the corresponding wavelength respectively. The material refractive index change due to Pockels effect is proportional to the applied electric field (E) as [76] ,

$$\Delta n = \frac{-1}{2}(n^3 r_{33} E) \ , \ E = \frac{V}{g} \tag{4.8}$$

Here, $n$ is the refractive index of the slot material which is the electro-optic polymer, $r_{33}$ is electro-optic polymer's Pockels coefficient inside the slot, V is the applied voltage and $g$ is the gap between the electrical contacts.

The electro-optic polymer SEO 125 has a bulk $r_{33}$ of $\sim$ 100 pm/V , refractive index of 1.63 at 1550 nm and a low optical loss [100]. It has been used to demonstrate a slow light enhanced effective $r_{33}$ of 490 pm/V [99] in a 150 nm wide slot, which corresponds to a material $r_{33}$ of $\sim$ 68 pm/V in the slot region taking the slow down factor (S) as 7.14 ($S = n_g/n_\phi = 20/2.8 = 7.14$). Using the same electro-optic polymer SEO125

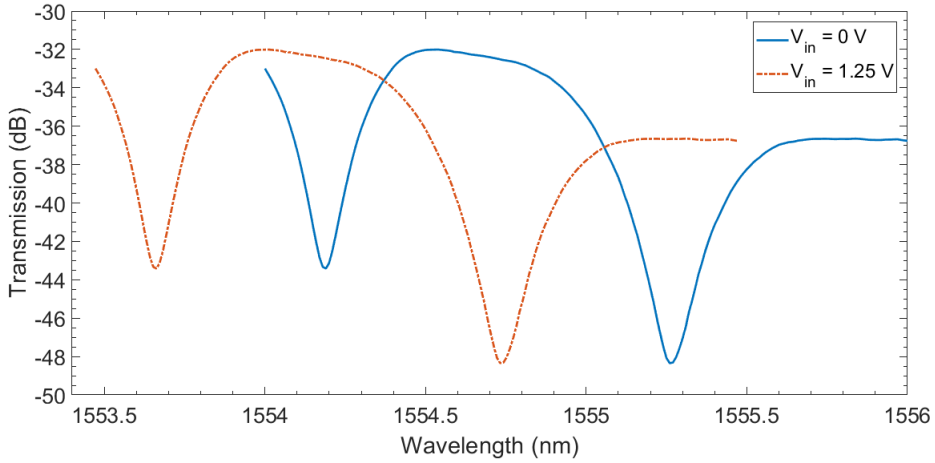


Figure 4.27: Predicted transmission spectra in the slow light region for the Mach Zehnder modulator shown in Fig. 4.26 .

as the cladding material in the design shown in Fig. 4.30 along with its material parameters and a slow light enhanced interaction factor of 1.659 for the designed slot waveguide BG, an excellent $V_\pi L$ of 0.317 V.mm is obtained. The change in cladding from silica (n=1.44) to the electro-optic polymer SEO 125 (n=1.63) is compensated by changing the Bragg period from 460 nm to 417 nm so that the phase shifter length is now $L = 600 \times 0.417 = 250.2$ $\mu$m and measured slow light region as shown in Fig. 4.28 remains around 1555 nm. The transmission spectrum including a bias of 1.25 V is shown in Fig. 4.27. In this preliminary analysis, an average value of 100 nm is used for $g$. This is because a fluctuation of 40 nm across the Bragg period of 417 nm due to internal corrugations corresponds to 0.16 % variation in $g$ over the entire phase shifter length of 250.2 microns. We can observe from Fig. 4.27 that an input voltage of 1.25 V is close to the $V_\pi$ voltage for the MZM with a useful extinction ratio of 16 dB at 1554.7 nm. Taking the worst case scenario of 120 nm as the slot gap through out the phase shifter, still gives an attractive $V_\pi L$ of 0.382 V.mm corresponding to a $V_\pi$ voltage of 1.51 V.

Using the phase shifter figure of merit ($f = \sigma.n_g.L_{3dB}$) [99] in the slow light wavelength region of 1555 nm, a value of $f = 0.37 \times 12.38 \times 0.588 \sim 2.69$ is obtained for the slot BG waveguide design with $\Delta W_{in} = 20$ nm. Here $\sigma$ is the optical mode confinement factor in the slot region that overlaps with the applied DC electric field, $n_g$ is the group index of the optical mode and $L_{3dB}$ is the phase shifter length in

mm for 3 dB propagation loss. Table 4.4 summarizes and compares different slot waveguide based phase shifters in terms of $f$ and the electro-optic modulator figure of merit $V_\pi.L$.

Table 4.4: Comparison of different slot waveguide based phase shifter structures

| **Phase Shifter Structure** | **Propagation loss (dB/mm)** | $\boldsymbol{f = \sigma n_g L_{3dB}}$ | **In-Device r33 (pm/V)** | $\boldsymbol{V_\pi.L}$**(V.cm)** | **Phase Shifter length (mm)** |
|---|---|---|---|---|---|
| Strip loaded slot waveguide [94] | 4 | 0.45 | 230 | 0.052 | 1 |
| 2D PC Slot Waveguide [100] | 20 | 1.05 | 1230 | 0.0282 | 0.3 |
| 1D PC Slot Waveguide [99] (External Corrugation) | 15 | 1.40 | 490 | 0.91 | 0.2 |
| Proposed slot BG waveguide ($\Delta W_{in}$ = 20nm) | 5.1 | 2.69 | 300 | 0.031 | 0.25 |

Although conventional slot waveguide geometries have potential for lowering propagation loss through improved fabrication processes, they are limited in terms of lowering the modulator figure of merit $V_\pi.L$ and device size as they rely on a polymer medium with a high Pockels coefficient to achieve large in-device $r_{33}$ values as in [94] where an in-device $r_{33}$ of 230 pm/V was achieved using SOH polymers. Slot waveguides embedded with photonic crystals on the other hand provide a slow light enhanced in-device $r_{33}$ in the slow light wavelength region, resulting in lower $V_\pi.L$ with compact phase shifter lengths in the range of $\sim$ 100's of $\mu$m as shown in Table 4.4. This is at the expense of a narrow operational bandwidth which is $\sim$ 2 nm for the proposed design but which can be improved using band engineering [100]. 1D PC slot waveguide have lower loss slow light compared to 2D PC slot waveguide and can still provide comparable $V_\pi.L$ to the 2D PC slot waveguide modulator. The proposed

internally corrugated slot BG waveguide has a predicted $V_{\pi}.L$ of only 0.031 V.cm considering an in slot $r_{33}$ of 68 pm/V, which has been accomplished in a 1D PC slot waveguide geometry [99]. The internally corrugated slot BG discussed here with its higher phase shifter efficiency and capability of low $V_{\pi}.L$ electro-optic modulation, makes it useful for other applications which require an efficient phase shifter section as in electromagnetic wave sensors [24] or biosensors [25, 6]. A detailed analysis for these applications is beyond the scope of this section.

## 4.9 Slow light coupling enhancement with a step taper

We experimentally report improvement in slow light coupling to internally corrugated slot Bragg grating (ICSBG) waveguide on a silicon-on-insulator platform. A short step taper is utilized to evanescently couple to the slow light mode near the stopband edge, resulting in minimization of Fabry-Perot reflections due to group index mismatch and a minimum slow light coupling enhancement of $\sim 1$ dB. This is important as it results in a lower insertion loss ICSBG waveguide, which is capable of low loss slow light propagation and therefore is an attractive option as a phase shifter structure for slow light enhanced electro-optic modulator or integrated-optic sensor applications.

### 4.9.1 Modeling and Simulation

The schematic of the transition from a strip waveguide to the ICSBG waveguide is shown in Fig. 4.28(a). It involves a strip to slot mode coupler and inclusion of an adjoining step taper at the beginning of the ICSBG section. Also indicated in Fig. 4.28(a) is the transition in group index ($n_g$) of the mode from the strip waveguide to the slot waveguide and to the slow light mode in the ICSBG section. Geometry of the ICSBG section is shown Fig. 4.28(b) where $W_{arm}$, $W_{slot}$ are the slot waveguide arm width and slot gap respectively while $\Lambda$, $\Delta W_{in}$ are the grating period and internal corrugation width respectively. In this design a grating pitch of 0.5 is used. Here the device layer is silicon with a thickness of 220 nm on a buried oxide layer and the top cladding is silicon dioxide. The fundamental slot waveguide has an arm width of 200 nm and a slot gap of 100 nm. The Bragg period for the ICSBG waveguide with $\Delta W_{in} = 20$ nm is chosen as 466 nm so that the stopband edge lies with the measurement window of 1.52-1.58 $\mu$m.

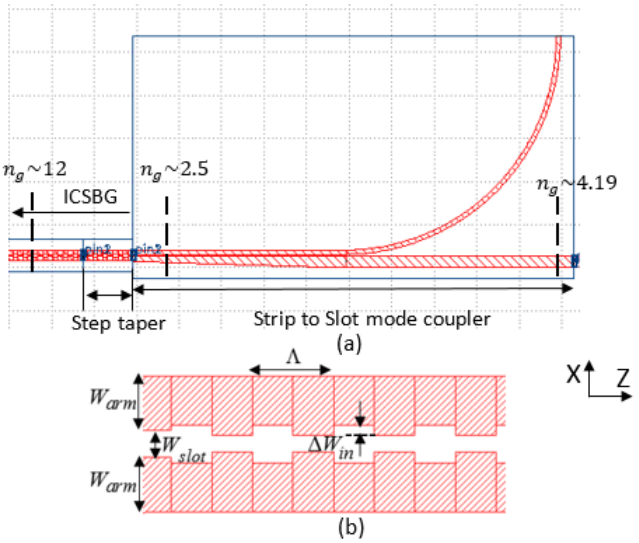


Figure 4.28: (a) kLayout schematic of the strip to slot mode coupler, step taper and the ICSBG structure. (b) Zoomed in kLayout schematic of the ICSBG structure.

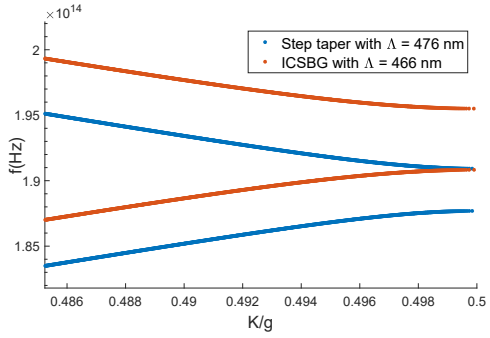


Figure 4.29: Dispersion plot of a unit cell in the ICSBG section with $\Lambda = 466$ nm, $\Delta W_{in} = 20$ nm and in the step taper section where $\Lambda = 476$ nm and $\Delta W_{in} = 14$ nm.

It has been experimentally shown that a short step taper performs better than a long adiabatic group index taper for 2D PC slot waveguide [113] because of evanescent coupling of the slow light mode and has been used to provide better coupling to slow light in a 1D PC slot waveguide with external corrugations [99, 24]. The Bragg period for the step taper section with 5 periods is chosen as 476 nm with $\Delta W_{in} = 14$ nm.The dispersion plot for a unit cell in the ICSBG waveguide with a grating period of 466 nm and step taper with $\Lambda = 476$ nm is shown in Fig. 4.29. We can observe that dispersion mode solutions for the two unit cells almost overlap around the stopband edge of 190.9 THz which corresponds to a wavelength of 1.57 $\mu$m.This allows for

evanescent coupling of the mode between the step taper and ICSBG waveguide in this slow light wavelength region.

### 4.9.2 Measurement Data and Analysis

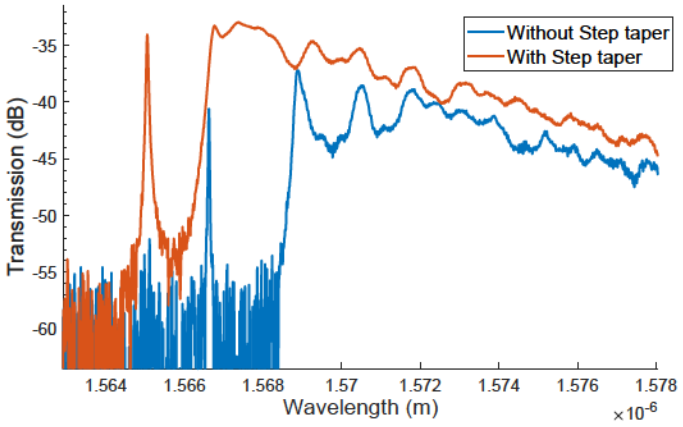


(a)

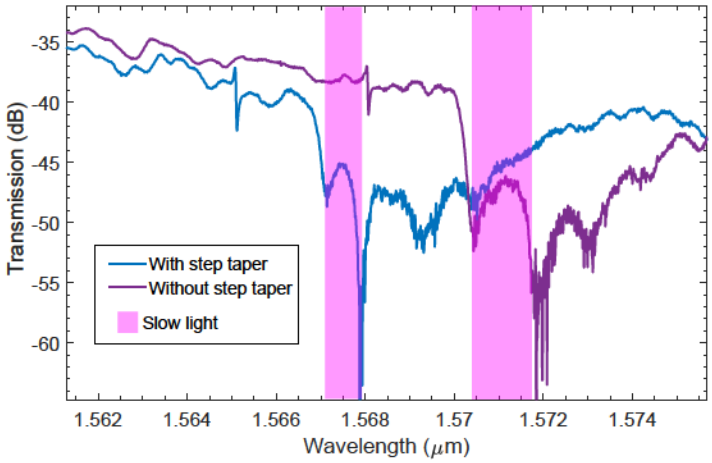


(b)

Figure 4.30: (a)Measured raw transmission spectra with and without the step taper for ICSBG waveguide with $\Lambda = 466$ nm and $\Delta W_{in} = 20$ nm. (b)Measured transmission spectra of the MZI circuit with the highlighted slow light region.

The e-beam fabrication process and the characterization setup used are as described in sections 4.7 and 4.8 in this chapter.The measured transmission spectrum for the ICSBG waveguide with and without the step taper transition to the strip to slot mode coupler is shown in Fig. 4.30(a). We can observe that the stopband edge

has shifted to a shorter wavelength for the ICSBG waveguide with step taper due to evanescent coupling and the Fabry-Perot reflections at the stopband edge have been minimized compared to the ICSBG waveguide without step taper. This indicates lower group index mismatch around the stopband edge and thus better coupling to the slow light mode.

In order to estimate the improvement in slow light coupling, the transmission spectrum of an Mach Zehnder Interferometer (MZI) circuit shown in Fig. 4.17 is analyzed, where one arm is the ICSBG section and the other arm is a strip waveguide of the same length. The MZI circuit is similar to the ones in sections 4.6.1 and 4.8, where they are described in detail.We can observe clear narrow fringes indicating slow light near the photonic bandgap edge for the MZI circuits with and without step taper in the ICSBG section.The improvement in slow light coupling loss can be estimated by analyzing the slow light fringes shown in Fig. 4.30.(b).

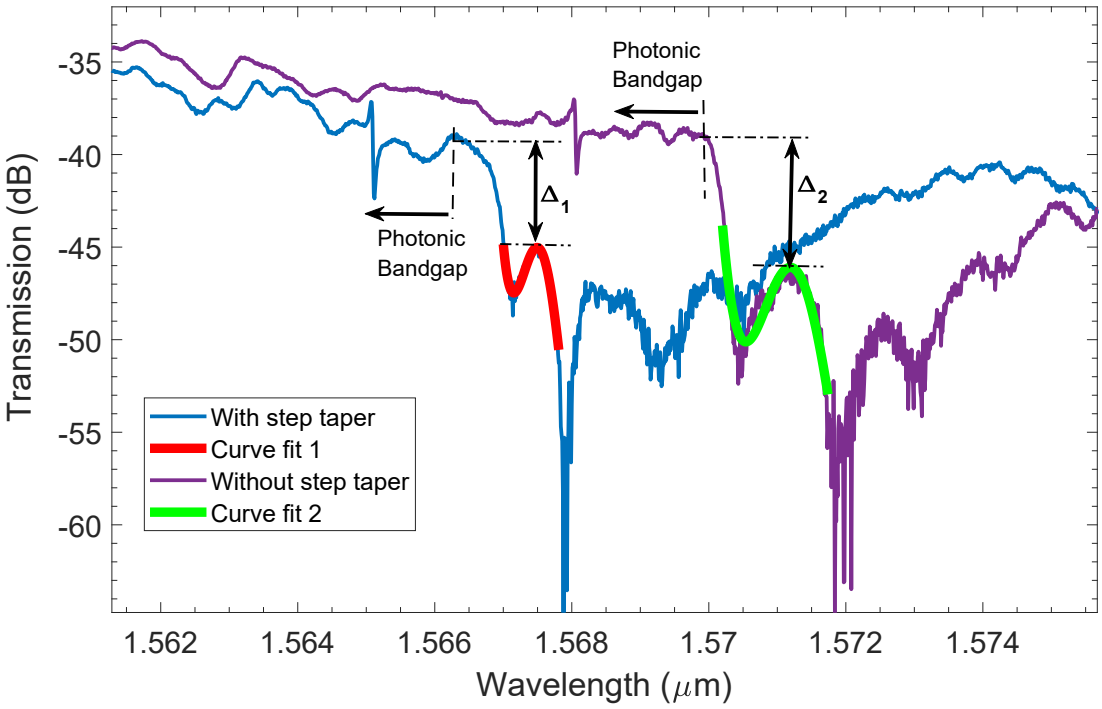


Figure 4.31: Measured raw transmission spectra for the MZI circuit.

Considering the difference in optical transmission power levels between the photonic bandgap edge and maxima of the slow light fringes, which are represented as $\Delta_1$ and $\Delta_2$ in Fig. 4.31, one can estimate the enhancement in slow light coupling for the

ICSBG section with step taper. The photonic bandgap edge is the point after which the transmission level begins to drop due to interference between slow light in the ICSBG arm and light from the strip waveguide arm of the MZI circuit. Using curve fit 1 and curve fit 2 for the measured data with and without the step taper respectively, as shown Fig. 4.31, a $\Delta_1 \simeq$6.01 dB and $\Delta_1 \simeq$7.12 dB is obtained. This gives a slow light coupling enhancement of $\sim$1.11 dB. Although there is some arbitrariness in the curve fit of measured data, the estimated minimum slow light coupling enhancement is $\sim$1 dB for this case, with potential to get a more accurate estimate considering a normalized transmission spectrum for the ICSBG waveguide.

## 4.10 Summary and conclusion

Slot waveguide BG with a internal corrugation design has been analyzed for its slow light properties in 1520-1580 nm wavelength range in simulation and in experiment. Slot BG with internal corrugations provide stronger and more efficient interaction than external corrugations. Group indices of 12-13 and insertion loss of 3-5 dB for internally corrugated slot waveguide Bragg gratings were extracted out through experimentally obtained transmission spectra.This improved interaction between the periodic corrugations and the slot mode results in a enhanced phase shifter figure of merit. A minimum slow light propagation loss of $\sim$ 5.1 dB/mm is obtained experimentally which to the best of our knowledge is the lowest reported slow light propagation loss for slot waveguides using a 1D photonic crystal structure. The application of a slot BG with $\Delta W_{in} = 20$ nm as a phase shifter in a electro-optic MZM has been analyzed with a calculated $V_{\pi}.L$ of only 0.031 V.cm. Slow light coupling to the ICSBG waveguide has been improved with the use of a short step taper. Evanescent coupling of the slow light mode from the step taper to the ICSBG section is experimentally verified with shift in the stop band edge to a shorter wavelength and reduction in the Fabry-Perot reflections due to group index mismatch. A slow light coupling enhancement of $\sim$ 1 dB has been experimentally obtained with the use of a short step taper adjoining the ICSBG section. This could be further improved with optimization of the step taper design parameters leading to lossless slow light coupling and therefore make on-chip slow light applications more efficient. In conclusion, slot BG waveguide with internal corrugations being easier to fabricate than

2D PC slot waveguides can provide slow light enhancements with low loss for practical high performance electro-optic modulator applications and potentially sensing applications.

# Chapter 5

# Conclusion

This thesis has described capabilities of silicon photonic devices in a polarization beam splitter using MMI's and MZI arms on micrometer scale device layer thickness, high speed Kerr effect modulator and slow light enhanced slot waveguide phase shifter on 220 nm scale thicknesses for silicon-based photonic integrated circuits. Although the main target areas for application of these photonic devices is in telecom or datacom optical interconnects, other potential applications are EM wave sensing [24], high speed modulators for RF photonics [26], autonomous car sensor's video data processing [28, 29], and in highly sensitive biosensors [25, 6]. The following sections summarize the micron and nano meter scale silicon photonic devices described in this thesis along with a list of future work to build on the work carried out in this thesis.

## 5.1 Summary

1. Micron scale Silicon photonics

   (a) Development of silicon photonic devices on micron scale thickness has been introduced from an Industrial perspective for telecom and datacom applications.

   (b) Design of the fundamental rib waveguide for single mode operation along with CMOS compatible fabrication process steps has been described.

   (c) A novel shallow etch PBS has been designed using a combination of 2x2 3 dB MMI splitters and MZI arms. Design of a low loss 2x2 3 dB MMI, tapers and MZI arms to achieve polarization splitting has been described. Simulation results for the nominal PBS design indicate an excess loss below 0.4 dB for both TE and TM polarizations, polarization extinction ratio greater than 15 dB and polarization dependant losses below 0.2 dB over the telecom C band wavelength range of 1530-1565 nm. In addition, the

nominal PBS design performance is robust to fabrication errors of upto +/- 10 nm in etch depth and +/- 50 nm in rib width.

2. Silicon Electro-Optic Kerr effect modulator

   (a) A literature review in the field of silicon electro-optic modulators has been provided. Limitations of the predominantly used charge carrier effect to achieve modulation in silicon has been described.

   (b) A novel silicon slot waveguide electro-optic Kerr effect modulator has been proposed. The theoretical background and CMOS compatible resonator structure implementation wherein ultrafast DC Kerr effect in silicon nanocrystals is utilized, has been described. The overall modulation bandwidth of the proposed design is 45 GHz, therefore allowing 90 Gb/s data rate transmission with a low energy/bit consumption of 25.13 fJ/bit in a compact ring resonator structure of 20 $\mu$m radius.

3. Silicon nanowire MZI circuits and low loss slow light propagation in silicon slot waveguides.

   (a) Silicon nanowire MZI circuits have been theoretically analyzed, designed, fabricated using e-beam lithography and experimentally characterized. A group index of 4.19 is experimentally obtained for the nanowire strip waveguide in the wavelength range of 1520-1580 nm and extinction ratios in excess of 30 dB are obtained experimentally for internally corrugated slot waveguide Bragg gratings.

   (b) Silicon slot waveguide Bragg gratings have been designed, fabricated and the experimental data has been analyzed for its slow light properties. Slow light with a group index of 12.38 at a wavelength near 1555 nm and having a low propagation loss of 5.1 dB/mm has been determined for internally corrugated slot waveguide Bragg gratings on a silicon-on-insulator platform. The combination of slow light and low propagation loss make the internally corrugated slot waveguide Bragg gratings especially attractive as a phase shifter section for low drive voltage, high speed and compact electro-optic modulators.

(c) Slow light coupling to the ICSBG waveguide has been improved with the use of a short step taper. Evanescent coupling of the slow light mode from the step taper to the ICSBG section is experimentally verified with shift in the stop band edge to a shorter wavelength and reduction in the Fabry-Perot reflections due to group index mismatch.An experimentally determined minimum slow light coupling enhancement of ∼1 dB is obtained.

## 5.2 Future Work

The next steps to develop on the work carried out in this thesis are listed below.

1. In micron scale silicon photonics, next steps would be to have design variants for the polarization beam splitter in order to have them in the mask layout for fabrication followed by experimental characterization of the devices. In addition to shallow etch PBS design with asymmetric MZI arms described in this thesis, symmetric MZI arms [46] needs to be explored for potential improvement in fabrication tolerance and a deep etch PBS design for shorter device lengths.

2. The advantages of micron scale silicon photonics in terms of low excess loss and low polarization dependant loss can be utilized for design of other photonic devices such as polarization rotator, and a low loss variable optical attenuator using thermo-optic effect.

3. Preparation of mask layout design variants for fabrication of the Silicon Electro-Optic Kerr effect modulator. A TCAD analysis of high frequency operation of the modulator would useful to determine potential RC parasitics that could limit the modulation bandwidth.

4. Preparation of the experimental setup to characterize the performance of the silicon Electro-Optic Kerr effect modulator.

5. Optimization of the step taper designs to enable lossless slow light coupling from slot waveguide mode to the slow light mode in the slot waveguide Bragg grating section.This would involve modeling and simulation of step taper design

variants, preparation of mask layout for fabrication followed by measurement data analysis.

6. Increase of slow light bandwidth for internally corrugated slot waveguide Bragg gratings.

## Bibliography


[1] M. Cada, "Nonlinear Kerr Materials," Nanphotonics Technology Centre (NTC), UPV, Spain, Valencia, Tech. Rep., 2008.

[2] D. T. Neilson, "Photonics for switching and routing," in *Eur. Conf. Opt. Commun.*, 2006, pp. 1–4.

[3] E. Ip, A. P. Lau, D. J. Barros, and J. M. Kahn, "Coherent detection in optical fiber systems," *Opt. Express*, vol. 16, no. 2, pp. 753–791, 2008.

[4] R. Halir, G. Roelkens, A. Ortega-Moñux, J. G. Wangüemert-Pérez, and I. Molina-Fernández, "High performance multimode interference couplers for coherent communications in silicon," in *Photonics North*. SPIE, 2011, p. 80071B.

[5] L. B. Soldano and E. C. M. Pennings, "Optical Multi-Mode Interference Devices Based on Self-Imaging : Principles and Applications," *IEEE J. Light. Technol.*, vol. 13, no. 4, p. 615, 1995.

[6] X. Wang, J. Flueckiger, S. Schmidt, S. Grist, S. T. Fard, J. Kirk, M. Doerfler, K. C. Cheung, D. M. Ratner, and L. Chrostowski, "A silicon photonic biosensor using phase-shifted Bragg gratings in slot waveguide," *J. Biophotonics*, vol. 828, no. 10, pp. 821–828, 2013.

[7] M. Asghari, "Silicon photonics: A low cost integration platform for datacom and telecom applications," in *OFC/NFOEC 2008 - 2008 Conf. Opt. Fiber Commun. Fiber Opt. Eng. Conf.*, 2008.

[8] K. Solehmainen, T. Aalto, J. Dekker, M. Kapulainen, M. Harjanne, and P. Heimala, "Development of multi-step processing in silicon-on-insulator for optical waveguide applications," *J. Opt. A Pure Appl. Opt.*, 2006.

[9] Cisco VNI, "Cisco Visual Networking Index: Forecast and Trends, 2017–2022," Cisco, Tech. Rep., 2018.

[10] T. Daniel Kilper, K. Bergman, V. W. S. Chan, I. Monga, G. Porter, and K. Rauschenbach, "Optical Networks Come of Age," *Opt. Photonics News*, pp. 51–57, 2014.

[11] M. Daikoku, I. Morita, H. Taga, H. Tanaka, T. Kawanishi, T. Sakamoto, T. Miyazaki, and T. Fujita, "100-Gb/s DQPSK transmission experiment without OTDM for 100G ethernet transport," in *OFC*, 2006, p. PDP36.

[12] A. Novack, N. C. Harris, Zhe Xuan, M. Hochberg, Ran Ding, T. Baehr-Jones, and Yi Zhang, "Silicon Photonics: The Next Fabless Semiconductor Industry," *IEEE Solid-State Circuits Mag.*, 2013.

[13] L. Conway, "Reminiscences of the VLSI revolution: How a series of failures triggered a paradigm shift in digital design," *IEEE Solid-State Circuits Mag.*, 2012.

[14] Luxtera, "Silicon Photonics Optical Transceivers." [Online]. Available: https://www.intel.com/content/www/us/en/products/network-io/high-performance-fabrics/silicon-photonics.html

[15] Mellanox Technologies, "LinkX® Silicon Photonics." [Online]. Available: http://www.mellanox.com/products/interconnect/silicon-photonics.php

[16] AMF, "Advanced Micro Foundry Services." [Online]. Available: http://www.advmf.com/services/

[17] EPIXfab, "MPW Fabrication- ePIXfab- European Silicon Photonics Alliance." [Online]. Available: http://epixfab.eu/technology-access/mpw-fabrication/

[18] WNF, "JEOL JBX-6300FS E-Beam Lithography at the Washington Nanofabrication Facility." [Online]. Available: https://ebeam.wnf.uw.edu/ebeamweb/news/projects/projects/silicon{_}photonics{_}1.html

[19] Applied Nanotools Inc., "NanoSOI Fabrication Process." [Online]. Available: https://www.appliednt.com/nanosoi/

[20] F. Boeuf, S. Crémer, N. Vulliet, T. Pinguet, A. Mekis, G. Masini, L. Verslegers, P. Sun, A. Ayazi, N.-K. Hon, S. Sahni, Y. Chi, B. Orlando, D. Ristoiu, A. Farcy, F. Leverd, L. Broussous, D. Pelissier-Tanon, C. Richard, L. Pinzelli, R. Beneyton, O. Gourhant, E. Gourvest, Y. Le-Friec, D. Monnier, P. Brun, M. Guillermet, D. Benoit, K. Haxaire, J. R. Manouvrier, S. Jan, H. Petiton, J. F. Carpentier, T. Quémerais, C. Durand, D. Gloria, M. Fourel, F. Battegay, Y. Sanchez, E. Batail, F. Baron, P. Delpech, L. Salager, P. De Dobbelaere, and B. Sautreuil, "A Multi-wavelength 3D-compatible Silicon Photonics Platform on 300mm SOI wafers for 25Gb/s Applications," in *IEEE Int. Electron Devices Meet.* IEEE, 2013.

[21] C. Doerr, L. Chen, D. Vermeulen, T. Nielsen, S. Azemati, S. Stulz, G. McBrien, X. M. Xu, B. Mikkelsen, M. Givehchi, C. Rasmussen, and S. Y. Park, "Single-chip silicon photonics 100-Gb/s coherent transceiver," in *Conf. Opt. Fiber Commun. Tech. Dig. Ser.*, 2014.

[22] S. Chandrasekhar, R. Aroca, Young-Kai Chen, Xiang Liu, L. L. Buhl, and Po Dong, "Monolithic Silicon Photonic Integrated Circuits for Compact 100+ Gb/s Coherent Optical Receivers and Transmitters," *IEEE J. Sel. Top. Quantum Electron.*, 2014.

[23] S. Wang, R. T. Chen, H. Subbaraman, Q. Zhan, J. Luo, A. K.-Y. Jen, X. Zhang, and A. Hosseini, "Integrated Photonic Electromagnetic Field Sensor Based on

Broadband Bowtie Antenna Coupled Silicon Organic Hybrid Modulator," *J. Light. Technol.*, 2014.

[24] C.-J. Chung, X. Xu, Z. Pan, F. Mokhtari-Koushyar, R. Wang, H. Yan, and R. T. Chen, "Silicon-Based Hybrid Integrated Photonic Chip for Ku band Electromagnetic Wave Sensing," *J. Light. Technol.*, 2017.

[25] Q. Liu, X. Tu, K. W. Kim, J. S. Kee, Y. Shin, K. Han, Y. J. Yoon, G. Q. Lo, and M. K. Park, "Highly sensitive Mach-Zehnder interferometer biosensor based on silicon nitride slot waveguide," *Sensors Actuators, B Chem.*, vol. 188, pp. 681–688, 2013.

[26] D. Marpaung, J. Yao, and J. Capmany, "Integrated microwave photonics," *Nat. Photonics*, 2019.

[27] D. Vermeulen, M. J. Byrd, D. B. Cole, M. R. Watts, C. V. Poulton, M. Raval, and A. Yaacobi, "Coherent solid-state LIDAR with silicon photonic optical phased arrays," *Opt. Lett.*, 2017.

[28] A. M. Spring, T. Kita, M. Sasaki, F. Qiu, M. Ozawa, S. Yokoyama, X. Cheng, O. Sugihara, H. Nawata, and T. Kashino, "Camera sensor platform for high speed video data transmission using a wideband electro-optic polymer modulator," *Opt. Express*, 2019.

[29] M. Mendez-Astudillo, M. Okamoto, Y. Ito, and T. Kita, "Compact thermo-optic MZI switch in silicon-on-insulator using direct carrier injection," *Opt. Express*, 2019.

[30] L. Chrostowski and M. Hochberg, *Silicon Photonics Design: from devices to systems*. Cambridge University Press, 2015.

[31] R. Halir, I. Molina-Fernandez, A. Ortega-Monux, J. G. Wanguemert-Perez, D.-X. Xu, P. Cheben, and S. Janz, "A Design Procedure for High-Performance, Rib-Waveguide-Based Multimode Interference Couplers in Silicon-on-Insulator," *J. Light. Technol.*, vol. 26, no. 16, pp. 2928–2936, 2008.

[32] W. Bogaerts, P. de Heyn, T. van Vaerenbergh, K. de Vos, S. Kumar Selvaraja, T. Claes, P. Dumon, P. Bienstman, D. van Thourhout, and R. Baets, "Silicon microring resonators," *Laser Photonics Rev.*, vol. 6, no. 1, pp. 47–73, jan 2012.

[33] G. Li, A. V. Krishnamoorthy, I. Shubin, J. Yao, Y. Luo, H. Thacker, X. Zheng, K. Raj, and J. E. Cunningham, "Ring resonator modulators in silicon for interchip photonic links," *IEEE J. Sel. Top. Quantum Electron.*, vol. 19, no. 6, 2013.

[34] B. Saleh and M. Teich, *Fundamentals of Photonics*. John Wiley and Sons Inc., 2007.

[35] V. R. Almeida, Q. Xu, C. A. Barrios, and M. Lipson, "Guiding and confining light in void nanostructure," *Opt. Lett.*, vol. 29, no. 11, pp. 1209–1211, 2004.

[36] Q. Xu, V. R. Almeida, R. R. Panepucci, and M. Lipson, "Experimental demonstration of guiding and confining light in nanometer-size low-refractive-index material," *Opt. Lett.*, vol. 29, no. 14, pp. 1626–1628, 2004.

[37] A. Rickman, "The commercialization of silicon photonics," *Nat. Photonics*, 2014.

[38] R. A. Soref, J. Schmidtchen, and K. Petermann, "Large Single-Mode Rib Waveguides in GeSi-Si and Si-on-SO2," *IEEE J. Quantum Electron.*, vol. 27, no. 8, 1991.

[39] A. G. Rickman and G. T. Reed, "Silicon-on-insulator optical rib waveguides : loss, mode characteristics, bends and y-junctions," *IEE Proceedings-Optoelectronics*, vol. 141, no. 6, pp. 391–393, 1994.

[40] D. W. Zheng, B. T. Smith, and M. Asghari, "Improved efficiency Si-photonic attenuator," *Opt. Express*, vol. 16, no. 21, pp. 16 754–16 765, 2008.

[41] T. Yin, R. Cohen, M. M. Morse, G. Sarid, Y. Chetrit, D. Rubin, and M. J. Paniccia, "31 GHz Ge n-i-p waveguide photodetectors on Silicon-on-Insulator substrate," *Opt. Express*, vol. 15, no. 21, p. 13965, 2007.

[42] K. Solehmainen, "Fabrication of microphotonic waveguide components on silicon," Ph.D. dissertation, Aalto University, 2007.

[43] M. Cherchi, S. Ylinen, M. Harjanne, M. Kapulainen, and T. Aalto, "Dramatic size reduction of waveguide bends on a micron-scale silicon photonic platform," *Opt. Express*, vol. 21, no. 15, p. 17814, 2013.

[44] J. Hong, H. Ryoo, B.-H. O, S. Lee, and E.-H. Lee, "Novel Design of Polarization Splitter Based on a Quasi-state Multimode Interference Couple," in *CLEO*, 2002, pp. 194–195.

[45] Jung Moo Hong, H. H. Ryu, S. R. Park, Jae Wan Jeong, S. G. Lee, Sunho Kim, B.-H. O, E.-H. Lee, S.-G. Park, D. Woo, S. R. Park, D. Woo, S. Kim, and B.-H. O, "Design and fabrication of a significantly shortened multimode interference coupler for polarization splitter application," *IEEE Photonics Technol. Lett.*, vol. 15, no. 1, pp. 72–74, 2003.

[46] D. Dai, Z. Wang, and J. E. Bowers, "Considerations for the design of asymmetrical machzehnder interferometers used as polarization beam splitters on a submicrometer silicon-on-insulator platform," *J. Light. Technol.*, vol. 29, no. 12, pp. 1808–1817, 2011.

[47] S. Lin, J. Hu, and K. B. Crozier, "Ultracompact, broadband slot waveguide polarization splitter," *Appl. Phys. Lett.*, 2011.

[48] Y. Shi, D. Dai, and S. He, "Proposal for an ultracompact polarization-beam splitter based on a photonic-crystal-aassisted multimode interference coupler," *IEEE Photonics Technol. Lett.*, vol. 19, no. 11, pp. 825–827, 2007.

[49] D. Dai, Z. Wang, J. Peters, and J. E. Bowers, "Compact polarization beam splitter using an asymmetrical Mach-Zehnder interferometer based on silicon-on-insulator waveguides," *IEEE Photonics Technol. Lett.*, 2012.

[50] T. K. Liang and H. K. Tsang, "Integrated polarization beam splitter in high index contrast silicon-on-insulator waveguides," *IEEE Photonics Technol. Lett.*, vol. 17, no. 2, pp. 393–395, 2005.

[51] R. A. Soref and B. R. Bennett, "Electrooptical effects in silicon," *IEEE J. Quantum Electron.*, vol. 23, no. 1, pp. 123–129, 1987.

[52] D. Kim, *Introductory Quantum Mechanics for Semiconductor Nanotechnology.* Wiley-VCH, 2010.

[53] Q. Xu, S. Manipatruni, B. Schmidt, J. Shakya, and M. Lipson, "12.5 Gbit/s carrier-injection-based silicon microring silicon modulators," *Opt. Express*, vol. 15, no. 2, pp. 430–436, 2007.

[54] A. Liu, R. Jones, L. Liao, D. Samara-Rubio, D. Rubin, O. Cohen, R. Nicolaescu, and M. Paniccia, "A high-speed silicon optical modulator based on a metaloxidesemiconductor capacitor," *Nature*, vol. 427, no. 6975, pp. 615–618, 2004.

[55] L. Liao, D. Samara-Rubio, M. Morse, A. Liu, D. Hodge, D. Rubin, U. D. Keil, T. Franck, A. Liu, R. Jones, L. Liao, D. Samara-Rubio, D. Rubin, O. Cohen, R. Nicolaescu, M. Paniccia, U. D. Keil, T. Franck, D. Hodge, and R. Cohen, "High speed silicon Mach-Zehnder modulator," *Opt. Express*, vol. 13, no. 8, p. 3129, 2005.

[56] L. Liao, A. Liu, D. Rubin, J. Basak, Y. Chetrit, H. Nguyen, R. Cohen, N. Izhaky, and M. Paniccia, "40 Gbit/s silicon optical modulator for high-speed applications," *Electron. Lett.*, vol. 43, no. 22, 2007.

[57] K. Bédard, A. D. Simard, B. Filion, Y. Painchaud, L. A. Rusch, and S. LaRochelle, "Dual phase-shift Bragg grating silicon photonic modulator operating up to 60 Gb/s," *Opt. Express*, 2016.

[58] R. Dubé-Demers, S. LaRochelle, and W. Shi, "Ultrafast pulse-amplitude modulation with a femtojoule silicon photonic modulator," *Optica*, vol. 3, no. 6, p. 622, jun 2016.

[59] M. Chagnon, M. Osman, M. Poulin, C. Latrasse, J.-F. Gagné, Y. Painchaud, C. Paquet, S. Lessard, and D. Plant, "Experimental study of 112 Gb/s short reach transmission employing PAM formats and SiP intensity modulator at 1.3 $\mu$m," *Opt. Express*, vol. 22, no. 17, p. 21018, 2014.

[60] T. Baba, S. Akiyama, M. Imai, N. Hirayama, H. Takahashi, Y. Noguchi, T. Horikawa, and T. Usuki, "50-Gb/s ring-resonator-based silicon modulator," *Opt. Express*, vol. 21, no. 10, p. 11869, may 2013.

[61] X. Xiao, H. Xu, X. Li, Z. Li, T. Chu, J. Yu, and Y. Yu, "60 Gbit/s silicon modulators with enhanced electro-optical efficiency," in *Opt. Fiber Commun. Conf. OFC 2013*, 2013.

[62] M. Lipson, "Compact electro-optic modulators on a silicon chip," *IEEE J. Sel. Top. Quantum Electron.*, 2006.

[63] M. Cada, "Silicon-based Kerr-effect electro-optic switch," Nanophotonics Technology Centre(NTC), UPV, Spain, Valencia, Tech. Rep., 2008.

[64] D. V. Simili and M. Cada, "Silicon Kerr Effect Electro-optic Switch," in *DCPHOTOPTICS*, 2015, pp. 74–79.

[65] R. Boyd, *Nonlinear Optics*, 3rd ed. Elsevier, 2008.

[66] A. Martínez, J. Blasco, P. Sanchis, J. V. Galán, J. García-Rupérez, E. Jordana, P. Gautier, Y. Lebour, S. Hernández, R. Guider, N. Daldosso, B. Garrido, J. M. Fedeli, L. Pavesi, and J. Martí, "Ultrafast all-optical switching in a silicon-nanocrystal-based silicon slot waveguide at telecom wavelengths," *Nano Lett.*, vol. 10, no. 4, pp. 1506–1511, 2010.

[67] J. Bickford, N. Bambha, and S. Preble, "CMOS compatible modulation of 1.5-micron light using silicon nanocrystals," in *2012 IEEE Avion. Fiber- Opt. Photonics Technol. Conf. AVFOP 2012*, vol. 3, 2012, pp. 86–87.

[68] L. Cao, A. Aboketaf, K. Narayanan, A. Elshaari, S. Kowsz, E. Freeman, S. McDermott, S. F. Preble, J. Bickford, and N. Bambha, "Direct Observation of DC Kerr Electro-Optic Modulation using Silicon Nanocrystals," in *FiO/LS Tech. Dig.*, 2013, p. FTu1A.5.

[69] M. Hochberg, T. Baehr-Jones, G. Wang, J. Huang, P. Sullivan, L. Dalton, and A. Scherer, "Towards a millivolt optical modulator with nano-slot waveguides," *Opt. Express*, vol. 15, no. 13, p. 8401, 2007.

[70] B. Qi, P. Yu, Y. Li, X. Jiang, M. Yang, and J. Yang, "Analysis of Electrooptic Modulator With 1-D Slotted Photonic Crystal Nanobeam Cavity," *IEEE Photonics Technol. Lett.*, vol. 23, no. 14, pp. 992–994, 2011.

[71] E. Jordana, J.-M. Fedeli, P. Lyan, J. Colonna, P. Gautier, N. Daldosso, L. Pavesi, Y. Lebour, P. Pellegrino, B. Garrido, J. Blasco, F. Cuesta-Soto, and P. Sanchis, "Deep-UV Lithography Fabrication of Slot Waveguides and Sandwiched Waveguides for Nonlinear Applications," in *IEEE Int. Conf. Gr. IV Photonics*. IEEE, 2007, pp. 222–224.

[72] T. Baehr-Jones, M. Hochberg, G. Wang, R. Lawson, Y. Liao, P. Sullivan, L. Dalton, A. Jen, and A. Scherer, "Optical modulation and detection in slotted Silicon waveguides." *Opt. Express*, vol. 13, no. 14, pp. 5216–26, 2005.

[73] D. Miller, "Time Dependant Perturbation Theory," in *Quantum Mech. Sci. Eng.* Cambridge University Press, 2008, ch. 7, pp. 195–205.

[74] T. Baehr-Jones, M. Hochberg, C. Walker, E. Chan, D. Koshinz, W. Krug, and A. Scherer, "Analysis of the tuning sensitivity of silicon-on-insulator optical ring resonators," *J. Light. Technol.*, vol. 23, no. 12, pp. 4215–4221, 2005.

[75] M. Cada, M. Qasymeh, and J. Pistora, "Electrically and optically controlled cross-polarized wave conversion," *Opt. Express*, vol. 16, no. 5, p. 3083, 2008.

[76] J.-M. Brosi, C. Koos, L. C. Andreani, M. Waldow, W. Freude, and J. Leuthold, "High-speed low-voltage electro-optic modulator with a polymer-infiltrated silicon photonic crystal waveguide," *Opt. Express*, vol. 16, no. 6, p. 4177, 2008.

[77] J. Matres, C. Lacava, G. C. Ballesteros, P. Minzioni, I. Cristiani, J. M. Fédéli, J. Martí, and C. J. Oton, "Low TPA and free-carrier effects in silicon nanocrystal-based horizontal slot waveguides," *Opt. Express*, vol. 20, no. 21, p. 23838, 2012.

[78] I. D. Rukhlenko, M. Premaratne, and G. P. Agrawal, "Effective mode area and its optimization in silicon-nanocrystal waveguides," *Opt. Lett.*, vol. 37, no. 12, p. 2295, 2012.

[79] G. T. Reed, G. Z. Mashanovich, F. Y. Gardes, M. Nedeljkovic, Y. Hu, D. J. Thomson, K. Li, P. R. Wilson, S. W. Chen, and S. S. Hsu, "Recent breakthroughs in carrier depletion based silicon optical modulators," *Nanophotonics*, vol. 3, no. 4-5, pp. 229–245, 2014.

[80] P. Steglich, C. Mai, C. Villringer, S. Pulwer, M. Casalboni, S. Schrader, and A. Mai, "Quadratic electro-optic effect in silicon-organic hybrid slot-waveguides," *Opt. Lett.*, vol. 43, no. 15, p. 3598, aug 2018.

[81] P. Steglich, C. Mai, A. Peczek, F. Korndorfer, C. Villringer, B. Dietzel, and A. Mai, "Quadratic electro-optical silicon-organic hybrid RF modulator in a photonic integrated circuit technology," in *Tech. Dig. - Int. Electron Devices Meet. IEDM.* Institute of Electrical and Electronics Engineers Inc., jan 2018, pp. 23.3.1–23.3.4.

[82] P. Steglich, C. Villringer, B. Dietzel, C. Mai, S. Schrader, M. Casalboni, and A. Mai, "On-Chip Dispersion Measurement of the Quadratic Electro-Optic Effect in Nonlinear Optical Polymers Using a Photonic Integrated Circuit Technology," *IEEE Photonics J.*, vol. 11, no. 3, pp. 1–10, jun 2019. [Online]. Available: https://ieeexplore.ieee.org/document/8718361/

[83] C. A. Barrios and M. Lipson, "Electrically driven silicon resonant light emitting device based on slot-waveguide," *Opt. Express*, vol. 13, no. 25, p. 10092, 2006.

[84] J. Leuthold, C. Koos, W. Freude, L. Alloatti, R. Palmer, D. Korn, J. Pfeifle, M. Lauermann, R. Dinu, S. Wehrli, M. Jazbinsek, P. Günter, M. Waldow, T. Wahlbrink, J. Bolten, H. Kurz, M. Fournier, J. M. Fedeli, H. Yu, and W. Bogaerts, "Silicon-Organic hybrid electro-optical devices," *IEEE J. Sel. Top. Quantum Electron.*, vol. 19, no. 6, 2013.

[85] J. Witzens, T. Baehr-Jones, and M. Hochberg, "Design of transmission line driven slot waveguide Mach-Zehnder interferometers and application to analog optical links," *Opt. Express*, vol. 18, no. 16, p. 16902, 2010.

[86] R. Guider, N. Daldosso, A. Pitanti, E. Jordana, J.-M. Fedeli, and L. Pavesi, "NanoSi low loss horizontal slot waveguides coupled to high Q ring resonators: Erratum," *Opt. Express*, vol. 17, no. 26, p. 23556, 2009.

[87] Y. Wang, X. Wang, J. Flueckiger, H. Yun, W. Shi, R. Bojko, N. A. F. Jaeger, and L. Chrostowski, "Focusing sub-wavelength grating couplers with low back reflections for rapid prototyping of silicon photonic circuits," *Opt. Express*, vol. 22, no. 17, pp. 20 652–, 2014.

[88] ThorLabs, "THORLABS FGA015 Ge Photodiode Spec Scheet." [Online]. Available: https://www.thorlabs.com/drawings/bcb9d9af3226c6e2-71D35875-FFE9-E762-7667F1A322808D8B/FGA015-SpecSheet.pdf

[89] L. Chrostowski, Z. Lu, J. Flueckiger, X. Wang, J. Klein, A. Liu, J. Jhoja, and J. Pond, "Design and simulation of silicon photonic schematics and layouts," in *Silicon Photonics Photonic Integr. Circuits V*. International Society for Optics and Photonics, 2016, p. 989114.

[90] L. Chrostowski and M. Hochberg, "Testing and Packaging," in *Silicon Photonics Des.* Cambridge University Press, 2015, pp. 381–405.

[91] "Automated Probe Station-siepic.ubc.ca." [Online]. Available: http://siepic.ubc.ca/probestation

[92] PLC, "PLC Connections." [Online]. Available: http://www.plcconnections.com/

[93] D. Dai, J. Bauters, and J. E. Bowers, "Passive technologies for future large-scale photonic integrated circuits on silicon: Polarization handling, light non-reciprocity and loss reduction," *Light Sci. Appl.*, vol. 1, no. MARCH, pp. 1–12, 2012.

[94] R. Palmer, S. Koeber, D. L. Elder, M. Woessner, W. Heni, D. Korn, M. Lauermann, W. Bogaerts, L. Dalton, W. Freude, J. Leuthold, and C. Koos, "High-speed, low drive-voltage silicon-organic hybrid modulator based on a binary-chromophore electro-optic material," *J. Light. Technol.*, vol. 32, no. 16, pp. 2726–2734, 2014.

[95] T. Baehr-Jones, B. Penkov, J. Huang, P. Sullivan, J. Davies, J. Takayesu, J. Luo, T. D. Kim, L. Dalton, A. Jen, M. Hochberg, and A. Scherer, "Nonlinear polymer-clad silicon slot waveguide modulator with a half wave voltage of 0.25 V," *Appl. Phys. Lett.*, vol. 92, no. 16, pp. 23–25, 2008.

[96] L. Alloatti, R. Palmer, S. Diebold, K. P. Pahl, B. Chen, R. Dinu, M. Fournier, J. M. Fedeli, T. Zwick, W. Freude, C. Koos, and J. Leuthold, "100 GHz silicon-organic hybrid modulator," *Light Sci. Appl.*, vol. 3, no. March, pp. 5–8, 2014.

[97] X. Wang, N. A. F. Jaeger, J. Flueckiger, S. Grist, and L. Chrostowski, "Silicon photonic slot waveguide Bragg gratings and resonators," *Opt. Express*, vol. 21, no. 16, p. 19029, 2013.

[98] F. Riboli, P. Bettotti, and L. Pavesi, "Band gap characterization and slow light effects in one dimensional photonic crystals based on silicon slot-waveguides," *Opt. Express*, vol. 15, no. 19, p. 11769, 2007.

[99] H. Yan, C.-J. Chung, H. Subbaraman, S. Chakravarty, H. Subbaraman, Z. Pan, S. Chakravarty, and R. T. Chen, "One-dimensional photonic crystal slot waveguide for silicon-organic hybrid electro-optic modulators," *Opt. Lett.*, vol. 41, no. 23, p. 5466, 2016.

[100] X. Zhang, C.-J. Chung, A. Hosseini, H. Subbaraman, J. Luo, A. K.-Y. Jen, R. L. Nelson, C. Y.-C. Lee, and R. T. Chen, "High Performance Optical Modulator Based on Electro-Optic Polymer Filled Silicon Slot Photonic Crystal Waveguide," *J. Light. Technol.*, vol. 34, no. 12, pp. 2941–2951, 2015.

[101] X. Wang, C.-Y. Lin, S. Chakravarty, J. Luo, A. K.-Y. Jen, and R. T. Chen, "Effective in-device r_33 of 735 pm/V on electro-optic polymer infiltrated silicon photonic crystal slot waveguides," *Opt. Lett.*, vol. 36, no. 6, p. 882, mar 2011.

[102] A. Di Falco, M. Massari, M. G. Scullion, S. A. Schulz, F. Romanato, and T. F. Krauss, "Propagation losses of slotted photonic crystal waveguides," *IEEE Photonics J.*, vol. 4, no. 5, pp. 1536–1541, 2012.

[103] W. Bogaerts, M. Fiers, and P. Dumon, "Design Challenges in Silicon Photonics," *IEEE J. Sel. Top. Quantum Electron.*, vol. 20, no. 4, 2014.

[104] A. Brimont, A. M. Gutierrez, M. Aamer, D. J. Thomson, F. Y. Gardes, J. Fedeli, G. T. Reed, J. Marti, and P. Sanchis, "Slow-Light-Enhanced Silicon Optical Modulators Under Low-Drive-Voltage Operation," *IEEE Photonics J.*, vol. 4, no. 5, pp. 1306–1315, 2012.

[105] Q. Fang, J. F. Song, T.-Y. Liow, H. Cai, T.-Y. Liow, G. Q. Lo, and D.-L. Kwong, "Ultralow Power Silicon Photonics Thermo-Optic Switch With Suspended Phase Arms," *IEEE Photonics Technol. Lett.*, vol. 23, pp. 525–527, 2011.

[106] R. J. Bojko, T. Baehr-Jones, Y. Aida, L. He, M. Hochberg, and J. Li, "Electron beam lithography writing strategies for low loss, high confinement silicon optical waveguides," *J. Vac. Sci. Technol. B, Nanotechnol. Microelectron. Mater. Process. Meas. Phenom.*, vol. 29, p. 063F09, 2011.

[107] M. Saleh, B.E.A , Teich, "One-Dimensional Photonic Crystals," in *Fundam. Photonics*. Singapore: John Wiley and Sons Inc., 2007, ch. Photonic C, pp. 265–279.

[108] S. K. Selvaraja, G. Winroth, S. Locorotondo, G. Murdoch, A. Milenin, C. Delvaux, P. Ong, S. Pathak, W. Xie, G. Sterckx, G. Lepage, D. Van Thourhout, W. Bogaerts, J. Van Campenhout, and P. Absil, "193Nm Immersion Lithography for High-Performance Silicon Photonic Circuits," in *SPIE 9052, Opt. Microlithogr. XXVII*, vol. 9052, 2014, p. 90520F.

[109] H. Tazawa, Y.-h. Kuo, I. Dunayevskiy, J. Luo, A. K. Jen, H. R. Fetterman, W. H. Steier, and L. Fellow, "Ring Resonator-Based Electrooptic Polymer Traveling-Wave Modulator," *IEEE J. Light. Technol.*, vol. 24, no. 9, pp. 3514–3519, 2006.

[110] B. Hong Ma, A. K-Y Jen, and L. R. Dalton, "Polymer-Based Optical Waveguides: Materials, Processing, and Devices," *Adv. Mater.*, vol. 14, no. 19, pp. 1339–1365, 2002.

[111] X. Zhang, A. Hosseini, X. Lin, H. Subbaraman, and R. T. Chen, "Polymer-based hybrid-integrated photonic devices for silicon on-chip modulation and board-level optical interconnects," *IEEE J. Sel. Top. Quantum Electron.*, vol. 19, no. 6, 2013.

[112] G. Wang, T. Baehr-Jones, M. Hochberg, and A. Scherer, "Design and fabrication of segmented, slotted waveguides for electro-optic modulation," *Appl. Phys. Lett.*, vol. 91, no. 14, pp. 2005–2008, 2007.

[113] A. Hosseini, X. Xu, D. N. Kwong, H. Subbaraman, W. Jiang, and R. T. Chen, "On the role of evanescent modes and group index tapering in slow light photonic crystal waveguide coupling efficiency," *Appl. Phys. Lett.*, vol. 98, no. 3, 2011.

## Appendix A: Publications and Technical Reports

The following are list of manuscripts published or submitted for publication during my PhD studies.

1. D.V. Simili, M. Cada, "Nanophotonic Silicon Electro-Optic Switch", in Proceedings of SPIE Vol. 8915, 89151S1, Photonics North, Ottawa, ON,2013.

2. D.V. Simili, M. Cada, "Silicon Kerr Electro-Optic Switch" in Proceedings of DCPHOTOPTICS, Scitepress pp. 74-79, Berlin, Germany, 2015.

3. D.V. Simili, M. Cada, "Resonator Structure Comparison for the Silicon Kerr Electro-Optic Switch", in Proceedings of Photonics North, Quebec City,QC,2016.

4. D.V. Simili, M. Cada, and J. Pistora, "Silicon Slot Waveguide Electro-Optic Kerr Effect Modulator", IEEE Photonics Technology Letters, 30,873-876 (2018).

5. D.V. Simili, M. Cada, "Low loss slow light propagation in silicon slot waveguide", Optics Express, (to be published, manuscript accepted on $1^{st}$ July 2019).

6. D.V. Simili, M. Cada,"Improved Coupling to Slow Light in Internally Corrugated Silicon Slot Waveguide Bragg Gratings" submitted to IEEE Photonics Technology Letters on $9^{th}$ August 2019.

In addition, this thesis contains an Industrial internship report and a course (eDX Phot1x: Silicon Photonics Design, Fabrication and Data Analysis) project report mentioned below.

1. D.V Simili, 'Micron Scale Silicon Photonics for Optical Communication', Industrial internship report, Lumentum LLC, Ottawa,ON, December 2016.

2. D.V Simili, "Design, Fabrication and Experimental Data Analysis of Silicon Nanowire Mach Zehnder Interferometer Circuits and Slot Waveguide Bragg Grating Structures", UBC edX Phot1x course report, December 2017.

# Appendix B: Copyright Permission Letters

Copyright Clearance Center RightsLink®

Home | Create Account | Help

IEEE Requesting permission to reuse content from an IEEE publication

**Title:** Silicon Slot Waveguide Electro-Optic Kerr Effect Modulator
**Author:** Deepak V. Simili
**Publication:** IEEE Photonics Technology Letters
**Publisher:** IEEE
**Date:** 1 May1, 2018
Copyright © 2018, IEEE

LOGIN
If you're a copyright.com user, you can login to RightsLink using your copyright.com credentials.
Already a RightsLink user or want to learn more?

**Thesis / Dissertation Reuse**

**The IEEE does not require individuals working on a thesis to obtain a formal reuse license, however, you may print out this statement to be used as a permission grant:**

*Requirements to be followed when using any portion (e.g., figure, graph, table, or textual material) of an IEEE copyrighted paper in a thesis:*

1) In the case of textual material (e.g., using short quotes or referring to the work within these papers) users must give full credit to the original source (author, paper, publication) followed by the IEEE copyright line © 2011 IEEE.
2) In the case of illustrations or tabular material, we require that the copyright line © [Year of original publication] IEEE appear prominently with each reprinted figure and/or table.
3) If a substantial portion of the original paper is to be used, and if you are not the senior author, also obtain the senior author's approval.

*Requirements to be followed when using an entire IEEE copyrighted paper in a thesis:*

1) The following IEEE copyright/ credit notice should be placed prominently in the references: © [year of original publication] IEEE. Reprinted, with permission, from [author names, paper title, IEEE publication title, and month/year of publication]
2) Only the accepted version of an IEEE copyrighted paper can be used when posting the paper or your thesis on-line.
3) In placing the thesis on the author's university website, please display the following message in a prominent place on the website: In reference to IEEE copyrighted material which is used with permission in this thesis, the IEEE does not endorse any of [university/educational entity's name goes here]'s products or services. Internal or personal use of this material is permitted. If interested in reprinting/republishing IEEE copyrighted material for advertising or promotional purposes or for creating new collective works for resale or redistribution, please go to http://www.ieee.org/publications_standards/publications/rights/rights_link.html to learn how to obtain a License from RightsLink.

If applicable, University Microfilms and/or ProQuest Library, or the Archives of Canada may supply single copies of the dissertation.

BACK | CLOSE WINDOW

Copyright © 2019 Copyright Clearance Center, Inc. All Rights Reserved. Privacy statement. Terms and Conditions.
Comments? We would like to hear from you. E-mail us at customercare@copyright.com

OSA
The Optical Society

# Copyright Transfer and Open Access Publishing Agreement

**THIS WORK IS BEING SUBMITTED FOR PUBLICATION TO:**

☐ Journal of the Optical Society of America A ☐ Applied Optics ☐ Biomedical Optics Express
☐ Journal of the Optical Society of America B ☐ Optics Letters ☐ Optical Materials Express
☐ Journal of Optical Communications and Networking ☐ Optics & Photonics News
☐ Advances in Optics and Photonics ☑ Optics Express ☐ Optica
☐ Other _____ (name of publication)

**AUTHOR(S):**
DEEPAK V. SIMILI, MICHAEL CADA

**TITLE OF ARTICLE, PAPER, OR MANUSCRIPT ("WORK"):**
LOW LOSS SLOW LIGHT PROPAGATION IN SILICON SLOT WAVE GUIDE

**SUBMITTING AUTHOR'S NAME AND ADDRESS:**
DEEPAK V. SIMILI
DEPARTMENT OF ELECTRICAL AND COMPUTER ENGINEERING, DALHOUSIE UNIVERSITY, HALIFAX, NS B3H 4R2, CANADA.

**COPYRIGHT TRANSFER.**
Effective upon date of acceptance of this Work for publication in the above-named Publication, and in exchange for OSA reviewing, editing, and publishing the Work on an exclusive basis and for other good and valuable consideration, the receipt and sufficiency of which are hereby acknowledged, the Author(s) hereby transfer to The Optical Society (OSA) full ownership throughout the world of all rights, titles, and interests in and to the above-titled Work, including the title and abstract of the Work and all dataset(s), media objects (video files, image files, sound files, and their constituent computer code), and other enhancements accompanying the Work. OSA shall have the right to register copyright to the Work and the accompanying abstract in its name as claimant, whether separately or as part of the journal issue or other medium in which the Work is included.

The Author(s) also hereby agree that OSA may use his/her name, photo, biographical information and likeness in connection with promoting or advertising the Work and any adaptation thereof, in the journal issue or other medium in which the Work is included, and the Author(s) release OSA from any claim based on right of publicity or privacy

OSA shall make the final, published version of the article freely available on the OSA Publishing platform without charge to the user or his/her institution. Users are allowed to read, download, copy, distribute, print, search, or link to the full text of the article, or use them for any other lawful purpose, without asking prior permission from the publisher or the Author(s). This is in accordance with the BOAI definition of open access.

**AUTHOR(S) RIGHTS.**
(a) Use in Classroom or Internal Training. The Author(s) are expressly permitted to reuse any portion of the Final Publisher Version of Record of the Work in connection with the Author(s)' teaching, training, or work responsibilities. Examples of permitted uses are lecture materials, e-reserves, conference presentations, or in-house training courses.

(b) Personal Servers. Author(s) shall have the right to post the Author Accepted version or Final Publisher Version of Record on their personal non-commercial website or the servers of their institutions or employers. Any such posting made after publication of the Work shall include a link to the online abstract in the Journal and the copyright notice below.

(c) Third-Party Servers. The Author(s) are permitted to post and update the Author Accepted version or Final Publisher Version of Record on e-print servers, e.g. arXiv. Any such posting made after publication of the Work shall include a link to the online abstract in the Journal and the copyright notice below.

(d) Other Proprietary Rights. Author(s) retain all proprietary rights other than copyright, such as patent rights.

OSA
The Optical Society

(e) Government Funding Agencies. Author(s) whose work was performed under a grant from a government funding agency are permitted to fulfill author deposit mandates from that funding agency.

(f) Work-for-hire. If the Work has been prepared by an employee within the scope of his or her employment or as a work made for hire, Author(s) retain the right to distribute copies of the Work for the employer's internal use.

**COPYRIGHT NOTICE.**
The Author(s) agree that all copies of the Work made under any of the above rights shall prominently include the following copyright notice: "*© XXXX [year] Optical Society of America.* Users may use, reuse, and build upon the article, or use the article for text or data mining, so long as such uses are for non-commercial purposes and appropriate attribution is maintained. All other rights are reserved."

**AUTHOR(S)' WARRANTIES.**
The Author(s) warrant to the best of the Author(s') knowledge, belief, and expertise that:

(1) Author(s) are the sole Author(s) and sole holder(s) of all rights in the Work;

(2) Author(s) have not previously assigned, pledged, or otherwise encumbered the Work;

(3) the Work is original to the Author(s);

(4) the Work has not been previously submitted for publication (unless the prior submission has been rejected unconditionally). Furthermore, the Work has not been published elsewhere, accepted for publication elsewhere, and is not pending acceptance or being considered for publication elsewhere;

(5) the Work does not violate or infringe on any copyright or other personal or property rights of any third parties,

(6) the Work contains nothing libelous or contrary to law;

(7) any scientific knowledge contained in the Work is true and accurate;

(8) Author(s) have obtained written consent as required for the use of any third-party copyrighted or unpublished material contained in the Work and will deliver such consent to OSA; and

(9) the signing Author(s) have the full power to enter into this Agreement and to make the grants contained herein.